Computational Optimization of Organic Optoelectronic Systems

Zur Erlangung des akademischen Grades eines
DOKTORS DER NATURWISSENSCHAFTEN (Dr. rer. nat.)

von der KIT-Fakultät für Physik des
Karlsruher Instituts für Technologie (KIT)
genehmigte

DISSERTATION

von

M.Sc. Ali Deniz Özdemir

Tag der mündlichen Prüfung:	21.06.2024
Erster Gutachter:	Prof. Dr. Wolfgang Wenzel
Zweiter Gutachter:	Prof. Dr. Marcus Elstner

Erklärung:

Ich versichere wahrheitsgemäß, die Arbeit selbstständig verfasst, alle benutzten Hilfsmittel vollständig und genau angegeben und alles kenntlich gemacht zu haben, was aus Arbeiten anderer unverändert oder mit Abänderungen entnommen wurde sowie die aktuelle Satzung des KIT zur Sicherung guter wissenschaftlicher Praxis in der Fassung vom beachtet zu haben.

. . . . . .

Karlsruhe, 13.05.2024, Ali Deniz Özdemir

Acknowledgements

I want to express my sincere gratitude to everyone who accompanied, encouraged, and supported me throughout my doctoral studies:

First and foremost, I am deeply thankful to Prof. Dr. Wolfgang Wenzel for providing me with the opportunity to conduct this doctoral research under his guidance. He not only allowed me the freedom to experiment but was consistently available whenever I needed help or advice. His creative ideas were invaluable in advancing my work.

I extend a sincere thank you to Prof. Dr. Marcus Elstner for our numerous enlightening and productive discussions on the electronic properties of organic molecules. Collaborating with him has significantly broadened my scientific perspective.

I am especially grateful to my colleague Dr. Jörg Schaarschmidt for his extensive expertise in cluster computing, which played a crucial role in the successful completion of this project. Without Jörg's efforts in maintaining the operational integrity of the research cluster, this work would not have been possible.

I would also like to extend my gratitude to Dr. Franz Symalla for providing incredibly useful advice on kinetic Monte Carlo and charge transport simulations. Thank you for your support and insights throughout this journey.

Moreover, I want to show my appreciation to the entire Wenzel research group for the supportive and enriching environment throughout this journey.

Finally, I want to convey my heartfelt thanks to Anna, whose unwavering patience and care supported me through the most challenging times. Thank you!

Abstract

Organic semiconductors are a versatile group of materials with potential to augment inorganic semiconductors, especially in applications such as OLEDs. When formed into amorphous films, organic semiconductors offer mechanical flexibility, enabling the creation of novel form factors for optoelectronic devices. Despite facing challenges such as low luminance efficiency and limited operational lifespans at higher voltages, there is strong optimism about their potential for improvement, driven by the diverse range of chemical compositions within this material class.

Discovering and synthesizing materials with specific desired properties solely through experimental experience and trial-and-error approaches can be a daunting task. To complement and enhance this approach, it is essential to integrate computational models into the discovery process. These computational tools become increasingly important in material science, particularly in OLED engineering. Through the combination of experimental insights and theoretical simulations, researchers can streamline the design of materials with desired properties in a more efficient and effective manner.

Computational tools of this nature must span extensive time and length scales, necessitating the integration of diverse methods ranging from quantum chemistry to mesoscopic transport models. These methods can be embedded within scale-bridging computational workflows that enable property prediction. In this work, I integrated existing methods into multiscale workflows to conduct computational investigations into charge carrier mobility, luminance efficiency during device operation, and accelerated long-term lifetime studies using the kinetic Monte Carlo method.

One of the developed workflows aims to investigate how molecular geometry and electronic structure of the employed molecules are influenced by structural dynamics. This analysis expands an existing mobility simulation workflow by integrating molecular dynamics as an additional dimension.

In addition to this study where molecular properties are translated into transport properties of amorphous structures, comprehensive device simulations have been performed to assess the impact of device architectures on luminance efficiency. The goal is to systematically identify performance bottlenecks and establish design rules for devices that can mitigate severe roll-off processes. As a final step, a computational degradation model was developed capable of simulating molecular degradation and luminance loss across a wide range of devices under various operating conditions.

Zusammenfassung

Organische Halbleiter sind eine vielseitige Gruppe von Materialien mit dem Potenzial, anorganische Halbleiter zu ergänzen, insbesondere in Anwendungen wie OLEDs. Wenn sie zu amorphen Filmen geformt werden, bieten organische Halbleiter mechanische Flexibilität, was die Schaffung neuartiger Formfaktoren für optoelektronische Geräte ermöglicht. Trotz Herausforderungen wie geringer Effizienz und begrenzter Betriebsdauer bei höheren Spannungen herrscht eine starke Zuversicht hinsichtlich ihres Verbesserungspotenzials, angetrieben durch die Vielfältigkeit von chemischen Zusammensetzungen innerhalb dieser Materialklasse. Die Entdeckung und Synthese von Materialien mit spezifisch gewünschten Eigenschaften allein durch experimentelle Erfahrung und Trial-and-Error-Ansatz, kann eine anspruchsvolle Aufgabe sein. Um diesen Ansatz zu ergänzen und zu verbessern, ist es unerlässlich, theoretische Modelle in den Entdeckungsprozess zu integrieren. Diese Simulations-Werkzeuge spielen eine zunehmend wichtige Rolle in der Materialwissenschaft, insbesondere in der Entwicklung von OLEDs. Durch die Kombination experimenteller Erkenntnisse und theoretischer Simulationen können Forscher die Entwicklung von Materialien mit gewünschten Eigenschaften effizienter und effektiver vorantreiben. Simulatons-Tools dieser Art müssen umfangreiche Zeit- und Längenskalen abdecken und erfordern die Integration verschiedener Methoden von der Quantenchemie bis zu mesoskopischen Transportmodellen. Diese Methoden können in Multiskalen Simulationen eingebettet werden, die die Vorhersage von Eigenschaften ermöglichen. In dieser Arbeit habe ich bestehende Methoden in Multiskalen-Simulationen integriert, um computergestützte Untersuchungen zur Ladungsträgermobilität, zur Leuchtdichte-Effizienz während des OLED-Betriebs und zur Untersuchung von -Lebensdauer unter Verwendung der kinetischen Monte-Carlo-Methode durchzuführen. Einer der entwickelten Arbeitsabläufe zielt darauf ab, zu untersuchen, wie Geometrie und elektronische Eigenschaften der verwendeten Moleküle durch strukturelle Dynamik beeinflusst werden. Diese Analyse erweitert einen vorhandenen Mobilitätssimulations-Workflow durch Integration molekularer Dynamik als zusätzliche Dimension. Zusätzlich zu dieser Studie, in der molekulare Eigenschaften in Transporteigenschaften amorphen Strukturen übersetzt werden, wurden umfassende Gerätesimulationen durchgeführt, um den Einfluss von Gerätearchitekturen auf die Leuchtdichte-Effizienz zu bewerten. Das Ziel ist es, Leistungsengpässe systematisch zu identifizieren und Designregeln für Geräte festzulegen, die effizienz mindernde Prozesse reduzieren können. Als abschließender Schritt wurde ein Degradationsmodell implementiert, das in der Lage ist, molekulare Degradation und Verlust der Helligkeit von diversen OLED-Architekturen, unter verschiedenen Betriebsbedingungen zu simulieren.

List of publications

- **Ali Deniz Özdemir**, Pramit Barua, Felix Pyatkov, Frank Hennrich, Yuan Checn, Wolfgang Wenzel, Ralph Krupke, Artem Fediai. Contact spacing controls the on-current for all-carbon field effect transistors. Commun. Phys. 4, 246 (2021). https://doi.org/10.1038/s42005-021-00747-5
- **Ali Deniz Özdemir**, Simon Kaiser, Tobias Neumann, Franz Symalla, Wolfgang Wenzel. Systematic kMC Study of Doped Hole Injection Layers in Organic Electronics. Front. Chem. 9:809415 (2022). doi: 10.3389/fchem.2021.809415
- Samaneh Inanlou, Rodrigo Cortes-Meija, **Ali Deniz Özdemir**, Sebastian Höfener, Wim Klopper, Wolfgang Wenzel, Weiwei Xie, Marcus Elstner. Understanding excited state properties of host materials in OLEDs: simulation of absorption spectrum of amorphous 4,4-bis(carbazol-9-yl)-2,2-biphenyl (CBP). Phys. Chem. Chem. Phys., 2022, 24, 4576
- **Ali Deniz Özdemir**, Samaneh Inanlou, Franz Symalla, Weiwei Xie, Wolfgang Wenzel, Marcus Elstner. Dynamic Effects on Hole Transport in Amorphous Organic Semiconductors: a Combined QM/MM and kMC Study. J. Chem. Theory Comput. 2023, 19, 13, 3849–3860
- **Ali Deniz Özdemir**, Fabian Li, Franz Symalla, Wolfgang Wenzel. In silico studies of OLED device architectures regarding their efficiency. Front. Phys. 11:1222589. 2023

Supervised scientific theses

- Masterthesis, Niklas Kappel, *Molecular Flexibility in Monte Carlo Simulations of Amorphous Organic Solids*, 2022
- Bachelorthesis, Fabian Li, *Kinetic Monte-Carlo Studies of different OLED Architectures*, 2023
- Masterthesis, Oliver Petkau, *Simulation of Organic Semiconductors with High Charge Carrier Concentrations*, 2024

Acronyms

B3LYP Becke 3-parameter Lee–Yang–Parr 26, 29

COM center-of-mass 58, 63, 71–74

CT charge transfer 38, 48

DDM drift-diffusion model 43, 44

DFT density functional theory 3, 16, 22, 26, 28, 29, 32, 53, 56

DFTB density functional tight-binding 3, 16, 26, 28–31, 51, 53, 57, 77, 118

EIL electron injection layer 12

EL electroluminescent 1, 7

EML emissive layer 12, 14, 15, 81, 82, 92, 98, 99, 106, 108, 111, 112, 114, 119

ETL electron transport layer 12, 82

GAFF general Amber force field 35, 55

HF Hartree-Fock 3, 16, 18, 22, 25, 26, 28, 56

HIL hole injection layer 12

HOMO highest occupied molecular orbital 3, 4, 11, 12, 27, 29, 30, 39, 41, 42, 44, 51, 56, 57, 60–63, 65, 69–71, 77, 79, 114, 118–120

HPC high performance computing 21

HTL hole transport layer 12, 82

IQE internal quantum efficiency 80, 87, 88

ISC intersystem crossing 9

KMC kinetic Monte-Carlo 3, 4, 39, 43, 46–49, 53, 81, 96, 98, 99, 101–106, 108, 110–113, 116, 118–121

KS Kohn-Sham 3

LCAO linear combination of atomic orbitals 20, 27

LUMO lowest unoccupied molecular orbital 11, 12, 39, 41, 42, 114, 119

MC Monte-Carlo 32, 106, 109

MD molecular dynamics 3, 32, 35, 51, 53, 55, 56, 58, 70, 75, 118

ME Master equation 43–45, 47

OLED organic light-emitting diode 2–4, 7–10, 13, 16, 80, 97, 99, 118–120

OLEDs organic light emitting diodes 1, 7, 11, 13, 15, 16, 98, 117–119

OSC organic semiconductors 1–3, 6, 7, 46, 50, 51, 79

PES potential energy surface 17, 38

PVD physical vapor deposition 13, 32

RISC reverse intersystem crossing 11

SA simulated annealing 34, 53, 55

SCF self-consistent field 3, 16, 21, 28

SPQ singlet-polaron quenching 99

SSA singlet-singlet annihilation 15, 98

STA singlet-triplet annihilation 15, 98

TADF thermally activated delayed fluorescence 11, 13

TPQ triplet-polaron quenching 14, 15, 92, 98, 99, 119

TSA triplet-singlet annihilation 98

TTA triplet-triplet annihilation 14, 15, 92, 98, 119

Contents

List of Figures

1 Introduction

For over seventy years, organic electronics has persisted as a dynamic area of study, consistently drawing scientific interest as a potential substitute for silicon and gallium arsenide-based electronics. Central to organic electronics is the utilization of hydrocarbon-based molecules, commonly referred to as OSC, as the fundamental constituents for electronic devices. One of the most fascinating aspects of OSC lies in the vast expanse of potential chemical compounds, offering a virtually limitless variety of chemical and physical properties. This rich diversity provides researchers with an opportunity to explore and synthesize compounds tailored to exhibit specific sets of properties ideal for various applications. Consequently, the ability to custom-design compounds to meet precise requirements opens up new avenues for innovation and advancement across numerous fields [1].

Nonetheless, organic materials lagged significantly behind conventional inorganic semiconductors in terms of longevity and performance. A significant milestone occurred in 1987 when Tang and VanSlyke [2], researchers at Kodak laboratories, achieved a breakthrough with the demonstration of an electroluminescent device based on organic compounds. This event marked the start of the development of practical organic light emitting diodes (OLEDs). Despite lower electroluminescent (EL) efficiency than traditional LEDs, organic devices have attracted considerable attention because of their potential for diverse applications stemming from their inherent mechanical flexibility. This flexibility is especially interesting for applications like curved displays, foldable phones, and creative lighting solutions (shown in Figure 1.1). These factors serve as substantial market catalysts, driving the extensive commercialization of OLED technology within the display industry. Market forecasts reveal a projected global market volume for OLED technology reaching 260 billion USD by 2032, as emphasized in [3], thereby under-

scoring the significant impact of OLEDs.
Furthermore, OLEDs provide another crucial advantage with their low energy consumption, a feature of utmost significance considering that approximately 15% of global energy consumption is allocated to lighting, contributing to 5% of worldwide greenhouse gas emissions [4], highlighting the importance of further improvements in OLED technology and general OSC materials.

Figure 1.1: Flexible OLED-display. Picture taken from [5]. Copyright 2024 Fluxim AG.

Despite the advancements made in recent decades, OSC and organic light-emitting diode (OLED) technology continue to face challenges such as low carrier mobility and short lifetimes, leaving room for enhancing device efficiency and lifetime. When considering the vast array of materials and potential device structures, it becomes evident that relying solely on experimental work is highly time and resource intensive. This is where theoretical and computational models come into play, offering crucial insights into material and architecture bottlenecks.
In contrast to perfectly crystalline inorganic semiconductors, where electron transport can be described by the well-established band-transport theory, this framework is only applicable to OSC with minimal structural disorder. However, in amorphous thin-film OSC, structural and energetic disorder results in the localization of electronic states on individual molecules. Consequently, charge carriers primarily move between neighboring molecules, a phenomenon known as hopping transport. Heinz Bässler used the concept of percolation paths for charge transport across multiple molecules, a concept that remains widely accepted in the field to this day [6]. Developing a comprehensive model capable of fully elucidating charge and exciton transport in amorphous OSCs is exceptionally challenging, mainly due to the multi-scale nature of the problem. This endeavor necessitates integrating diverse methods from various fields to bridge the relevant scales effectively. It begins with accurately describing the electronic structure of individual molecules, which operates at the sub-nanometer scale, and extends to understand-

ing their interactions within their respective environments. However, conducting a quantum-chemical analysis of entire amorphous thin-films, comprising millions of molecules, is practically infeasible. The next challenge arises when attempting to simulate charge transport across numerous molecules, where charges navigate through what are referred to as percolation paths within the organic solid. These paths can extend up to several micrometers [7, 8]. The complexity intensifies even further when aiming to simulate entire OLED devices. This is because charge carriers must traverse multiple thin-films composed of different materials and interact with carriers of opposite sign to form excitons. These excitons, subsequently, may either move within the system or undergo various decay channels, adding another layer of intricacy to the simulation.
In my thesis, I will address three topics related to OSC and OLED modeling across different length and timescales. This ranges from quantum mechanical studies of dynamic effects on electronic structure and transport parameters in amorphous organic layers, to in-depth kinetic Monte-Carlo (KMC) analyses of multilayered OLED devices focusing on efficiency loss mechanisms, and finally to long-timescale degradation simulations examining the effects of intrinsic molecular degradation on device performance. The structure of this thesis is organized as follows:

Chapter 2 presents a detailed overview of the fundamental operating principles of OLED devices. Essential concepts related to device efficiency are introduced, followed by a concise discussion of the materials and manufacturing techniques applied in practice.

In Chapter 3, I discuss the computational tools pertinent to this work. Starting with electronic structure methods, from the Hartree-Fock (HF) approximation to describe the self-consistent field (SCF) algorithm, followed by the discussion of the Kohn-Sham (KS) approach within density functional theory (DFT). Subsequently, the semi-empirical density functional tight-binding (DFTB) method, which was extensively used in Chapter 4, is introduced and explained in more detail. After discussing electronic structure methods, the DEPOSIT protocol for generating amorphous organic structures [9] is introduced. This is followed by a brief overview of employing molecular dynamics (MD) to simulate structural fluctuations within these structures. Lastly, a theoretical examination of charge and exciton transport in amorphous organic layers is presented. This understanding serves as the basis for employing the KMC method in OLED simulations.

In Chapter 4, the computational tools discussed earlier are utilized to investigate dynamic effects on the electronic structure of amorphous organic morphologies. The primary focus is on understanding the origin of energetic disorder by analyzing both its static and dynamic contributions, while also examining the influence of fluctuating intermolecular couplings. The study further explores how these dynamic phenomena impact hole mobility within amorphous structures. An interesting observation has been made regarding dynamic disorder in organic materials. It has been observed that materials with a highest occupied molecular orbital (HOMO) that is delocalized across many rotatable groups tend to show a relatively high contribution of dynamic disorder to the total disorder. Conversely, in

molecules where the primary components of the HOMO are localized on non-movable parts, the contribution of dynamic disorder is significantly smaller. This gives hints on how the electronic structure of single molecules has to be, in order to reduce the dynamic disorder in complicated amorphous solids. Such an ad-hoc prediction for the static disorder based solely on single molecular properties is very challenging due to the complexity of the deposition process and intermolecular interactions that lead to the disordered morphology. Therefore, the explicit differentiation between static and dynamic disorder presented here offers insights into effectively reducing overall disorder by focusing on mitigating dynamic disorder of the molecules comprising the structure.

Chapter 5, focuses on conducting comprehensive OLED simulations aimed at identifying architecture bottlenecks that contribute to efficiency roll-off. This investigation employed a parametric toy model to represent the microscopic structure and simulation parameters, allowing for a systematic exploration of various architecture designs. Through extensive KMC simulations, it is demonstrated how effective this approach is in efficiently pinpointing drawbacks associated with specific device architectures and proposing optimization strategies to enhance device efficiency across a broad spectrum of operational conditions. The results of this study reveal that implementing exciton-blocking layers between the hole transport and emissive layer, as well as between the electron transport and emissive layer, coupled with an increased thickness of the emissive layer, leads to a significant reduction in efficiency roll-off in OLEDs. This exploration underscores the practical applications of simulation-driven design for enhancing OLED performance and addressing critical efficiency-related challenges. By leveraging simulation tools and parametric modeling, this work showcases how theoretical insights can guide experimental efforts toward optimizing device architectures and achieving more stable and efficient OLEDs.

In Chapter 6, a modified version of the KMC approach was implemented to account for exciton-quenching based degradation processes and the potential destruction of individual sites within the device. This study is instrumental in determining whether host or emitter degradation predominates in limiting the lifetimes of OLED devices. Throughout this investigation, it became evident that simulating realistic device lifetimes using KMC requires employing several methodological improvements. The first strategy involves a post-simulation adjustment of the system time, where KMC steps corresponding to quenching and subsequent degradation are corrected using single molecular parameters, considering molecular stability and a factor reflecting the frequency of quenching events at individual sites. This factor is influenced by device architecture and operational conditions and had to be parameterized by preparatory KMC simulations. The approach enabled the simulation of lifetime curves for OLEDs with low emitter concentrations. However, for higher emitter concentrations resulting in lower current densities, this method was impractical within reasonable KMC simulation times. A second methodological improvement involved using only a fraction of the degradation simulation to model the fraction of intact molecules over time and to extrapolate the behavior of the device over extended operational periods. This modeling approach was validated by comparing the resulting luminance curves with those

obtained from explicit degradation simulations. The findings from this study highlight that in OLEDs employing typical iridium-based phosphorescent emitter molecules, the primary limiting factor for device lifetimes appears to be degradation of the host molecules within the emissive layer. This insight underscores the importance of understanding and mitigating degradation mechanisms to enhance the stability and longevity of OLED devices, particularly those employing phosphorescent emitters. The methodological innovations applied in this research contribute valuable tools for assessing and predicting device lifetimes under realistic operating conditions.

2

Organic semiconductors & OLEDs

Organic semiconductors (OSC) are organic solids exhibiting semiconducting properties. They primarily consist of carbon and hydrogen, often with additional heteroatoms such as nitrogen, oxygen, or heavier elements. Some cases may also involve heavy metal complexes with special photophysical characteristics. When discussing semiconducting behavior, one typically considers how conductivity increases with temperature by thermally exciting electrons from the valence band to the conduction band, thereby creating mobile charge carriers—a well-known phenomenon in inorganic semiconductors. In typical inorganic semiconductors, band gaps range from 0.67 eV (Ge) to 1.1 eV (Si) up to 1.4 eV (GaAs) [10].
Unlike their inorganic counterparts, intrinsic conductivity of organic semiconductors is absent, necessitating the generation of mobile carriers through extrinsic processes like charge injection, doping, or photoexcitation followed by charge separation. Another notable distinction is the dielectric constant—typically $\epsilon_r = 11$ in inorganic semiconductors, effectively screening Coulomb interactions, versus $\epsilon_r = 3.5$ in organic OSC, leading to stronger Coulomb interactions among mobile carriers. This characteristic significantly impacts applications such as organic photovoltaic (OPV) devices where efficient separation of excitons (bound electron-hole pairs) is essential. To make OSC appealing for electronic applications, they must allow carrier injection from common contact materials like Indium Tin Oxide (ITO) for hole injection or Aluminum (Al) for electron injection. For utilization in display applications, OSC must also exhibit a band gap within the visible light spectrum. These requirements are fulfilled by π-conjugated materials [11, 12]. OSC can be categorized into three main classes: (i) organic crystals, (ii) polymer films, and (iii) amorphous organic films, each possessing distinct properties.
In amorphous organic films and organic crystals, which consist of molecules typically with a molecular

mass below 1000 atomic units, the bonding between molecules is primarily of the van der Waals type [13]. This, combined with a disordered structure, results in lower carrier mobilities compared to inorganic semiconductors, leading to higher layer resistance. However, OSC devices can be build from thin films (approximately 200 nm), which helps to reduce the overall resistance [14]. Crystalline OSCs have better mobility compared to disordered OSCs but are usually very fragile and challenging to fabricate in electronic devices and to contact with electrode materials. In contrast, amorphous films are easier to handle, and importantly, the fabrication of mixed films, such as in conductivity doping [15, 16], or blending molecules with desired photophysical properties for more efficient emission, can be achieved. This is why amorphous structures are more interesting for technical applications and are focus of this work.

2.1 Fundamentals of OLEDs

OLEDs are electronic devices incorporating amorphous OSC that exhibit EL characteristics, emitting light in response to electric current [17]. The basic process of generating light involves electrons and holes recombining to form an exciton (an electron-hole pair), followed by the emission of a photon through radiative decay. Over the past few decades, there has been remarkable progress in the development of efficient OLEDs achieved through the optimization of materials and device architectures [18].

2.1.1 Historical development

In the 60s, organic EL devices consisted of single-layer architectures where an organic layer (often crystalline Anthracene) was positioned between an anode for hole injection and a cathode for electron injection [19, 20]. However, these single-layer devices exhibited the significant drawback of requiring high operation voltages, resulting in poor power-conversion efficiency. Attempts were made to lower the operating voltage by depositing thinner layers of Anthracene; nevertheless, these modifications still resulted in low quantum efficiency [21]. This was mainly explained by inefficient electron injection causing charge imbalance inside the organic layer. In 1987, Tang and VanSlyke made a significant breakthrough by implementing a bilayer organic structure between an indium tin oxide anode and a magnesium-silver alloy cathode, which notably enhanced the EL performance [2].
The device exhibited IV characteristics similar to conventional diodes, where under forward bias (with the positive terminal of the external voltage source connected to the anode and the negative terminal at the cathode), high current densities and light emission were observed. This behavior can be attributed to the hole injection barrier between the anode and the first organic layer composed of TPD, as well as the injection barrier between the second organic layer (made of Alq3) and the cathode (see Figure 2.1). These injection barriers can only be overcome by forward biasing, facilitating carrier injection at the electrodes. Conversely, under reverse bias, these barriers become stronger, effectively blocking the injection of holes and electrons. This achievement marked the beginning of modern-day OLED technology.

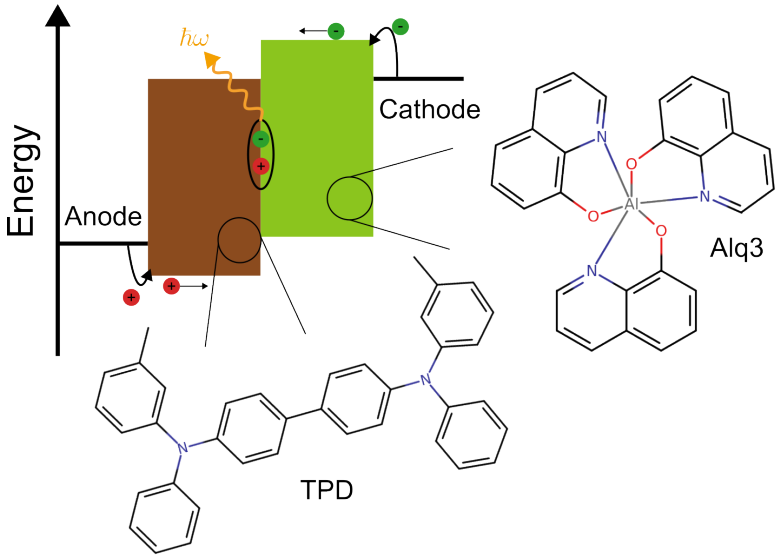

Figure 2.1: Schematic representation of a Tang and VanSlykes OLED. Under forward bias, electrons and holes are injected at the anode and cathode, respectively. The compound Alq3 was used as electron injection and transport material. At the anode a diamine was used similar to shown in the figure (TPD).

Figure 2.1 illustrates the working principle of the device, showing how injected carriers recombine at the interface between the organic layers, resulting in photon emission. Compared to modern OLED devices, the early device developed by Tang and VanSlyke exhibited a relatively low external quantum efficiency of approximately 1% [2]. Since then, efficiencies have significantly improved [22, 23]. In the following section, the concept of external quantum efficiency will be defined.

2.1.2 External quantum efficiency

The external quantum efficiency η_{ext} of an OLED is determined by the fraction of injected electrons and holes that result in emitted photons without being absorbed by the device material. Tetsuo Tsutsui introduced this concept, which is defined by four factors [24]:

$$\eta_{\text{ext}} = \gamma \cdot \eta_{\text{r}} \cdot \eta_{\text{PL}} \cdot \eta_{\text{out}} \tag{2.1}$$

where γ represents the charge balance factor, η_{r} denotes recombination efficiency, η_{PL} denotes photoluminescence efficiency, and η_{out} refers to the outcoupling efficiency. Each of these four factors is the focus of research efforts aimed at maximizing the external quantum efficiency.
The charge balance factor γ reflects the necessity for an electron and a hole to recombine into an exciton, which can be hindered by asymmetric transport properties between electrons and holes, leading to non-ideal ambipolar carrier transport [25]. The Photoluminescence efficiency η_{PL} quantifies the effectiveness

of light emission via radiative decay of excitons. This decay process competes with non-radiative pathways, typically influenced by strong exciton-phonon coupling [26] or exciton-quenching [27, 28]. After generation, the photons need to be extracted from the device. The outcoupling efficiency η_{out} measures the fraction of photons that are successfully extracted [29, 30]. The first three factors are commonly denoted as the internal quantum efficiency:

$$\eta_{\text{int}} = \gamma \cdot \eta_{\text{r}} \cdot \eta_{\text{PL}} \,. \tag{2.2}$$

The recombining electron and hole carry a spin of $1/2$ and $-1/2$, respectively [14]. After the process of recombination, excitons can exist in four possible spin states: one state with a total spin of zero, known as singlet, and three states with a total spin of 1, collectively termed triplets. The spin contributions to the excitonic wavefunctions for singlet and triplet states are illustrated in Figure 2.2. Due to spin statistics, 25% of formed excitons will be singlets, while the remaining 75% will be triplets. Devices that exclusively rely on fluorescent emission, where singlet excitons decay into the electronic ground state by emitting a photon, are inherently limited to an internal quantum efficiency of 25%. The introduction of phosphorescent emitters by Baldo et al. [31] marked a second breakthrough in OLED technology, enabling a theoretical internal quantum efficiency of 100%. A more detailed discussion of light emission mechanisms in organic materials is given in the next section.

2.1.3 Light emission mechanisms

As previously discussed, only one-fourth (25%) of the formed excitons are singlets. The early generations of OLEDs relied on fluorescent emitter materials, which could only emit light from singlet excitons [2, 32]. This limitation resulted in a theoretical internal quantum efficiency of 25%, translating to an external quantum efficiency of around 5% in practice. In the late 90s, it was demonstrated that phosphorescent materials could enhance the internal quantum efficiency up to 100%. Baldo et al. blended phosphorescent emitter molecules into an organic matrix and showed a strong increase in the internal quantum efficiency [31, 33, 34]. This is attributed to the fact on phosphorescent emitters, both singlets and triplets can radiatively decay [35, 36, 26, 37]. The singlets can undergo radiative decay through either a fluorescent pathway or via intersystem crossing (ISC) to a triplet state, followed by phosphorescent emission [38]. A fast ISC-rate however, requires strong spin-orbit coupling between the singlet and triplet states. Also the phosphorescence emission rate ω_{phos} strongly depends on the spin-orbit coupling which was demonstrated by McGlynn et al. [39]. The phosphoresence emission rate is proportional to the quadratic spin-orbit coupling:

$$\omega_{\text{phos}} \propto \frac{|\langle \psi_{\text{S}_1} | \hat{H}_{\text{SO}} | \psi_{\text{T}_1} \rangle|^2}{(\Delta E_{\text{S}_1-\text{T}_1})^2}. \tag{2.3}$$

This implies that strong spin-orbit coupling in phosphorescent emitters is essential. Purely organic materials typically lack significant spin-orbit couplings [40], rendering them unsuitable as emitters in OLEDs. Therefore, phosphorescent emitter molecules often incorporate heavy-metal elements such as

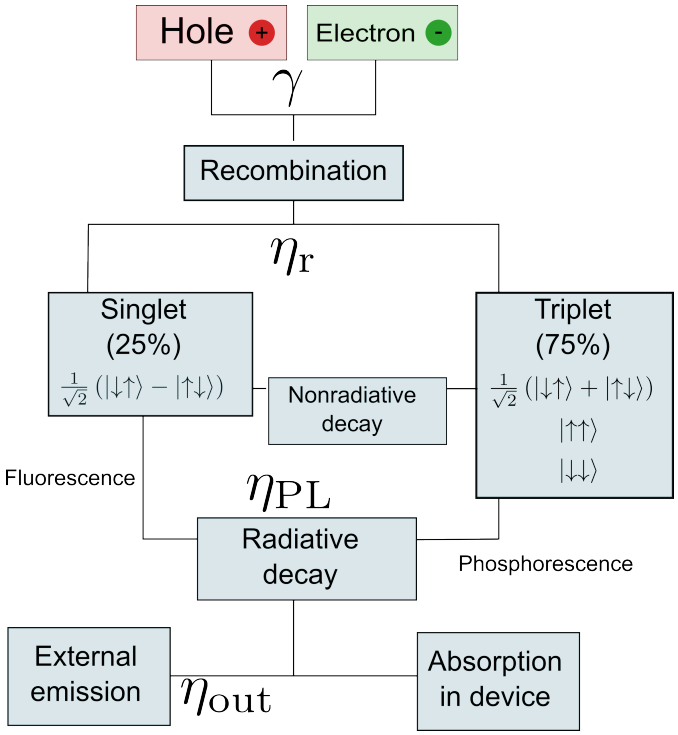

Figure 2.2: Scheme for the external quantum efficiency. Injected holes and electrons recombine to form singlet or triplet excitons, which subsequently undergo either radiative or non-radiative decay processes. For radiative decay, the resulting photon must exit the device, a process referred to as external emission. These sequential steps collectively determine the overall external quantum efficiency of an OLED.

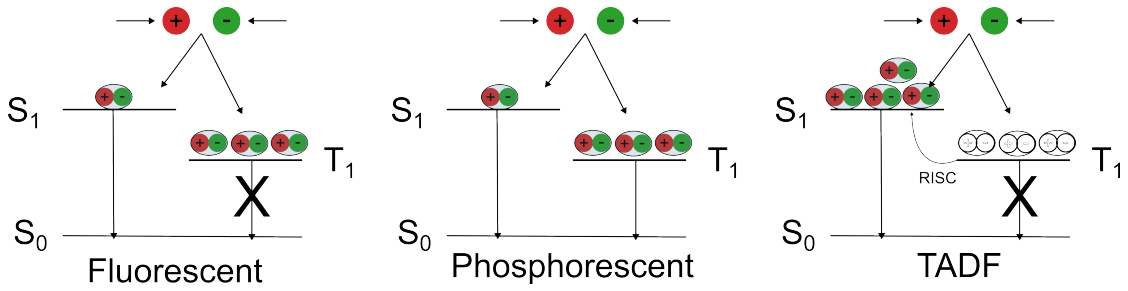

Figure 2.3: Emitter generations. On the left side, the diagram illustrates the principle of fluorescent emitters in OLEDs. Only 25% of the formed excitons are singlet-type, explaining why fluorescent emitters have a theoretical limit for internal quantum efficiency of 25%. In the center, employing phosphorescent emitters raises the theoretical limit to 100%. These emitters can harvest all formed excitons by leveraging strong spin-orbit coupling to convert singlet excitons into triplets. The triplet excitons can then decay radiatively through phosphorescence. A critical requirement for phosphorescent emitters is strong spin-orbit coupling, which is typically not achievable with purely organic materials. On the right side, TADF molecules do not necessitate strong spin-orbit coupling because they transform triplet excitons back into singlet excitons through reverse intersystem crossing, instead of undergoing radiative decay from the triplet state. This transformation allows them to emit regular fluorescence. A key condition here is a small singlet-triplet energy gap.

Pt or Ir [41]. Despite the widespread adoption of phosphorescence-based OLEDs in commercial applications, they are burdened by certain drawbacks including high production costs, toxicity associated with heavy metal atoms, and challenges in developing stable blue phosphorescent emitters [42]. In 2012, Uyama et al. [43] introduced an alternative approach aiming to achieve a theoretical internal quantum efficiency of 100% using thermally activated delayed fluorescence (TADF) molecules.

TADF molecules enable efficient conversion of triplet excitons back to singlet states through processes called reverse intersystem crossing (RISC), assuming negligible phosphorescence rates in purely organic materials due to weak spin-orbit coupling. Subsequently, these singlet excitons can undergo regular fluorescence decay. This process requires a competitive RISC rate compared to the non-radiative decay rate, which is closely related to achieving a very small singlet-triplet energy gap ($\Delta E_{S_1-T_1}$). In Figure 2.3 depicts the three generations of emitters and their operational principles.

2.2 Modern OLED devices

Over time, efforts to improve OLED efficiency have included not only utilizing phosphorescent or TADF emitters to harvest triplets but also advancing device architectures by incorporating additional layers [18, 44]. The introduction of extra organic layers was aimed at overcoming specific drawbacks, resulting in OLEDs with a multilayered structure where each layer was designed to address particular limitations or challenges. A standard schematic representation of a multilayer OLED device typically includes an energy diagram depicting the HOMO and lowest unoccupied molecular orbital (LUMO) levels of each layer. An example of such a multilayer device is illustrated in Figure 2.4, where the materials used for

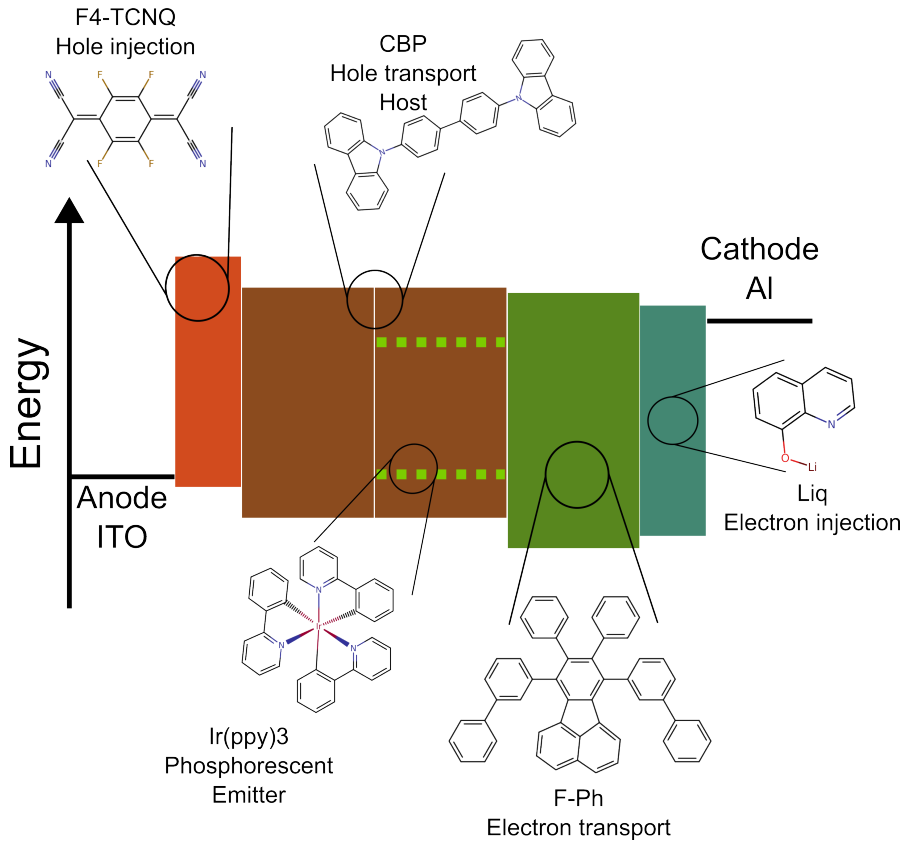

Figure 2.4: Energy diagram of a multilayer OLED. The energies of the HOMO and LUMO are indicated by the lower or upper edge of each layer. The device structure, from left to right, includes an anode, a hole injection layer, followed by a hole transport layer and an emissive layer where phosphorescent emitters are doped into a host matrix. Next is the electron transport layer, followed by the electron injection layer, with the cathode located at the end of the device.

each layer are also indicated. As an example, a hole injection layer (HIL) can be incorporated between the anode and the subsequent organic layers to reduce the injection barrier and enhance injection efficiency [45]. Similarly, an electron injection layer (EIL) can be utilized to enhance electron injection efficiency at the cathode. These injection layers are followed by either hole transport layer (HTL) or electron transport layer (ETL), which serve to transport the carriers to the emissive layer (EML) located at the center of the device. In Figure 2.4, the material used for the HIL is F4-TCNQ [45]. The materials Liq and F-PH are employed for the EIL and ETL, respectively, as described in [46]. The HTL and the host material within the EML are composed of CBP, with Ir(ppy)3 being utilized as phosphorescent emitter [47]. The device configuration and materials illustrated in Figure 2.4 represent just one example within a nearly limitless space of compound and architecture combinations.

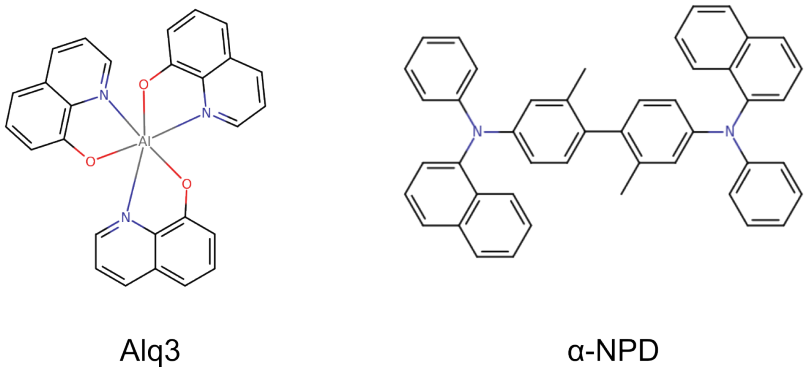

Figure 2.5: Chemical structure of Alq3 and α-NPD

2.2.1 Device manufacturing

When fabricating multilayer OLEDs using small organic molecules (with a molecular weight below 1000 atomic units), the most commonly used method is physical vapor deposition (PVD) due to the superior thermal stability of these molecules compared to larger polymers [48]. The fabrication process begins with a glass substrate that is precoated with an indium tin oxide anode. Subsequently, the organic molecules are deposited layer by layer by evaporating them in a vacuum chamber and allowing them to condense onto the substrate. PVD is a time-consuming process, giving amorphous OSC films a significant disadvantage compared to alternative technologies such as Liquid Crystal Displays (LCDs) or plasma-based panels, which offer faster manufacturing processes. Attempts to increase the deposition rate can negatively impact the physical properties of the deposited film. For instance, in the case of Alq3, increasing the deposition rate led to worsened electron mobility and increased total power consumption [49]. Matsushima et al. conducted a comprehensive investigation into the effects of deposition rates on the optical and electrical properties of two different materials: α-NPD and Alq3 (Figure 2.5). The findings suggest that high deposition rates can have both positive and negative effects on conductivity, as depicted in Figure 2.6. While the conductivity of α-NPD slightly improves with high deposition rates, it drastically decreases for Alq3. This highlights the challenge of identifying materials that can withstand and benefit from higher deposition rates. Navigating this complexity in material selection is crucial for optimizing device performance following thin film deposition processes.

2.3 Efficiency roll-off

Despite significant advancements in OLED technology over the past decades, challenges persist, particularly in achieving high luminance at high current densities without efficiency losses and reduced device lifetime. Earlier, I discussed how incorporating phosphorescent or TADF emitters into OLEDs theoretically allows for internal quantum efficiency up to 100%, but practical efficiency falls short of this. One immediate challenge is efficiency roll-off, where efficiency decreases with increasing current density. A major contributor to efficiency roll-off are excitonic quenching events [51].

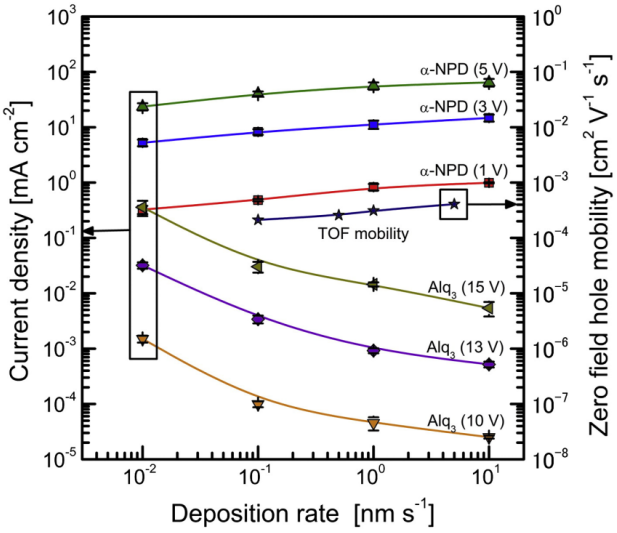

Figure 2.6: Effect of deposition rate. For α-NPD, a higher deposition rate results in a slight improvement in transport performance. However, for Alq3, high deposition rates lead to a significant decrease in transport properties and consequently affect device performance negatively. Reprinted from [50]. Copyright 2024, with permission from Elsevier.

In phosphorescent emitters, although phosphorescence efficiency is relatively high, triplet lifetimes (few µs) are much longer than singlet lifetimes (few ns). This extended triplet exciton lifetime introduces another issue, as excitons can diffuse through the matrix and quench either by interacting with other excitons or with charge carriers (polarons). The most prevalent quenching processes are triplet-polaron quenching (TPQ)[1] and triplet-triplet annihilation (TTA), which significantly reduce internal quantum efficiency at high current densities [38, 27, 52]. In general, all these quenching events result in the loss of an exciton by transferring its excess energy to the quenching partner [53]. At high operation voltages, the overall carrier density increases, leading to a higher exciton density, particularly within the EML. The rise in exciton density automatically increases the likelihood of exciton-exciton or exciton-polaron quenching which explains the efficiency roll-off.

2.3.1 Triplet-triplet annihilation (TTA)

When a donor and acceptor molecule are both in their lowest triplet excited state (T_1), TTA involves the energy transfer from the triplet state of the donor to the excited acceptor molecule. This results in the donor returning to its electronic ground state (S_0), while the acceptor is left in either its first triplet- or singlet-excited state (S_1). The mechanism can be described by:

$$T_1 + T_1 \xrightarrow{\omega_{\mathrm{TTA}}} X \begin{cases} \xrightarrow{75\%} T_n + S_0 \rightarrow T_1 + S_0 \\ \xrightarrow{25\%} S_n + S_0 \rightarrow S_1 + S_0 \end{cases} \tag{2.4}$$

[1] Charge carriers are frequently called polarons because of the Coulomb-induced polarization of their surroundings.

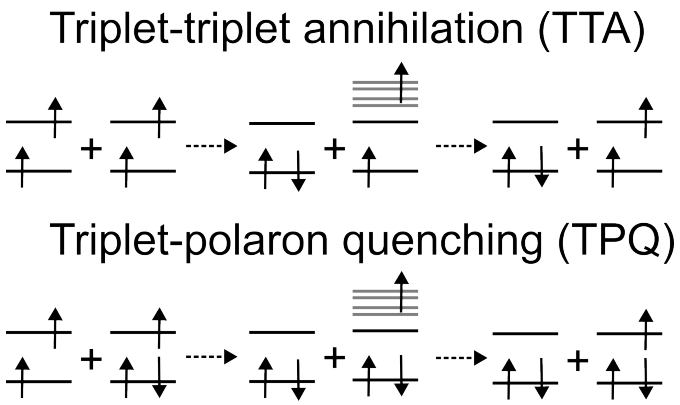

Figure 2.7: Schematic illustrations of TTA (top) and TPQ (bottom). In the case of TTA, the intermediate state of the acceptor molecule is shown in a high triplet state, as described in equation (2.4). For TPQ, the illustration demonstrates triplet-electron quenching.

As discussed by Murawski et al. [38], TTA leads to an intermediate state X. From this state, the acceptor molecule can transition either to an energetically high triplet state (T_n) or singlet state (S_n), which then thermally relax back to the lowest triplet or singlet states, respectively. The highly excited intermediate state of the acceptor molecule can trigger molecular degradation, for instance by bond breaking [54, 55, 56, 57, 58, 59]. In guest-host systems such as the EML, TTA can occur among guests (emitter molecules), among hosts (host matrix), and between guests and hosts. Singlet excitons can undergo quenching with other singlets through singlet-singlet annihilation (SSA) as discussed in [60, 61], or with other triplets through singlet-triplet annihilation (STA) as studied in [62, 63, 64]. These processes resemble TTA and can be formally described in a similar manner.

2.3.2 Triplet-polaron quenching (TPQ)

TPQ is also a significant contributor to efficiency roll-off in OLEDs [27, 65]. Similar to equation (2.4), TPQ can be formally expressed as [38]:

$$T_1 + h^+ \xrightarrow{\omega_{\mathrm{TPQ}}} S_0 + h^{+*} \rightarrow S_0 + h^+ \tag{2.5}$$

$$T_1 + e^- \xrightarrow{\omega_{\mathrm{TPQ}}} S_0 + e^{-*} \rightarrow S_0 + e^- \,. \tag{2.6}$$

In this mechanism, the excited donor molecule transfers its energy to a molecule that has either a hole or an electron, creating an intermediate state where the charged molecule becomes highly excited. This excited state then quickly decays back to its original state through thermal processes, effectively leading to the disappearance of the initial exciton [27].

3

Theoretical background & computational methods

Computational investigations in the realm of organic semiconductors and OLEDs apply theoretical principles spanning various length and time scales. In this chapter, I aim to provide a brief summary of the theories, methods, and implementations utilized in this thesis. Beginning with electronic structure calculations, wherein the molecular Schrödinger equation must be approximately solved to gain insights into molecular energy levels and intermolecular couplings. To facilitate comprehension, I will commence with one of the conceptually simplest methods, the HF approximation. Although mainly serving as an educational example, it aids in introducing fundamental concepts such as the basis set and SCF procedure. Subsequently, I will delve into the fundamentals of DFT to establish a groundwork for understanding DFTB, a method extensively utilized in this thesis.
Furthermore, I will provide a brief overview of the field of computational modeling of amorphous organic thin films and the theory of charge and exciton transport. Lastly, I will review various computational methods employed to model these processes in OLED devices.

3.1 Electronic Structure of Molecular Systems

In the domain of material science and computational chemistry, electronic structure theory stands out as a primary discipline. Within this field, atomic units emerge as the prevailing unit system:

$$\frac{\hbar^2}{m_e} = 4\pi\epsilon_0 = e = 1 \ .$$

The cornerstone of electronic structure theory lies in the molecular Hamiltonian, which, for a molecule composed of N electrons and M nuclei, is formulated as follows:

$$\begin{aligned} \hat{H} &= \hat{T}_\mathrm{e} + \hat{V}_\mathrm{en} + \hat{V}_\mathrm{ee} + \hat{V}_\mathrm{nn} \\ &= -\frac{1}{2}\sum_i^N \nabla_i^2 - \sum_I^M \sum_i^N \frac{Z_I}{|\boldsymbol{r}_i - \boldsymbol{R}_I|} + \frac{1}{2}\sum_{i\neq j}^N \frac{1}{|\boldsymbol{r}_i - \boldsymbol{r}_j|} + \sum_{I\neq J}^M \frac{Z_I Z_J}{|\boldsymbol{R}_I - \boldsymbol{R}_J|} \qquad (3.1) \\ &= \hat{H}_\mathrm{e} + \hat{V}_\mathrm{nn} \ . \qquad (3.2) \end{aligned}$$

The summation index for electrons is denoted by lowercase letters i and j, while capital letters represent summation over nuclei.
The first term, $\hat{T}_\mathrm{e}$, signifies the kinetic energy operator of the electrons, whereas the second term, $\hat{V}_\mathrm{en}$, denotes the Coulomb attraction between electrons and nuclei. The third term, $\hat{V}_\mathrm{ee}$, signifies the electron-electron interaction, while the last term, $\hat{V}_\mathrm{nn}$, represents the nuclei-nuclei repulsion. Notably, the kinetic energy of the nuclei is absent from consideration.
The Hamiltonian (3.1) is formulated under the Born-Oppenheimer approximation [66]. This approximation exploits the considerable mass disparity between nuclei and electrons, allowing the treatment of electrons as moving within the field of the nuclei with fixed positions. As a result, the kinetic energy of the nuclei is neglected, and the interaction between nuclei $\hat{V}_\mathrm{nn}$ is a constant.
The eigenfunctions of the electronic Schrödinger equation:

$$\hat{H}_\mathrm{e}\Psi_\mathrm{e}(\{\boldsymbol{r}_i\},\{\boldsymbol{R}_I\}) = E_\mathrm{e}(\{\boldsymbol{R}_I\})\Psi_\mathrm{e}(\{\boldsymbol{r}_i\},\{\boldsymbol{R}_I\}) \qquad (3.3)$$

are the electronic wavefunctions Ψ that explicitly depend on the positions of the electrons, while nuclei positions enter the wavefunctions as parameters. Also the corresponding eigenvalues E_e depend parametrically on the nucleonic positions.
The total molecular energy in Born-Oppenheimer approximation is the given by:

$$E_\mathrm{tot} = E_\mathrm{e}(\{\boldsymbol{R}_I\}) + \frac{1}{2}\sum_{I\neq J}^M \frac{Z_I Z_J}{|\boldsymbol{R}_I - \boldsymbol{R}_J|} \ . \qquad (3.4)$$

The total energy constitutes a hypersurface in the space of nucleonic positions, commonly referred to as the potential energy surface (PES). The goal of electronic structure theory is to establish a theoretical framework for addressing the electronic Schrödinger equation (3.3). Due to the inherent complexity of

this problem, analytical solutions are generally not feasible. Thus, the approach involves: i) Developing theoretical approximations to the electronic problem. ii) Implementing these approximations into computer programs to transform the task of solving the electronic Schrödinger equation approximately into solving numerical problems.
Such approximate methods can be broadly categorized into two fundamentally different approaches: wavefunction-based methods, where an ansatz for the electronic wavefunction is made to render the problem solvable, and density-based methods. Both types of methods find applications in practice, and providing an in-depth survey of all methods would be beyond the scope of this thesis.

3.1.1 Hartree Fock Theory

As previously mentioned, the HF-theory is a wavefunction-based method, which is rooted the theory of molecular orbitals. Similar to the concept of orbitals used in atomic physics, molecular orbitals describe the electronic structure of molecules. Mathematically, this involves decomposing the many-electron wavefunction $\Psi_e(\{\boldsymbol{r}_i\})$ into a series of uncorrelated single-electron functions, referred to as molecular orbitals ψ_i. In the following, I will omit the subscript "e" to denote that I am discussing electronic wavefunctions. To preserve the antisymmetry of the many-electron wavefunction, the Slater determinant is employed:

$$\Psi(\boldsymbol{x}_1,\ldots,\boldsymbol{x}_N) = \frac{1}{\sqrt{N!}}\begin{vmatrix} \psi_1(\boldsymbol{x}_1) & \psi_2(\boldsymbol{x}_1) & \ldots & \psi_N(\boldsymbol{x}_1) \\ \psi_1(\boldsymbol{x}_2) & \psi_2(\boldsymbol{x}_2) & \ldots & \psi_N(\boldsymbol{x}_2) \\ \vdots & \vdots & \ddots & \vdots \\ \psi_1(\boldsymbol{x}_N) & \psi_2(\boldsymbol{x}_N) & \ldots & \psi_N(\boldsymbol{x}_N) \end{vmatrix} . \tag{3.5}$$

To be more precise, the single-particle functions ψ_i are better referred to as spin-orbitals rather than molecular orbitals because they also incorporate the spin as a degree of freedom:

$$\psi_i(\boldsymbol{x}_i) = \varphi_i(\boldsymbol{r}_i)\cdot\xi(\sigma_i) \tag{3.6}$$

$$\boldsymbol{x}_i = (\boldsymbol{r}_i,\sigma_i)\,. \tag{3.7}$$

where $\xi_i(\sigma_i)$ denotes the spin wavefunction of the electron as a function of a dummy variable σ_i. The electrons spin can either be spin-up or spin-down. The spatial contribution $\varphi_i(\boldsymbol{r}_i)$ is a function of space. The electronic energy can now be obtained by:

$$E = \langle\Psi|\hat{H}|\Psi\rangle = \sum_i^N \langle\psi_i|\hat{h}(\boldsymbol{r}_i)|\psi_i\rangle + \frac{1}{2}\sum_{i,j}^N\left(\langle\psi_i\psi_j|\frac{1}{|\boldsymbol{r}_i-\boldsymbol{r}_j|}|\psi_i\psi_j\rangle - \langle\psi_i\psi_j|\frac{1}{|\boldsymbol{r}_i-\boldsymbol{r}_j|}|\psi_j\psi_i\rangle\right), \tag{3.8}$$

where in the last term, electron i and j was exchanged. The minus sign is a consequence of the antisymmetric many electron wavefunction. All operators in the Hamuiltonian that only act on single electrons

are written in the compact form:

$$\hat{h}(\boldsymbol{r}_i) = -\frac{1}{2}\nabla_i^2 - \sum_I^M \frac{Z_I}{|\boldsymbol{r}_i - \boldsymbol{R}_I|} \,. \tag{3.9}$$

In the subsequent step, the spin orbitals ψ_i must be selected to minimize the energy, in accordance with the variational principle. This minimization process is carried out under the boundary condition of orthonormal molecular orbitals:

$$\begin{aligned} \left\langle \psi_i \middle| \psi_j \right\rangle &= \int \mathrm{d}\boldsymbol{x}\ \psi_i^*(\boldsymbol{x})\psi_j(\boldsymbol{x}) \\ &= \int \mathrm{d}\sigma\ \xi_i^*(\sigma)\xi_j(\sigma) \int \mathrm{d}\boldsymbol{r}\ \varphi_i^*(\boldsymbol{r})\varphi_j(\boldsymbol{r}) \\ &= \delta_{ij}\,, \end{aligned} \tag{3.10}$$

indicating the orthogonality of the spin and spatial contributions to the spin-orbital.
By minimizing the energy (3.8) with given boundary conditions one finds the following equation for the spin-orbital ψ_i:

$$\left[\hat{h}(\boldsymbol{r}_i) + \sum_j^N (\hat{J}_j - \hat{K}_j)\right] \psi_i(\boldsymbol{x}_i) = \varepsilon_i \psi_i(\boldsymbol{x}_i) \,. \tag{3.11}$$

The differential equation for a single electron introduced above is known as the Hartree-Fock equation. The operators introduced, $\hat{J}_j$ and $\hat{K}_j$, are termed the Coulomb and exchange operators, respectively. Acting on spin orbital ψ_i they yields:

$$\hat{J}_j \psi_i(\boldsymbol{x}_i) = \int \mathrm{d}\boldsymbol{x}'\ \frac{|\psi_j(\boldsymbol{x}')|^2}{|\boldsymbol{r}_i - \boldsymbol{r}'|} \psi_i(\boldsymbol{x}_i) \tag{3.12}$$

$$\hat{K}_j \psi_i(\boldsymbol{x}_i) = \int \mathrm{d}\boldsymbol{x}'\ \frac{\psi_j^*(\boldsymbol{x}')\psi_i(\boldsymbol{x}')}{|\boldsymbol{r}_i - \boldsymbol{r}'|} \psi_j(\boldsymbol{x}_i) \,. \tag{3.13}$$

The Coulomb operator evaluates the Coulombic interaction between an electron in spin-orbital i and the electrostatic potential arising from the electron in spin-orbital j. The exchange operator measures the energy necessary for exchanging an electron between spin-orbital i and spin-orbital j.
Given that only closed-shell molecules are the focus of Chapter 4, after integrating over all spin degrees of freedom, the closed-shell restricted Fock operator can be defined as follows:

$$\hat{F}(\boldsymbol{r}_i) = \hat{h}(\boldsymbol{r}_i) + \sum_j^{N/2} \left[2\hat{J}_j - \hat{K}_j\right] , \tag{3.14}$$

leading to the restricted Hartree-Fock equation:

$$\hat{F}(\boldsymbol{r}_i)\varphi_i(\boldsymbol{r}_i) = \varepsilon_i\varphi_i(\boldsymbol{r}_i)\,. \tag{3.15}$$

The factor ε_i serves as the Lagrange multiplier, arising from the boundary condition in the variational optimization process. It can be interpreted as the energy associated with molecular orbital i.
I no longer use spin-orbitals because the definition of the restricted Fock operator includes integration over all spin degrees of freedom, and now I employ the spatial component φ_i, which is refered to as molecular orbitals. It is noteworthy that when electrons possess antiparallel spin, the exchange energy becomes zero. This clarifies why there is no factor of 2 preceding the exchange operator.

Introducing a basis set

To render the Hartree-Fock approximation suitable for implementation in computer programs and for conducting practical electronic structure calculations, additional approximations are necessary, particularly concerning the molecular orbitals. In nearly all prevalent quantum chemistry softwares, the linear combination of atomic orbitals (LCAO) method is applied:

$$\varphi_i(\boldsymbol{r}_i) = \sum_{I}^{M}\sum_{\mu\in a}^{K_I} c_{\mu I i}\chi_{I\mu}(\boldsymbol{r}_i - \boldsymbol{R}_I)\,. \tag{3.16}$$

A molecule comprising M atoms, where each atom I possesses K_I orbitals, can be expressed as a sum of atom-centered atomic orbitals $\chi(\boldsymbol{r} - \boldsymbol{R}_I)$.
For instance, considering the Hydrogen atom, at least one atomic orbital with 1s-character would be necessary to represent the electronic structure (minimal basis set). For an isolated Lithium atom, the minimum number of basis functions would be 2, with one representing 1s-character and the other representing 2s-character. Similarly, for an H2 molecule, a minimum of 2 basis functions would be required, with one 1s-like atomic orbital for each hydrogen atom.
In general, the only atom for which an exact solution of the atomic orbitals is known is the isolated Hydrogen atom. Using the radial behavior as a template, atomic orbitals for other atoms can be constructed similarly. This involves representing the angular parts using spherical harmonics and the radial part using an exponential decay function $\propto \exp(-\zeta r)$, where ζ dictates the decay length and r denotes the distance from the atom. These atomic orbitals are termed Slater-type orbitals.
In practice, however, the radial part is often represented by a Gaussian function instead. The primary reason for this choice is that many integrals encountered in calculations can be solved much faster and more straightforwardly when Gaussian-type orbitals are employed.
To simplify the following equations, I will not explicitly sum over atoms I and their orbitals. Instead, I will use μ as a generalized index where both summations are already included. Additionally, I will not explicitly specify the atom-centered character. Consequently, the number of atomic orbitals for a

molecule is given by $K = M \cdot K_I$, and the molecular orbital in terms of atomic orbitals is expressed as:

$$\varphi_i(\boldsymbol{r}) = \sum_{\mu}^{K} c_{\mu i} \chi_\mu(\boldsymbol{r}) \,, \tag{3.17}$$

where the summation over index μ now denotes a summation of all orbitals of all atoms constituting the molecule. Each molecular orbital has one set of coefficients $c_{\mu i}$.

Self-consistent field calculation

By introducing of a basis set (3.17), the Hartree-Fock equation (3.15) can be written as:

$$\hat{F}(\boldsymbol{r}_i) \sum_{\nu} c_{\nu i} \chi_\nu(\boldsymbol{r}_i) = \varepsilon_i \sum_{\nu} c_{\nu i} \chi_\nu(\boldsymbol{r}_i) \,. \tag{3.18}$$

Multiplying with $\chi_\mu(\boldsymbol{r}_i)^*$ from the left and integrating over space yields:

$$\sum_{\nu} F_{\mu\nu} c_{\nu i} = \sum_{\nu} S_{\mu\nu} c_{\nu i} \varepsilon_i \,, \tag{3.19}$$

with the Fock matrix

$$F_{\mu\nu} = \int \mathrm{d}\boldsymbol{r}\ \chi_\mu^*(\boldsymbol{r}) \hat{F}(\boldsymbol{r}) \chi_\nu(\boldsymbol{r}) \tag{3.20}$$

and the ovrerlap matrix

$$S_{\mu\nu} = \int \mathrm{d}\boldsymbol{r}\ \chi_\mu^*(\boldsymbol{r}) \chi_\nu(\boldsymbol{r}) \,. \tag{3.21}$$

This equation can be expressed in matrix form, and for each molecular orbital index i, we obtain the Roothan equations in matrix form:

$$\boldsymbol{F}\boldsymbol{c} = \boldsymbol{S}\boldsymbol{c}\boldsymbol{\varepsilon} \tag{3.22}$$

where $\boldsymbol{F}$ and $\boldsymbol{S}$ are $K \times K$ matrices defined as described earlier, $\boldsymbol{\varepsilon}$ is the diagonal matrix $\mathrm{diag}[\varepsilon_1, \ldots, \varepsilon_K]$, containing the molecular orbital energies, and $\boldsymbol{c}$ is the coefficient matrix.
The Roothan equations (3.22) have now been transformed into matrix equations, which can be efficiently solved using high performance computing (HPC). The output provides the coefficient matrix and the orbital energies for a given molecular structure.
Recalling the definitions of the Fock operator (3.14) and the Coulomb and exchange operators (3.12) and (3.13), it becomes apparent that the Fock operator, and consequently the Fock matrix in the basis of atomic orbitals, depends on the molecular orbitals (or spin-orbitals), and thus also on the coefficients $\boldsymbol{F} = \boldsymbol{F}(\boldsymbol{c})$ that we seek to determine.
To address this challenge, one employs the SCF approach. Initially, an estimate for the coefficients is

made, then the generalized eigenvalue equation (3.22) is solved, the Fock operator is recalculated with the newly computed coefficients, and this process is repeated iteratively until the coefficient matrix converges.

3.1.2 Density Functional Theory

The HF approximation is a method used to tackle the numerical solution of the many-electron Schrödinger equation via a wave function-based approach. While HF-computed energies capture significant portions of the total energy, they lack what is known as correlation energy. This deficiency arises from treating Coulomb interaction between electrons in a mean-field manner, where each electron interacts with the averaged electrostatic potential from all other electrons. Consequently, Coulomb-induced electron correlations are neglected.

For many applications, the accuracy of the HF approximation proves insufficient, necessitating the use of more sophisticated methods to incorporate correlation energy. Various approaches exist, ranging from perturbative methods to extensions of the wave function approach, such as Configuration Interaction and Coupled Cluster methods [67, 68].

A different strategy for addressing this issue does not rely on the many-electron wave function, a complex mathematical object, but instead utilizes a more intuitive observable: the electron density, denoted as $n(\boldsymbol{r})$. This approach expresses the total energy in terms of the electron density, denoted as $E[n(\boldsymbol{r})]$, giving rise to DFT. The foundation of DFT lies in the Hohenberg-Kohn theorems [69], which assert that: i) there exists a unique correspondence between the ground-state electron density and the external potential, which, in this context, refers to the electron-nuclei interaction term, and ii) the true electron density minimizes the energy.

The first Hohenberg-Kohn theorem implies that the electron density serves as a unique descriptor for each molecular structure. Meanwhile, the second theorem resembles the variational principle, which states that the correct wavefunction minimizes the total energy—a principle implicitly utilized in the discussion of the HF equation (3.15).

Understanding how the energy can be formulated as a functional of the electron density and gaining insight into the practical implementation of DFT calculations are crucial topics to discuss. This is because DFT serves as the foundational framework for later approximations utilized to make the work presented in chapter 4 feasible.

Electron density

The relation between the electron density and the many-electron wavefunction is given as:

$$n(\boldsymbol{r}) = N \int \mathrm{d}\sigma \int \mathrm{d}\boldsymbol{x}_2 \ldots \boldsymbol{x}_N \, |\Psi(\boldsymbol{r}, \sigma, \boldsymbol{x}_2, \ldots, \boldsymbol{x}_N)|^2 \,, \tag{3.23}$$

where $n(\boldsymbol{r})\,\mathrm{d}\boldsymbol{r}$ is interpreted as the probability to find an electron $\boldsymbol{r}$. Note that if one omits the single integration over the spin degrees of freedom σ one could define a spin-polarized electron density $n_\sigma(\boldsymbol{r})$

which is useful in some cases [70].
In a similar manner, one can define the pairwise electron density as:

$$n^{(2)}(\boldsymbol{r},\boldsymbol{r}') = \frac{N(N-1)}{2}\int \mathrm{d}\sigma\,\mathrm{d}\sigma' \int \mathrm{d}\boldsymbol{x}_3\ldots\boldsymbol{x}_N\,|\Psi(\boldsymbol{r},\boldsymbol{r}',\sigma,\sigma',\boldsymbol{x}_3,\ldots\boldsymbol{x}_N)|^2\,. \tag{3.24}$$

The probability of finding an electron at position $\boldsymbol{r}$ while another electron is positioned at $\boldsymbol{r}'$ is represented by $n^{(2)}(\boldsymbol{r},\boldsymbol{r}')\mathrm{d}\boldsymbol{r}\mathrm{d}\boldsymbol{r}'$. This encompasses the full electron correlation, contributing to the complexity of solving the Schrödinger equation. One can separate the complicated correlation part from the uncorrelated contributions to the pairwise density in the following way:

$$n^{(2)}(\boldsymbol{r},\boldsymbol{r}') = \frac{1}{2}n(\boldsymbol{r})n(\boldsymbol{r}') + \Delta n^{(2)}(\boldsymbol{r},\boldsymbol{r}')\,, \tag{3.25}$$

where if one would neglect the second term one describes uncorrelated electrons. The correction includes corrections coming from correlation.

Energy as a density functional

The objective now is to represent the expectation value of the molecular Hamiltonian defined in equation (3.1) as a functional of the electron density. This can be achieved by expressing the contributing terms as such a functional.
With the provided definitions, the electron-nuclei interaction expressed as a functional of the electron density can be written as:

$$\begin{aligned} E_{\mathrm{en}}[n] &= \langle\Psi|\,\hat{V}_{\mathrm{en}}\,|\Psi\rangle \\ &= \int \mathrm{d}\boldsymbol{r}\,\sum_I^M \frac{(-Z_I)}{|\boldsymbol{r}-\boldsymbol{R}_I|}n(\boldsymbol{r}) \\ &= \int \mathrm{d}\boldsymbol{r}\,v_{\mathrm{ext}}(\boldsymbol{r})n(\boldsymbol{r})\,, \end{aligned} \tag{3.26}$$

where the external potential $v_{\mathrm{ext}}(\boldsymbol{r})$ is defined.
The electron-electron interaction can be expressed as:

$$\begin{aligned} E_{\mathrm{ee}}[n] &= \langle\Psi|\,\hat{V}_{\mathrm{ee}}\,|\Psi\rangle \\ &= \int \mathrm{d}\boldsymbol{r}\,\mathrm{d}\boldsymbol{r}'\frac{n^{(2)}(\boldsymbol{r},\boldsymbol{r}')}{|\boldsymbol{r}-\boldsymbol{r}'|} \\ &= \frac{1}{2}\int \mathrm{d}\boldsymbol{r}\,\mathrm{d}\boldsymbol{r}'\frac{n(\boldsymbol{r})n(\boldsymbol{r}')}{|\boldsymbol{r}-\boldsymbol{r}'|} + \Delta E_{\mathrm{ee}}[n]\,, \end{aligned} \tag{3.27}$$

where the last term represents the correlation-induced corrections to the electron-electron interaction.

The kinetic energy term cannot be expressed as a functional of the electron density due to the in-

volvement of second-order derivatives in the expectation value of the kinetic energy operator. This challenge is particularly pronounced for correlated many-electron wavefunctions. To address this, Kohn and Sham proposed separating the intricate correlation effects on kinetic energy from those that can be captured by uncorrelated motion. This led to the introduction of Kohn-Sham orbitals ψ_i^{KS}, facilitating the representation of kinetic energy [71, 72]:

$$T[n] = -\frac{1}{2}\sum_{i}^{N}\left\langle \psi_i^{\mathrm{KS}}\middle|\nabla_i^2\middle|\psi_i^{\mathrm{KS}}\right\rangle + \Delta T[n]\,. \tag{3.28}$$

The first term represents the kinetic energy of non-interacting particles, while the second term serves as a correction to account for correlation effects. Much like the spin orbitals employed in HF-theory, Kohn-Sham orbitals consist of both spin and spatial components, are orthonormal, and crucially, enable the computation of the true electron density. These orbitals mimic non-correlated particles moving within an auxiliary system featuring an effective potential.
The electron density can be obtained by:

$$n(\boldsymbol{r}) = \sum_{i=1}^{N} |\psi_i^{\mathrm{KS}}(\boldsymbol{r})|^2\,. \tag{3.29}$$

For simplicity, I will refer to Kohn-Sham orbitals as just ψ_i.
Combining all terms together, we reach the total energy in the following form:

$$E[n] = -\frac{1}{2}\sum_{i=1}^{N}\langle\psi_i|\nabla_i^2|\psi_i\rangle + \int \mathrm{d}\boldsymbol{r}\; v_{\mathrm{ext}}(\boldsymbol{r})n(\boldsymbol{r}) + \frac{1}{2}\int \mathrm{d}\boldsymbol{r}\,\mathrm{d}\boldsymbol{r}'\frac{n(\boldsymbol{r})n(\boldsymbol{r}')}{|\boldsymbol{r}-\boldsymbol{r}'|} + \Delta T[n] + \Delta E_{\mathrm{ee}}[n] + E_{\mathrm{nn}}\,. \tag{3.30}$$

The challenge of incorporating electron correlation effects into the total energy is now addressed through the two correction terms. When combined, they form what is known as the exchange-correlation functional.

$$E_{\mathrm{XC}}[n] = \Delta T[n] + \Delta E_{\mathrm{ee}}[n]\,. \tag{3.31}$$

The primary challenge in the many-electron problem now lies in determining the exact form of the exchange-correlation functional, which remains unknown.

Kohn-Sham Equations

Applying the variational principle to the total energy (3.30), one finds the Kohn-Sham equations:

$$\left(-\frac{1}{2}\nabla_i^2 + v_{\mathrm{ext}}(\boldsymbol{r}) + \int \mathrm{d}\boldsymbol{r}'\frac{n(\boldsymbol{r}')}{|\boldsymbol{r}-\boldsymbol{r}'|} + \frac{\delta E_{\mathrm{XC}}[n]}{\delta n}\right)\psi_i(\boldsymbol{r}) = \varepsilon_i\psi_i(\boldsymbol{r})\,, \tag{3.32}$$

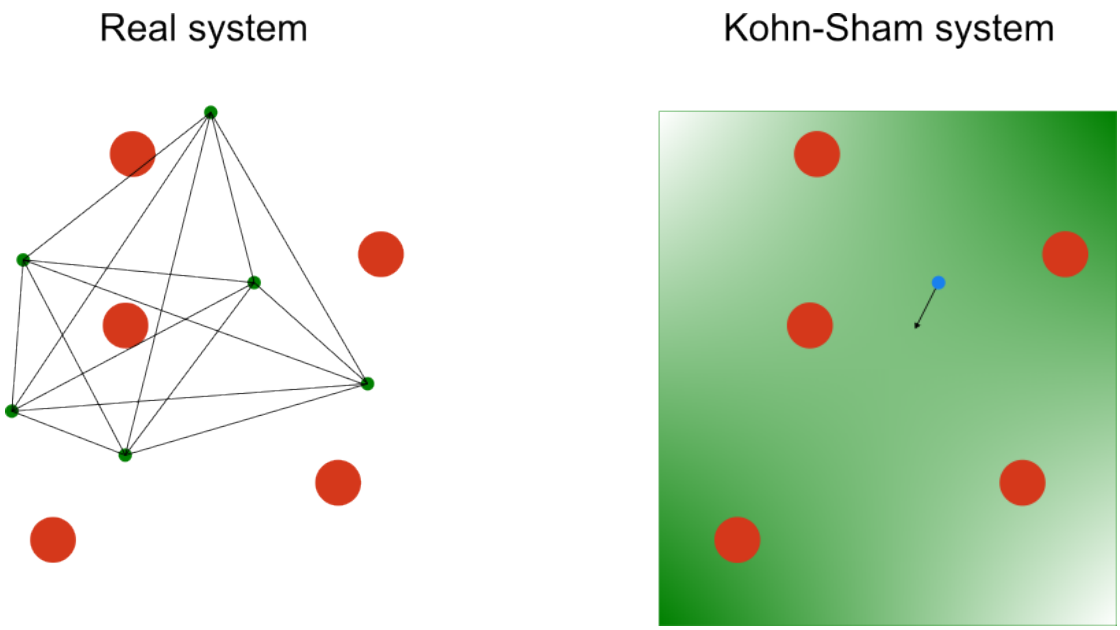

Figure 3.1: Kohn-Sham auxiliary system. On the left side a molecular system with nuclei (red circles) and interacting electrons (green circles) is shown. Each electron interacts with all other electrons and the interactions are shown with the connection lines. The Kohn-Sham approach replaces the real system with an ficticious system where single electron like particles (blue circle) move in an effective potential $v_{\text{eff}}(\boldsymbol{r})$.

which are single particle wave-equations, similar to the HF-equatios (3.15) with the main difference of incorperating correlation effects by means of the exchange correlation functional.
To solve Kohn-Sham equations again the SCF procedure (3.22) presented before can be applied.
The last term represents the functional derivative of the exchange-correlation functional with respect to the electron density. The effective potential seen by the non-interacting electrons is given by:

$$\begin{aligned} v_{\text{eff}}(\boldsymbol{r}) &= v_{\text{ext}}(\boldsymbol{r}) + \int \mathrm{d}\boldsymbol{r}' \frac{n(\boldsymbol{r}')}{|\boldsymbol{r}-\boldsymbol{r}'|} + \frac{\delta E_{\text{XC}}[n]}{\delta n} \\ &= v_{\text{ext}}(\boldsymbol{r}) + v_{\text{H}}(\boldsymbol{r}) + v_{\text{XC}}(\boldsymbol{r}) \end{aligned} \tag{3.33}$$

and depends on the exchange-correlation functional employed.
Figure 3.1 shows a schematic presentation on how the realistic interaciting system is replaced by the Kohn-Sham auxiliary system.

Exchange correlation functionals

In principle, solving the Kohn-Sham equations could lead to exact energies if the true form of the exchange-correlation functional was known. However, this is not the case, and approximations must be used. Over the past decades, numerous developments, ranging from simple to more advanced ap-

proximations for exchange-correlations, have been made.
Starting with the Local Density Approximation (LDA), where the functional depends solely on the electron density $E_{\mathrm{XC}}^{\mathrm{LDA}}[n(\boldsymbol{r})]$, and progressing to the Generalized Gradient Approximation (GGA), which also considers the first spatial derivative $E_{\mathrm{XC}}^{\mathrm{GGA}}[n(\boldsymbol{r}), \nabla n(\boldsymbol{r})]$, and to very advanced hybrid functionals where parts of the exchange energy incorporate the HF exchange energy.
One particularly prominent functional is Becke 3-parameter Lee–Yang–Parr (B3LYP), which has been successfully utilized in describing the electronic structure of organic molecules [73].
The B3LYP functional combines components from other functionals, with each part having its own weighting factor typically determined through fitting to very accurate high level methods [74].

3.1.3 Density Functional Theory Tight Binding

Over the past decades, DFT has risen as one of the most utilized quantum chemical methods, finding applications even in industrial research and development. However, the effectiveness of DFT is also contingent upon the size of the system under study, as it scales with K^3, where K denotes the number of basis functions required to represent the system. This highlights that the computational expenses associated with DFT can become exceedingly high for large systems, such as bio-molecules or, as pertinent to our context, amorphous organic solids consisting of thousands of small organic molecules. This is where highly efficient semi-empirical quantum chemisty methods like DFTB come into play.
The method of choice for the study presented in Chapter 4 is DFTB, an approximation of the standard DFT discussed previously. In this section, I aim to elucidate the main concepts and principles underlying the DFTB method, elucidate its distinctions from conventional DFT, and expound on its application in electronic structure calculations pertinent to this study.
The first concept underlying DFTB is to decompose the true electron density as follows[75]:

$$n(\boldsymbol{r}) = n_0(\boldsymbol{r}) + \delta n(\boldsymbol{r}) \,, \tag{3.34}$$

where $n_0(\boldsymbol{r})$ resembles the electron density as it would be if all atoms composing the molecule or solid were free and no charge transfer occurred due to covalent bonds. The correction term δn is assumed to be small. In the standard DFTB scheme, the energy functional is expanded around the reference density n_0 up to the second order of the correction term. The approximated energy reads

$$\begin{aligned} E[n_0] &= \sum_{i=1}^{N} \left\langle \psi_i \middle| -\frac{1}{2}\nabla^2 + v_{\mathrm{ext}}(\boldsymbol{r}) + \int \mathrm{d}\boldsymbol{r}' \frac{n(\boldsymbol{r}')}{|\boldsymbol{r}-\boldsymbol{r}'|} + v_{\mathrm{XC}}[n_0] \middle| \psi_i \right\rangle + E_{\mathrm{Rep}} + \frac{1}{2}\int \mathrm{d}\boldsymbol{r}\,\mathrm{d}\boldsymbol{r}' \left(\frac{\delta^2 E_{\mathrm{XC}[n_0]}}{\delta n \delta n'} + \frac{1}{|\boldsymbol{r}-\boldsymbol{r}'|} \right) \\ &= \sum_{i=1}^{N} \left\langle \psi_i \middle| \hat{H}[n_0] \middle| \psi_i \right\rangle + E_{\mathrm{rep}} + E_{\mathrm{Coulomb}}[\delta n] \\ &= E_{\mathrm{BS}}[n_0] + E_{\mathrm{rep}} + E_{\mathrm{Coulomb}}[\delta n] \,. \end{aligned} \tag{3.35}$$

In the electronic structure calculations carried out for this study, only the first two terms, the so-called bandstructure energy E_{BS} and the repulsive energy E_{rep} [75], directly influenced the results. The con-

tribution from all second-order expansion terms in δn played only an indirect role, being utilized solely for the parameterization of the repulsive energy, as described by:

$$E_{\text{rep}} = -\frac{1}{2}\int \mathrm{d}\boldsymbol{r}\; v_{\text{H}}[n_0]n_0(\boldsymbol{r}) + E_{\text{XC}}[n_0] + E_{\text{nn}} - \int \mathrm{d}\boldsymbol{r}\; v_{\text{XC}}[n_0]n_0(\boldsymbol{r})\,. \tag{3.36}$$

It is named as such because it incorporates the nuclei-nuclei repulsion term. In the subsequent section, I will briefly outline the computation of the bandstructure energy and the derivation of the repulsive term.

Matrix elements

Once more, closed-shell systems are considered, allowing us to assume that all spatial contributions to the molecular orbital are doubly occupied up to the HOMO. Thus, one can rewrite the bandstructure energy as:

$$E_{\text{BS}}[n_0] = \sum_{i=1}^{N/2} 2\,\langle\varphi_i|\hat{H}[n_0]|\varphi_i\rangle\,. \tag{3.37}$$

Applying the LCAO as already discussed in (3.17), one finds:

$$E_{\text{BS}}[n_0] = \sum_{i=1}^{N/2} 2c_{\mu i}c_{\nu i}H^0_{\mu\nu}\,. \tag{3.38}$$

To determine the orbital coefficients, one must once again solve a set of algebraic equations, which take the following form:

$$\sum_{\nu}\left(H^0_{\mu\nu} - \varepsilon_i S_{\mu\nu}\right)c_{\nu i} = 0\,, \tag{3.39}$$

where the matrix elements are given by

$$H^0_{\mu\nu} = \int \mathrm{d}\boldsymbol{r}\; \chi_\mu(\boldsymbol{r})\hat{H}[n_0]\chi_\nu(\boldsymbol{r}) \tag{3.40}$$

$$S_{\mu\nu} = \int \mathrm{d}\boldsymbol{r}\; \chi_\mu(\boldsymbol{r})\chi_\nu(\boldsymbol{r})\,. \tag{3.41}$$

A crucial aspect of atomic basis sets is that they utilize only a minimal basis set for the matrix elements, and solely the valence electrons are taken into account. The core electrons are incorporated into the repulsive energy.
As our goal is to compute electrons that are tightly bound in a solid or molecule, using atomic orbitals from free atoms would not be suitable due to their diffusive nature. Instead, orbitals from pseudo-atoms are utilized. This is achieved by solving a single atomic Schrödinger equation and introducing a confining potential to attain a more appropriate distance behavior of the atomic orbitals for subsequent

applications.
In practice, the basis functions of the pseudo-atoms are acquired by solving the following Schrödinger equation:

$$\left(-\frac{1}{2}\nabla^2 + \frac{Z}{|r|} + v_{\mathrm{XC}}(\boldsymbol{r}) + v_{\mathrm{H}}(\boldsymbol{r}) + v_{\mathrm{conf}}(\boldsymbol{r})\right)\chi^{\mathrm{p}}(\boldsymbol{r}) = \varepsilon^{\mathrm{p}}\chi^{\mathrm{p}}(\boldsymbol{r})\,, \tag{3.42}$$

where the confining potential uses a cutoff distance as parameter and has the following form:

$$v_{\mathrm{conf}}(\boldsymbol{r}) = \left(\frac{r}{r_{\mathrm{cutoff}}}\right)^2\,. \tag{3.43}$$

The pseudo-atom Schrödinger equation is frequently solved using standard Density Functional Theory (DFT) employing the PBE functional.
The confined atomic orbitals obtained are then utilized to compute the matrix elements of the Hamiltonian (3.40) and the overlap matrix (3.41). This process is performed for atomic pairs of different elements, including both homonuclear and heteronuclear pairs, at various distances. The resulting integrals are stored in Slater-Koster files, allowing for easy lookup and eliminating the need for recalculation.
In traditional DFT (or HF), the molecular structure is initialized, an initial guess for the coefficients of the molecular orbitals is made, followed by computation of the first-guess density. Subsequently, the Kohn-Sham Hamiltonian and the matrix elements, involving numerous integrations over the Gaussian basis functions, are computed. The coefficient matrix equation (3.22) is then solved, and this process is repeated until convergence is achieved. This iterative procedure involves multiple cycles where the matrices need to be recomputed at each step.
In contrast, in DFTB with tabulated integrals, the molecular structure, comprising all atoms composing the molecule, is read, and for each atomic pair, the integrals for the Hamiltonian and overlap matrix are retrieved from the tabulated integrals. The algebraic equation can then be solved to obtain the orbital coefficients and molecular orbital energies. This streamlined process eliminates the need for the SCF procedure, making the DFTB approach much faster.

Repulsive term

The repulsive energy is a highly intricate term encompassing not only the nuclei-nuclei repulsion but also components of the exchange-correlation energy. Following the philosophy of DFTB, the repulsive term is represented by a simpler mathematical expression, which is subsequently parametrized based on higher-level calculations. This process resembles the parametrization of the matrix elements described earlier.
The repulsive term is written as

$$E_{\mathrm{rep}} = \frac{1}{2}\sum_{I,J} V_{IJ}^{\mathrm{rep}}[n_{0I}, n_{0J}, R_{IJ}]\,. \tag{3.44}$$

In the provided expression, the summation indices denote different atoms within the molecule or solid. V^{rep} signifies a pairwise potential that relies on the reference densities of atoms I and J as well as their mutual distance R_{IJ}.

Next, pairwise energies are computed using a reference method, typically a Density Functional Theory (DFT) calculation, to create a scan of energy versus atomic distances. The repulsive energy is then determined by this scan and can be expressed as follows:

$$V_{IJ}^{\text{rep}}(R_{IJ}) = \left(E_{\text{ref}}(R_{IJ}) - E_{\text{el}(r_{IJ})}\right) + E_{\text{IJ}}^{\text{shift}} \,, \tag{3.45}$$

where, E_{ref} represents the reference energy, E_{el} denotes the electronic energy obtained from the DFTB calculation, encompassing the Coulomb term but excluding the repulsive term, and E_{IJ}^{rep} accounts for any global offset between the reference energy and the DFTB energy. For the calculations in this work, the so-called MIO-parametrization was used. There, the reference method was DFT with a B3LYP functional and 6-31G(d) basis set [76, 77, 78].
However, in practice, instead of fitting energies, forces between atoms are typically employed for fitting purposes.

Calculation of couplings

A decisive parameter in the modelling of charge transfer between small organic molecules is the so-called electronic coupling. In most of the hopping transport models the hopping rate depends on the absolute square of the electronic couplings. The calculation of the coupling though is far from straight forward and many methods are used to do this. The coupling for hole transfer between two chemically identical closed shell molecule plays a crucial role for the work presented in chapter 4 which is I want to present the method to compute the coupling that was applied in this work.
A fundamental concept underlying the coupling involves the notion of diabatic states Ψ_a and Ψ_b, where state a signifies the hole located on the donor molecule D while the acceptor A remains charge-neutral. Due to the relatively weak coupling between organic molecules, it is a valid approximation to express the diabatic states as a combination of spin-orbitals localized on either the donor ψ_i^{D} or acceptor ψ_i^{A}. One can conceptualize this as a $2N-1$ electron system where an electron is absent in the donor (resulting in a hole), and the acceptor is in a neutral charge state. After hole transfer, the donor molecule becomes neutral, and the hole resides at the acceptor molecule.
The diabatic state before charge transfer is given by:

$$\Psi_a = \frac{1}{\sqrt{(2N-1)!}} |\psi_1^{\text{D}}(\boldsymbol{x}_1) \dots \psi_{N-1}^{\text{D}}(\boldsymbol{x}_{N-1}) \psi_1^{\text{A}}(\boldsymbol{x}_N) \dots \psi_N^{\text{A}}(\boldsymbol{x}_{2N-1})| \,. \tag{3.46}$$

Here, $|\dots|$ denotes the Slater determinant of the single-particle spin-orbitals. The Highest Occupied Molecular Orbital (HOMO) of the donor orbital is only half-occupied, as indicated by the occupation of spin orbitals up to ψ_{N-1}^{D}. Conversely, the spin orbitals of the acceptor are fully occupied. Following

charge transfer, the $2N-1$ electrons are redistributed such that the donor returns to a closed-shell configuration, while the acceptor assumes an open-shell configuration.
The diabatic state b reads:

$$\Psi_b = \frac{1}{\sqrt{(2N-1)!}} |\psi_1^{\mathrm{D}}(\boldsymbol{x}_1)\dots\psi_{N-1}^{\mathrm{D}}(\boldsymbol{x}_{N-1})\psi_1^{\mathrm{A}}(\boldsymbol{x}_N)\dots\psi_N^{\mathrm{D}}(\boldsymbol{x}_{2N-1})| \,. \tag{3.47}$$

The electron $2N-1$ jumped from the HOMO of the acceptor to the HOMO of the donor $\psi_N^D(\boldsymbol{x}_{2N-1})$.
The electronic coupling can be computed as

$$\begin{aligned} H_{ab} &= \langle\Psi_a|\hat{H}_{\mathrm{e,dimer}}|\Psi_b\rangle \\ &\approx \langle\Psi_a|\hat{H}_{\mathrm{DFTB1}}|\Psi_b\rangle \\ &= \left\langle\psi_N^{\mathrm{A}}\middle|\hat{H}_{\mathrm{DFTB1}}\middle|\psi_N^{\mathrm{D}}\right\rangle . \end{aligned} \tag{3.48}$$

In this context, the electronic Hamiltonian of the dimer is approximated using the DFTB1 Hamiltonian discussed earlier, and the Slater-Condon rules are employed for the evaluation of matrix elements. Since the Slater determinants differ by only one state, the resulting expression simplifies to an integral over the Highest Occupied Molecular Orbital (HOMO) orbitals of the donor and acceptor molecules.
However, a remaining issue arises from the non-orthogonality of spin orbitals between two distinct molecules. To fully account for electronic coupling, it is advantageous to work within an orthonormal basis.
This can be achieved by representing the Schrödinger equation of the dimer in matrix form [79]:

$$\begin{pmatrix} H_{aa} & H_{ab} \\ H_{ba} & H_{bb} \end{pmatrix}\begin{pmatrix} c_a \\ c_b \end{pmatrix} = E\begin{pmatrix} 1 & S \\ S & 1 \end{pmatrix}\begin{pmatrix} c_a \\ c_b \end{pmatrix}$$
$$\boldsymbol{H}\boldsymbol{c} = E\boldsymbol{S}\boldsymbol{c} \,, \tag{3.49}$$

with the coefficients c_a and c_b and the overlap, defined as

$$S = \left\langle\psi_N^{\mathrm{D}}\middle|\psi_N^{\mathrm{A}}\right\rangle = \left\langle\psi_N^{\mathrm{A}}\middle|\psi_N^{\mathrm{D}}\right\rangle . \tag{3.50}$$

Diagonalizing the spin-orbitals is accomplished using a transformation matrix $\boldsymbol{X}$ that satisfies $\boldsymbol{X}^\dagger\boldsymbol{S}\boldsymbol{X} = \mathbf{1}$ and $\boldsymbol{c} = \boldsymbol{X}\boldsymbol{c}'$.
Such a matrix brings the matrix equation (3.49) into

$$\boldsymbol{H}\boldsymbol{X}\boldsymbol{c}' = E\boldsymbol{S}\boldsymbol{X}\boldsymbol{c}' \,, \tag{3.51}$$

which when multiplying with $\boldsymbol{X}^\dagger$ from left reads:

$$\boldsymbol{H}'\boldsymbol{c}' = E\boldsymbol{c}' \,, \tag{3.52}$$

with $\boldsymbol{H}' = \boldsymbol{X}^\dagger \boldsymbol{H} \boldsymbol{X}$.
This diagonalization of the spin-orbitals can be achieved through the Löwdin-orthogonalization procedure [80], where $\boldsymbol{X}$ is chosen as $\boldsymbol{S}^{-1/2}$. To compute the square root of the overlap matrix, one takes the square root of its diagonal form $\boldsymbol{s}$, which is related to the form used in Eq. (3.49) by a unitary matrix:

$$\boldsymbol{X} = \boldsymbol{S}^{-1/2} = \boldsymbol{U} \boldsymbol{s}^{-1/2} \boldsymbol{U}^\dagger \,. \tag{3.53}$$

The unitary transformation matrix reads

$$\boldsymbol{U} = \frac{1}{\sqrt{2}} \begin{pmatrix} 1 & 1 \\ 1 & -1 \end{pmatrix} . \tag{3.54}$$

Applying all these transformations, the actual coupling in orthogonal basis can be found by

$$H'_{ab} = J_{ab} = \frac{H_{ij} - \frac{1}{2}(H_{ii} + H_{jj})S}{1 - S^2} \,. \tag{3.55}$$

As previously mentioned, one of the reasons for the efficiency of DFTB stems from the utilization of a minimal basis set. While this approach enhances computational speed, it also poses challenges in accurately describing the interaction between two atoms across a wide range of distances, as it relies on an approximative basis function derived from solving the confined single atomic problem (3.42). Unfortunately, the tail of the basis function becomes suppressed, resulting in a poor representation of the atomic orbital at distances beyond the bond length. However, this portion of the atomic orbital is crucial for calculating electronic coupling, which consequently leads to a severe underestimation when standard DFTB parameters are used for coupling calculations.

By reducing confinement during the parametrization process, an improved description of the atomic basis at larger distances is achieved. This approach allows for mimicking the features of a basis with longer-reaching tails with the computational efficiency of a minimal basis. In benchmark studies by Kubas et al. [81, 82], such a procedure was employed to properly capture the tails of the basis set. It was found that the couplings, when compared to high-level calculations, exhibited only a systematic error, which could be corrected by scaling the obtained couplings with a constant factor [83, 84, 79].

3.2 Modelling amorphous organic structures

In a multiscale simulation of organic semiconductors, the first step is to model thin amorphous organic films. Unlike crystalline semiconductors, whether they are organic or inorganic, describing amorphous structures mathematically is quite challenging. This complexity highlights the necessity of using computational methods to effectively simulate these structures.
Simulation techniques in this context involve integrating the geometric and physical characteristics of individual molecules, allowing for the simulation of amorphous structures composed of thousands of

molecules. Accurately representing intra- and intermolecular forces is crucial for capturing properties such as packing density, as well as potential isotropy or anisotropy.
There are two main approaches to model amorphous organic structures: MD [85, 86, 87, 88] and Monte-Carlo (MC) [89, 9]. MC methods encompass a class of computational approaches that utilize random numbers to compute physical observables, solve differential equations, integrate functions, or model various processes. In the context of generating amorphous structures, MC methods involve randomly generating structures through defined "moves," with subsequent acceptance or rejection of the new state determined by the Metropolis criterion. In comparison, MD methods involve solving Newton's equations using force-fields to model molecular motion within classical mechanics.
In the work discussed in Chapter 4, a combination of both approaches was used: the structures were generated with the MC-based simulation tool DEPOSIT [9], followed by subsequent MD simulations to study the structural dynamics of the amorphous materials.

3.2.1 DEPOSIT: Monte-Carlo protocol for structure generation

In the DEPOSIT protocol, the process of simulating PVD involves adding single molecules to a simulation box one by one. For each molecule, several simulated annealing cycles are conducted to determine its lowest energy conformation inside the simulation box. This process continues until the desired number of molecules is deposited. The deposition protocol starts with initializing a simulation box with the dimensions L_x, L_y and L_z. Then single molecules are added one by one until the desired number of molecules is reached.

Energy contributions

The energy of a molecule in the deposition process consists of contributions from both intermolecular and intramolecular interactions. In DEPOSIT the bond lengths and bond angles of the molecules remain constant during the entire deposition process. Consequently, geometry optimizations of the molecules are typically conducted beforehand using DFT. This leads to the following expression:

$$E_{\text{total}} = U_{\text{LJ}} + U_{\text{C}} + U_{\text{DH}} \,. \tag{3.56}$$

The first two terms are so-called non-bonded terms representing interatomic interactions, which in this case is the Lennard-Jones interaction

$$U_{\text{LJ}} = \frac{1}{2} \sum_{i,j} 4\epsilon_{ij} \left(\left(\frac{\sigma_{ij}}{r_{ij}} \right)^{12} - \left(\frac{\sigma_{ij}}{r_{ij}} \right)^{6} \right) \tag{3.57}$$

and the Coulomb interaction

$$U_{\text{C}} = \frac{1}{2} \sum_{i,j} \frac{q_i q_j}{r_{ij}} \,. \tag{3.58}$$

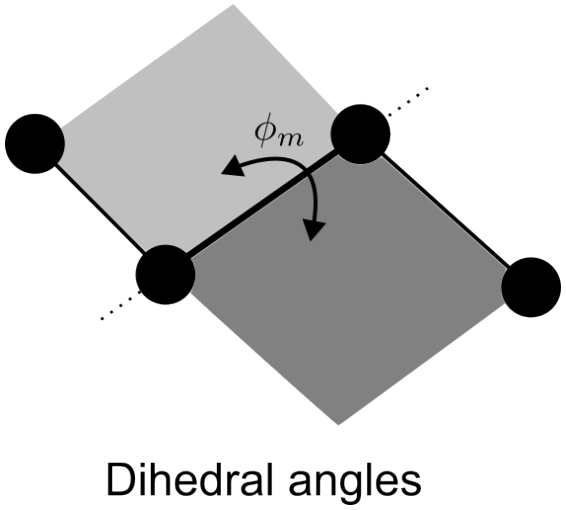

Figure 3.2: Definition of the dihedral angle. The dihedral angle between two planes defined by sets of three points each is used to characterize torsion angles in molecular structures.

The Lennard-Jones parameters ϵ_{ij} and σ_{ij}, along with atomic charges q_i, can be obtained from published literature [90, 91] or methods involving fitting to ab-initio calculations. The non-bonded energy contributions depend on the interatomic distance r_{ij}. The intra-molecular energy coming from torsional deformations of the molecule (see Figure 3.2) is given by:

$$U_{\mathrm{DH}} = \sum_m V_m \left[1 + \cos(n_m \phi_m - \gamma_m)\right] . \tag{3.59}$$

The parameters for the torsion terms, are the energy amplitude V_m, the periodicity n_m and a phase angle γ_m. The parameters for the torsional energy can also be either used from existing databases or by fitting to energies obtained from quantum-chemical calculations.

Simulated annealing

After setting up the simulation box and all necessary energy parameters, a molecule is placed randomly inside the simulation box, and the initial total energy E_0 is computed according to equation (3.56). Next, a random molecular move is executed, which can involve either a random translation of the entire molecule, a random 3D rotation of the molecule around its center of geometry, or a random but physically permissible adjustment of the dihedral angles ϕ_m. This results in a new state with energy E_1. The new state is accepted or rejected according to the Metroplis criterion [92]:

$$P = \begin{cases} \exp\left(-\frac{E_1 - E_0}{k_{\mathrm{B}} T_n}\right), & \text{if } E_1 - E_0 < 0, \\ 1, & \text{otherwise} , \end{cases} \tag{3.60}$$

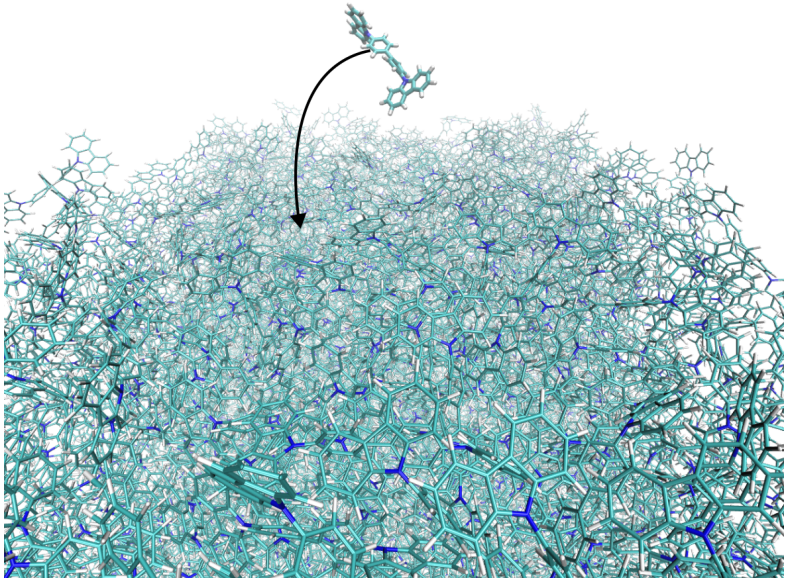

Figure 3.3: Deposition process. A molecule is deposited on top of already deposited molecules according to the described DEPOSIT protocol.

where P denotes the probability for acceptance. If the proposed state is rejected, the molecular conformation is reset to its previous state. If the proposed state is accepted, the next random move is performed based on the new conformation.
Such moves are repeated n times while the temperature is reduced for each step according to

$$T_n = T_\mathrm{s}\left(\frac{T_\mathrm{e}}{T_\mathrm{s}}\right)^{1/n}, \tag{3.61}$$

where the start- and end temperature are denoted with T_s or T_e respectively. This iterative process is known as simulated annealing (SA), designed to globally minimize the molecule's energy while avoiding being trapped in local energy minima [93]. Several simulated annealing cycles can be run in parallel, ultimately choosing the conformation with the lowest energy to serve as the final deposited molecule.

SA cycles are performed for each molecule that is deposited, progressively constructing the entire structure molecule by molecule. Following the deposition of each molecule, the non-bonded interactions U_LJ and U_C need to be updated based on the addition of the new molecule. As more molecules are deposited, additional interaction terms are incorporated into the energy evaluation during the SA process. The previously deposited molecules are treated as static. The deposition process is illustrated in Figure 3.3.

3.2.2 Molecular dynamics

In the work presented in Chapter 4 after the deposition process, the structural dynamics of the generated morphologies is simulated using MD which is briefly discussed here. The fundamental concept behind Molecular Dynamics (MD) is to approximate all quantum mechanical interactions through an analytic expression for the energy $U(\{\boldsymbol{r}\})$, where $\{\boldsymbol{r}\}$ represents the positions of all atoms. This energy function comprises multiple terms, each of which needs to be parameterized based on higher-level quantum chemistry methods [94]. By deriving the forces acting on each atom from this energy function, we can solve the equations of motion based on Newtons laws:

$$\boldsymbol{F}_i = m_i \boldsymbol{a}_i \ , \tag{3.62}$$

where m_i is the mass of atom i. The forces are computed with

$$\boldsymbol{F}_i = -\nabla_i U(\{r\}) \ . \tag{3.63}$$

Force field parameters

Again, the expression for the energy can be decomposed into bonded and non-bonded terms

$$U(\{\boldsymbol{r}\}) = U_{\text{bonded}} + U_{\text{LJ}} + U_{\text{C}} \ , \tag{3.64}$$

where the Lennard-Jones and Coulomb potential were introduced in equations (3.57) and (3.58). In the MD simulation, bond angle- and bond-length vibrations are explicitely considered. Together with the torsion-terms (3.59), the energy of the bonded contributions reads:

$$\begin{aligned} U_{\text{bonded}} =& \frac{1}{2} \sum_j k_j (d_j - d_j^0)^2 \\ &+ \frac{1}{2} \sum_k f_k (\theta_k - \theta_k^0)^2 \\ &+ \sum_m V_m \left[1 + \cos(n_m \phi_m - \gamma_m)\right] \ , \end{aligned} \tag{3.65}$$

where the sums run over all bonds, bond angles and dihedral angles. The parameters k_j and f_k represent the force constants of the bond-length and bond-angle oscillations respectively. The parameters for the torsion terms have been discussed earlier. The specific functional forms of the bonded terms are somewhat arbitrary and can be adjusted to more complex expressions as needed. When referring to a "force field," it generally encompasses the choice of functional forms and the specific parameterization used for a specific applications.
For the work in Chapter 4, the force field employed was the general Amber force field (GAFF) [91, 90].

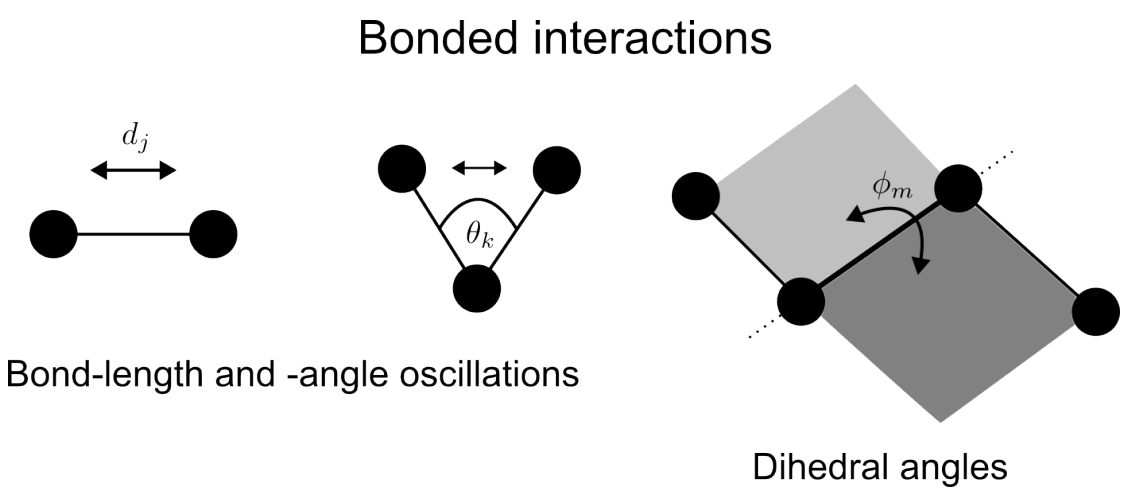

Figure 3.4: Schemes Illustrating terms in the bonded energy terms.

MD trajectory

As previously mentioned, the objective is to solve Newton's equation (3.62) to determine the atomic trajectories $\boldsymbol{r}_i(t)$. In practice, this is achieved through numerical integration, commonly utilizing the Verlet algorithm [95], where the time evolution of particle positions, velocities, accelerations, and the related forces is described by:

$$\boldsymbol{r}_i(t+\mathrm{d}t) = \boldsymbol{r}_i(t) + \boldsymbol{v}_i(t)\,\mathrm{d}t + \frac{1}{2}\boldsymbol{a}_i(t)\,\mathrm{d}t^2 \tag{3.66}$$

$$\boldsymbol{v}_i(t+\mathrm{d}t) = \boldsymbol{v}_i(t) + \boldsymbol{a}_i(t)\,\mathrm{d}t \tag{3.67}$$

$$\boldsymbol{a}_i(t+\mathrm{d}t) = \frac{1}{m_i}\boldsymbol{F}_i(t)\,. \tag{3.68}$$

The timestep $\mathrm{d}t$ in the Chapter 4 was 2 ps.
In an MD simulation, the process begins by assigning each atom its initial position and a velocity typically drawn from a Boltzmann distribution. The energy $U(r)$ is then computed based on the current atom positions. From this energy evaluation, atomic accelerations are determined, followed by the calculation of velocities for the next time step and subsequently updated atomic positions. This iterative cycle continues until certain stopping criteria are met.
There are additional aspects of MD simulations to consider, such as alternative integration schemes and the use of boundary conditions like thermostats or barostats [96, 97], but discussing these topics is beyond the scope of this thesis.

3.3 Theory of charge & exciton transport in molecular systems

In this section, I will discuss the transport mechanism of charges and excitons in amorphous organic materials, which is fundamentally different from band transport in crystalline solids [98]. This discussion will provide the basis for understanding the computational model applied throughout this thesis.

3.3.1 Charge transport in amorphous organic solids

A central physical property of materials in nano-electronics or electronics in general is the conductivity tensor with elements σ_{ij}:

$$\sigma_{ij} = e\rho\mu_{ij}, \tag{3.69}$$

where e represents the elementary charge, ρ is the density of mobile carriers, and μ_{ij} denotes elements of the carrier mobility tensor.
This definition is general and applies without regard to the specific type of material or nature of charge transfer. Detailed characteristics related to specific materials such as structure or external factors like temperature or doping dependency are governed by the parameters ρ and μ_{ij}.

Carrier density

The density of mobile carriers can be decomposed into two contributions: the intrinsic part and an extrinsic part $\rho = \rho_{\text{int}} + \rho_{\text{ext}}$. The intrinsic contribution for holes and electrons are closely related to the density of states $\text{DOS}(\varepsilon)$ of the material of interest:

$$\rho^{\text{e}}_{\text{int}} = \int_{\epsilon_{\text{F}}}^{\infty} \text{DOS}(\varepsilon) f(\varepsilon, T) \tag{3.70}$$

$$\rho^{\text{h}}_{\text{int}} = \int_{-\infty}^{\epsilon_{\text{F}}} \text{DOS}(\varepsilon)\Big(1 - f(\varepsilon, T)\Big), \tag{3.71}$$

with the Fermi level ε_{F} Fermi-Dirac distribution:

$$f(\varepsilon, T) = \frac{1}{\exp\left(\frac{\varepsilon - \varepsilon_{\text{F}}}{k_{\text{B}}T}\right) + 1}. \tag{3.72}$$

The extrinsic contribution is highly dependent of material defects like introduction of dopants or field-induced energy-shifts with respect to the Fermi level.
Or amorphous organic semiconductors, for long time the mechanism of doping was not well understood. Fediai et al. published a work where doping in molecular systems was studied on the scale of large amorphous structures [16, 99, 15].

Carrier mobility

Carrier mobility is defined using the time-averaged carrier velocity $\langle v \rangle_i$, often referred to as drift velocity, in response to an external electric field $\boldsymbol{F}$:

$$\mu_{ij} = \frac{\langle v \rangle_i}{F_j}. \tag{3.73}$$

For our interest in isotropic amorphous structures under a homogeneous electric field, the tensorial equation (3.73) simplifies to a scalar equation for carrier mobility $\mu = \langle v \rangle / F$.
Modeling the drift velocity heavily depends on the transport mechanism, which is inherently tied to the material properties. In solid-state physics, the well-established band-transport theory describes carrier transport in crystalline systems. A key feature of this theory is the significant carrier delocalization; for example, the electron gas model [100].
In disordered systems, especially in amorphous organic materials, charge carriers tend to be highly localized on individual molecules or functional groups. This localization is primarily attributed to two factors: structural disorder within the material and weak coupling between neighboring molecules [101]. Given this carrier localization, transport in such systems is typically described by the charge hopping model [102].
In the hopping model, the transportation of either holes or electrons is depicted by consecutive jumps from one molecule i to another j. For each hop between a pair of molecules, there is an associated charge transfer (CT) rate $\omega_{ij}^{\mathrm{CT}}$.

CT-rate equation

Typically, rates of charge transfer (CT) are often described using Marcus theory [103]. I will briefly discuss some fundamental concepts behind Marcus theory. This theory operates within the high-temperature limit ($k_{\mathrm{B}}T \gg \hbar\omega_\nu$), where ω_ν represents the frequency of vibrational mode ν. This temperature limit makes a classical treatment of the molecular vibronics possible. For simplicity, I consider a single vibrational mode characterized by frequency ω and equilibrium coordinate $q^{(0)}$. The molecules PES can then be expressed as

$$U(q) = U^{(0)} + \frac{1}{2}\omega\left(q - q^{(0)}\right)^2 . \tag{3.74}$$

Applying Fermis Golden Rule to the case of manifold initial states, as present here, and considering the classical treatment of vibrational motions, the resulting rate formula reads:

$$\omega_{ij}^{\mathrm{CT}} = \frac{2\pi}{\hbar}\int \mathrm{d}q\; f(q)\,|J_{ij}|^2\,\delta(U_i(q) - U_j(q))\,, \tag{3.75}$$

where

$$f(q) = \frac{1}{Z} \exp\left(\frac{-U_i(q)}{k_B T}\right) \tag{3.76}$$

is the probability that the donor-molecule i occupies molecular state q. The electronic coupling J_{ij} can be obtained by equation (3.55).
Integrating over q and collecting all terms, leads to the final form of the Marcus rate:

$$\omega_{ij}^{(\mathrm{CT})} = \frac{2\pi}{\hbar} \frac{1}{\sqrt{4\pi\lambda k_\mathrm{B} T}} |J_{ij}|^2 \exp\left(-\frac{(\Delta\varepsilon_{ij} + \lambda)^2}{4\lambda k_\mathrm{B} T}\right). \tag{3.77}$$

In practice, the energy difference $\Delta\varepsilon_{ij} = U_j^{(0)} - U_i^{(0)}$ is taken as the difference between the HOMO energy for hole transport and the LUMO energy for electron transport [104]. The parameter λ, known as the reorganization energy, is defined as

$$\lambda = \frac{\omega^2}{2}(q_j^{(0)} - q_i^{(0)})^2 \,, \tag{3.78}$$

where ω is a characteristic frequency, and $q_j^{(0)}$ and $q_i^{(0)}$ are equilibrium positions of the molecular vibrations associated with states j and i, respectively. The reorganization energy λ is often computed using the Nelsen four-point procedure [105, 106].

Gaussian Disorder Model

In 1993, Heinz Bässler, suggested that the energies of the hole- and electron transporting states (HOMO and LUMO) form a Gaussian density of states [6]:

$$\mathrm{DOS}(\varepsilon) = \frac{1}{\sqrt{2\pi\sigma^2}} \exp\left(-\frac{(\varepsilon - \langle\varepsilon\rangle)}{2\sigma^2}\right), \tag{3.79}$$

where the parameter σ is the energetic disorder in absence of any spatial correlations. After performing KMC calculations, Bässler fitted an analytic expression to the obtained carrier mobility and found out that the mobility strongly depends on the energetic disorder [6]

$$\mu(T) = \mu_0 \exp\left(-\frac{4}{9}\left(\frac{\sigma}{k_\mathrm{B} T}\right)^2\right). \tag{3.80}$$

The field dependency was first observed in experimental time-of-flight measurements and found to be of Poor-Frenkel type [107]:

$$\mu(F) = \mu(T) \cdot \exp\left(\gamma(T)\sqrt{F}\right), \tag{3.81}$$

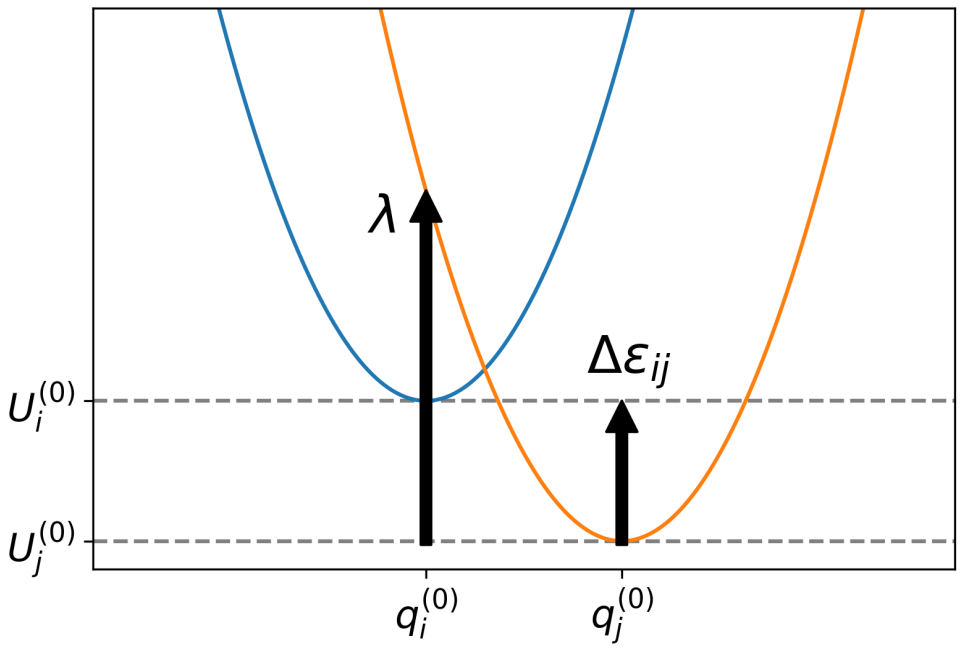

Figure 3.5: Visualization of the reorganization energy and the energy-difference in Marcus theory.

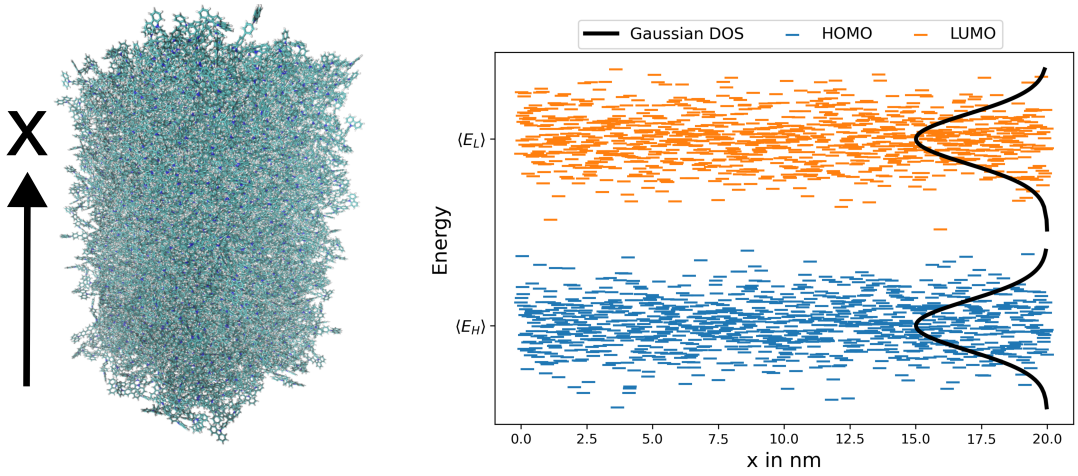

Figure 3.6: Gaussian disorder model. The Highest Occupied Molecular Orbital (HOMO) and Lowest Unoccupied Molecular Orbital (LUMO) levels were calculated along the transport x axis in an amorphous structure composed of CBP molecules. This structure was generated using the DEPOSIT protocol [9].

where F is the electric field strength, and $\gamma(T)$ is an empirical temperature-dependent factor:

$$\mu(F,T) = \mu(T) \cdot \exp\left(\gamma(T)\sqrt{F}\right), \tag{3.82}$$

with an empirical temperature dependent factor $\gamma(T)$.

3.3.2 Exciton transport

The description of exciton dynamics, akin to charge dynamics, depends on the specific properties of the material being studied. In inorganic semiconductors, which typically exhibit high levels of order, excitons can span multiple unit cells, forming what are referred to as Mott excitons [108]. Conversely, in disordered organic semiconductors, excitons remain localized on individual molecules [109], forming so-called Frenkel-excitons.

This distinction provides the rationale for treating exciton diffusion in a manner similar to charge carrier transport, involving discrete hops from one molecule to another. There are two recognized types of exciton transfers: one involves simultaneous charge transfer from a donor molecule i to an acceptor molecule j, referred to as Dexter transfer [110], and the other involves de-excitation of the donor molecule followed by energy transfer to the acceptor molecule, leading to its excitation; this is termed Förster transfer [111]. Figure 3.7 illustrates the Förster and Dexter transfer processes of a singlet exciton.

In this study, Dexter transfer is modeled using Marcus theory (3.77) in a similar manner to charge transfer, but with the relevant excitation energies substituted for the charge transfer energies. Dexter transport necessitates an overlap between the LUMOs and HOMOs of the donor and acceptor molecules, making it a very short-ranged transport mechanism, akin to charge transfer.

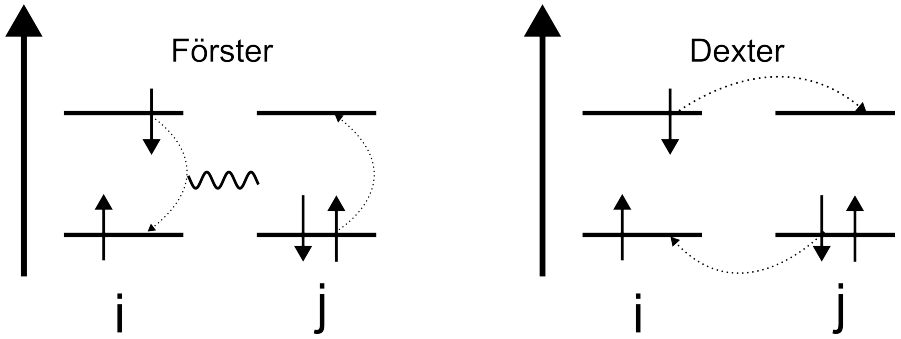

Figure 3.7: Förster and Dexter exciton-transport. Förster transfer involves the de-excitation of the exciton donor molecule i, with energy transfer to molecule j, resulting in the excitation of molecule j. The energy transfer is indicated by a wiggly line. On the other hand, Dexter transfer, the second transfer mechanism, involves the simultaneous transfer of both the electron in the excited state and the remaining hole.

Förster transfer can also be described using Marcus theory, where the corresponding excitation energies and excitonic reorganization energy are used in the exponent. However, the coupling can be effectively approximated by:

$$J_{i,j}^{\text{Förster}} = \kappa \frac{|\boldsymbol{d}_i||\boldsymbol{d}_j|}{r_{ij}^3}, \tag{3.83}$$

where $\boldsymbol{d}_i$ represents the transition dipole moment and κ describes the relative orientation of the transition dipole moments of the donor and acceptor molecules. The transition dipole moment, for instance, in the case of a molecule in the first excited singlet state where the electron is excited from the HOMO to the LUMO, can be expressed as:

$$\boldsymbol{d} = \int d\boldsymbol{r}\ \psi_{\text{HOMO}}^*(\boldsymbol{r})\boldsymbol{r}\psi_{\text{LUMO}}(\boldsymbol{r}). \tag{3.84}$$

Unlike Dexter transfer, Förster transfer does not require an overlap between the molecular orbitals of the donor and acceptor molecules. The coupling is mediated by the interaction of the transition dipole moments, which can extend over several nanometers.
Further details on Förster transfer and its application within this work can be found in Chapter 5 and in the study by Stehr et al. [112].

3.4 Device simulations

The preceding sections provided an introduction to the theoretical foundations used in computational models for simulating charge and exciton transfer in disordered systems, and even for performing comprehensive device simulations. A typical example for a device could be the one presented in Figure 2.4. Now, I will introduce several prominent computational approaches, briefly comparing their strengths and weaknesses, before delving into a more detailed description of the general Kinetic Monte Carlo (KMC) algorithm.

3.4.1 Overview of simulation methods

The theoretical concepts discussed above are all for one particular purpose, generating structures computing the electronic and excitonic properties, but the actual simulation of nano-electronic devices requires dedicated simulation methods. Before I introduce the KMC that was exclusively used in this work, I want to give a short and brief description of two other methods, namely the drift-diffusion model (DDM) and Master equation (ME) approach.

Drift-Diffusion model

DDM approaches are widely used and popular for device modeling in inorganic semiconductors. They excel in simulating complex device geometries [113, 114] and can effectively describe charge transfer in devices spanning several micrometers [104].
These approaches operate under a macroscopic framework, treating charge flow as a continuum. The fundamental equations include the continuity equation, which ensures charge conservation, and an equation incorporating driving forces on the current density.
For electrons, the continuity equation is expressed as [115]:

$$\frac{\partial n(\boldsymbol{r},t)}{\partial t} = \frac{1}{q}\nabla \boldsymbol{j}_n(\boldsymbol{r},t) + G(\boldsymbol{r},t) - R(\boldsymbol{r},t), \tag{3.85}$$

where the change in electron density at position $\boldsymbol{r}$ is governed by the charge flux (first term), as well as electron generation $G(\boldsymbol{r},t)$ due to processes like exciton separation, or annihilation $R(\boldsymbol{r},t)$ due to processes like recombination. The specifics of these terms can vary between implementations, but the underlying concept remains consistent.
The second equation describes carrier transport physics influenced by external fields (drift) and concentration gradients within the device (diffusion):

$$\boldsymbol{j}_n(\boldsymbol{r}) = qn(\boldsymbol{r})\mu_n \boldsymbol{F} + qD_n \nabla n(\boldsymbol{r}), \tag{3.86}$$

where electron mobility μ_n and electron diffusion coefficient D_n are typically included as material-specific parameters.

DDM is suitable for describing devices in steady-state conditions:

$$\frac{\partial n(\boldsymbol{r},t)}{\partial t} = 0, \tag{3.87}$$

particularly when the steady-state does not significantly deviate from thermal equilibrium [104]. However, DDM may not adequately handle disorder that cannot be effectively captured by material constants and requires explicit treatment.
In summary, DDM is limited in addressing nanostructured devices [116] and scenarios where disorder plays a critical role beyond what can be represented by effective material parameters.

Master-equation

Another approach to simulate complete devices in three dimensions involves solving the Master Equation. This method facilitates a comprehensive 3D simulation of a device. Before starting the device-simulation, a hopping matrix is initialized, representing a discretized spatial grid where each lattice site corresponds to a molecule. Specifically focusing on cubic lattices, each point is assigned an energy value drawn from a Gaussian distribution where the distribution width represents the energetic disorder. Once the grid is set up, charge transport within the lattice can be described using the ME.
For example, considering holes: [117, 118, 119]):

$$\frac{\mathrm{d}p_i}{\mathrm{d}t} = \sum_{j\neq i}\Big(p_j\omega_{ji}^{\mathrm{CT}}(1-p_i) - p_i\omega_{ij}^{\mathrm{CT}}(1-p_j)\Big) - R_i + G_i\ . \tag{3.88}$$

In this approach, the occupation probability p_i represents the likelihood of site i being occupied, while $\omega_{ji}^{\mathrm{CT}}$ denotes the hole transfer rate from site j to i, often calculated using the Marcus equation (3.77). The terms R_i and G_i correspond to the annihilation and generation rates of holes, respectively. Similar equations are necessary for modeling other types of particles. Charge hopping leads to a continuous change in the occupation probability p_i, which ranges continuously between 0 and 1. When the system reaches a steady state ($\mathrm{d}p_i/\mathrm{d}t = 0$), a set of coupled equations must be solved self-consistently.
A significant drawback of the ME approach is the treatment of Coulomb interactions among charge carriers within the device. Because occupation probabilities are continuous, a mean-field approximation of Coulomb interaction is commonly used. However, this approximation can sometimes underestimate the forces acting on charge carriers, leading to potential inaccuracies in process rates.
Figure 3.8 depicts a 2D quadratic hopping matrix. The various colors indicate HOMO energies sampled from a Gaussian distribution. The semi-transparent red dots symbolize partial hole occupation (with values ranging between 0 and 1).

3.4.2 Kinetic Monte Carlo

Kinetic Monte Carlo methods simulate the dynamics of physical systems by implementing predefined transition rules and utilizing random numbers to evolve the system from one state to another, while

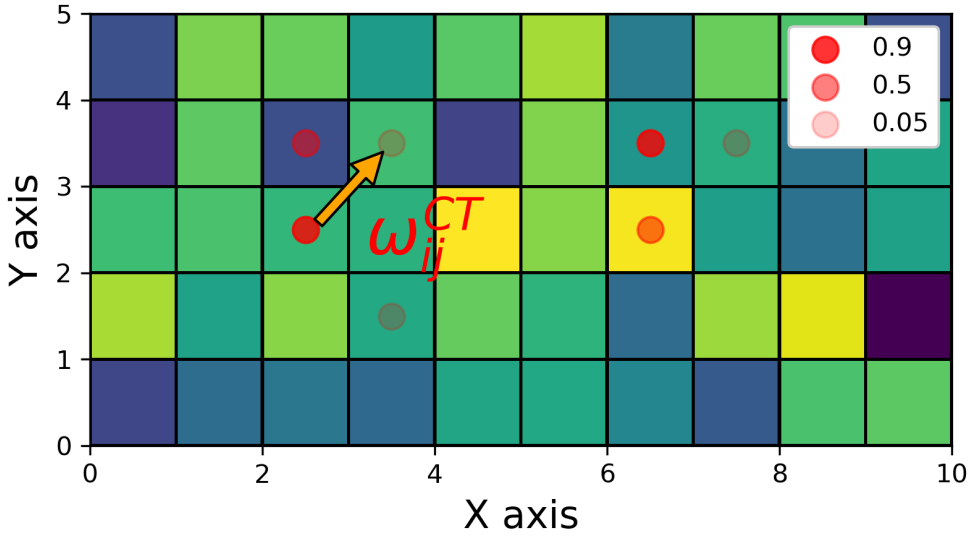

Figure 3.8: Discrete hopping matrix for ME approach. The red circles indicate partial hole occupation of the sites. The square colors represent the energetic disorder.

also assigning a physical time increment to each progression step.
In OLED modeling, a primary distinction between the KMC method and the Master Equation method lies in the occupation probability, which is strictly binary (either 0 or 1) in KMC. This discrete representation mirrors charge transfer as distinct events, aligning well with the hopping transport model used for disordered OSC systems. This approach allows for an exact treatment of Coulomb interactions among charge carriers in the device, but typically requires significantly more computational resources compared to ME simulations [104, 119].
The KMC algorithm operates on a Markov chain principle, where the past evolution history of the system is irrelevant for determining the next state. This implies that only the current state is necessary to predict and obtain the subsequent system state. Is is done by generating a list of all possible system transitions, which could be something like the transfer of a charge carrier from site to site, the injection of a charge carrier, electron-hole recombination and many more. In principle, every process that can be described as a distinct event and has an associated rate can be implemented into the list of possible processes in the KMC simulation framework. This includes a wide range of physical phenomena such as charge carrier transfer between sites, charge injection, electron-hole recombination, and many others.

To illustrate the Kinetic Monte Carlo (KMC) algorithm, I will use the example introduced in Figure 3.9, where sites are either occupied or unoccupied. I assume the device is initially in a state with 2 holes, which I will denote as state I.
Each hole has 8 potential target sites, and each transition from an occupied site to an unoccupied site is characterized by a unique rate $\omega_{ij}^{\mathrm{CT}}$. These transition rates are collected into a list $\Lambda_{I\to II}$:

$$\Lambda_{I\to II} = \Big(\underbrace{\ldots, \quad \omega_{ij}^{\mathrm{CT}}, \quad \ldots}_{16 \text{ rates}}\Big). \tag{3.89}$$

The cumulative rate is defined as the sum of the rates of all potential processes from (3.89):

$$\Omega = \sum_{n=1}^{16} \omega_n^{\mathrm{CT}}\,. \tag{3.90}$$

To decide which process is executed next, a random number ω_x is generated from a uniform distribution between 0 and Ω. This random number ω_x is then used to determine the specific transition k that needs to be executed next, based on the following condition:

$$\sum_{n=1}^{k-1} \omega_n^{\mathrm{CT}} < \omega_x \leq \sum_{n=1}^{k} \omega_n^{\mathrm{CT}}\,. \tag{3.91}$$

After each execution step, the system transitions to a new state with updated particle positions, which in turn alters the Coulomb interactions within the system. To proceed with the simulation, the rates for possible transitions must be recomputed based on the new state. This iterative process continues until

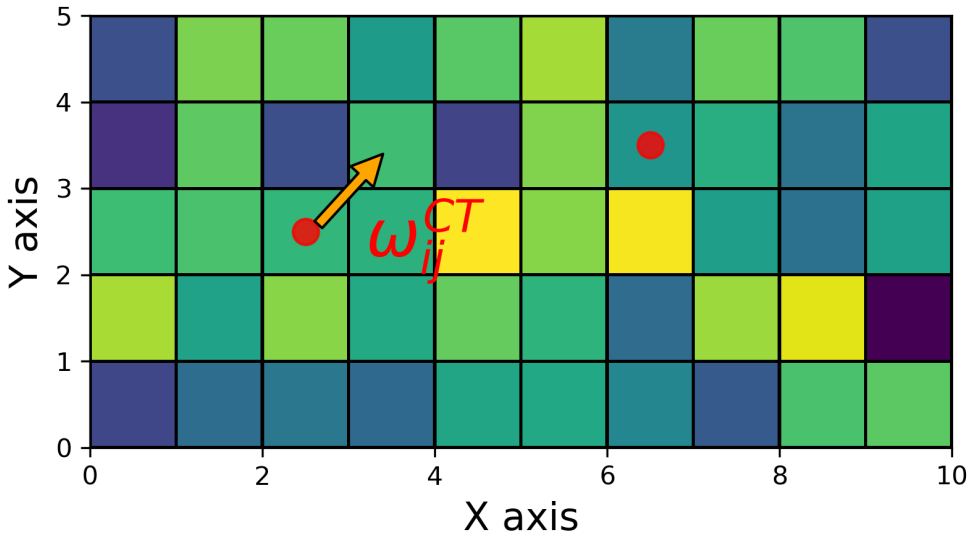

Figure 3.9: Discrete hopping matrix for KMC. In contrast to the ME-approach, the sites are either occupied or not. Charge transfer is treated as perfectly distinct processes. The square colors represent the energetic disorder.

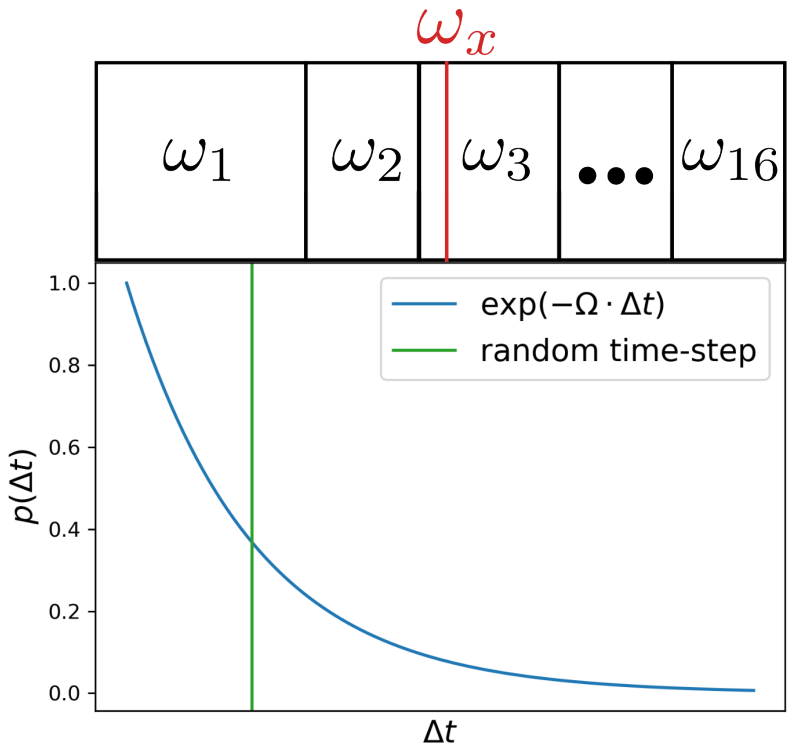

Figure 3.10: System transition and corresponding time increment. In this illustration, the system transition that corresponds to rate ω_3 is executed. The corresponding time increment Δt is drawn for them exponential distribution which is parameterized by the cumulative rate Ω.

a specified termination criterion is met.
The time elapsed during each transition is determined by the cumulative rate Ω. The probability of the system remaining in state I can be modeled using an exponentially decaying function of the time difference Δt, given by [120]:

$$p(\Delta t) = \exp(-\Delta t \cdot \Omega)\,. \tag{3.92}$$

The time-step is then obtained by drawing another random number based on the distribution (3.92). Figure

Carrier mobility calculation

Starting from a hopping matrix containing a specified number of hopping sites, each assigned a site energy ε_i and interconnected with inter-site couplings to compute CT rates between all sites (3.77), we can then use KMC to calculate the mobility of charge carriers. In this discussion, I will outline the protocol for calculating carrier mobility.

As earlier mentioned, one key advantage of KMC simulations is the explicit consideration of Coulomb interactions between charge carriers. Consequently, after each KMC step where a carrier changes its position, the Coulomb interactions with all charge carriers must be updated. For instance, considering a hole located at site i and a potential target site j for hole transfer, the energy difference, accounting for interactions with all other holes in a hole-only system, is expressed as follows (in atomic units):

$$\Delta\varepsilon_{ij} = \left[\varepsilon_j + \frac{1}{\epsilon_r}\sum_{l\neq j}\frac{1}{R_{lj}}\right] - \left[\varepsilon_i + \frac{1}{\epsilon_r}\sum_{l\neq i}\frac{1}{R_{li}}\right] + FR_{ij}\,. \tag{3.93}$$

Here, F represents the electric field applied in the transport direction, and R_{ij} denotes the projection onto the field direction of the distance vector between site i and j. The summation extends over all interactions involving the hole of interest with the other holes.
To achieve a steady state, a total of 10^7 Kinetic Monte Carlo (KMC) steps are conducted across 20 independent realizations of the hopping matrix to improve the statistics. In each realization n, the hole mobility $\mu^{(n)}$ is calculated as $\mu^{(n)} = v^{(n)}\text{drift}/F$, where $v^{(n)}\text{drift}$ represents the cumulative drift velocity in the transport direction x. The cumulative drift-velocity is obtained with:

$$v_{\text{drift}} = \frac{\sum_i \Delta x_i}{t_{\text{total}} - t_0}\,, \tag{3.94}$$

where t_{total} is the total system-time after 10^7 KMC-steps and $t_0 = t_{\text{total}}/3$. The sum in the numerator of eq. (3.94) runs over all hole-displacements that occurred during the final third of the KMC-simulation to ensure a steady-state of the overall charge transport. The final mobility is than obtained by:

$$\mu = \frac{1}{20}\sum_n \mu^{(n)}\,, \tag{3.95}$$

with the standard deviation of

$$\text{Var}[\mu]^{1/2} = \sqrt{\frac{1}{19}\sum_n (\mu - \mu^{(n)})^2}\,, \tag{3.96}$$

4

Dynamic effects in hole transport through amorphous semiconductors

The work presented here was published in:
Ali Deniz Özdemir, Samaneh Inanlou, Franz Symalla, Weiwei Xie, Wolfgang Wenzel, Marcus Elstner. Dynamic Effects on Hole Transport in Amorphous Organic Semiconductors: a Combined QM/MM and kMC Study. J. Chem. Theory Comput. 2023, 19, 13, 3849–3860 [121]

The mobility of charge carriers in amorphous organic semiconductors is a pivotal and limiting factor influencing the performance and utility of emerging electronic devices. Computational models have been developed to calculate mobility, accounting for structural disorder in morphologies consisting of several thousand molecules, and these models have been successfully employed in the past[122, 123, 124, 125, 126]. Nevertheless, a significant drawback of many of these models is the absence of a differentiated treatment regarding the influence of dynamical fluctuations on the energetic and intermolecular properties of the structures under investigation. Acknowledging the existence of both static and dynamic contributions to the overall structural disorder, there is an advantage in explicitly examining static and dynamic disorders separately. This approach aims to comprehend the individual impact of each disorder type on mobility and explore potential avenues for their reduction.
In 2015, Tummala et al. first distuingished between static and dynamic contributions to the overal disorder in OSC. Since then dynamic effects on the energetics and the resulting dynamic disorder have been

studied in crystalline or partially ordered systems [127, 128, 129, 130, 131, 132, 133, 134]. Notably, Aydin and Yavuz [135] investigated dynamic effects on energetic disorder and their implications for charge carrier mobility in fully amorphous systems. However, it's important to highlight that their study did not encompass dynamic effects on intermolecular couplings.

Beratan and Skourtis have conducted thorough examinations of the impact of structural fluctuations on electronic couplings in biomolecular systems [136, 137, 138, 139]. Their proposal suggests that the degree to which molecular fluctuations influence coupling strength dictates the approach for time-averaging the couplings. This time-averaging is crucial for deriving an effective coupling, which is subsequently used in the Marcus rate expression. Nevertheless, a comprehensive investigation of this nature has not been carried out in amorphous systems consisting of small organic molecules. Gali et al. [140] investigated the dynamics of energetics and couplings in OSC and their influence on charge carrier mobility. However, their approach differs from ours in two main aspects: firstly, they focused specifically on OSC based on polymers, and secondly, they computed the couplings using a singleMD snapshot rather than multiple snapshots. For each snapshot, they incorporated a random correction term to the intermolecular couplings drawn from a Gaussian distribution. This method introduces a snapshot dependency of the couplings, although it does not inherently account for potential correlations between coupling fluctuations and fluctuations in site energy. The explicit treatment of electronic couplings requires a thorough time-dependent calculation across many molecular pairs, requiring highly efficient quantum chemical methods.

The primary focus of this study is to evaluate the influence of both static and dynamic structural disorder on transport energies and electronic couplings, employing quantum chemical calculations. The hole mobility of four representative hole-transport materials depicted in Figure 4.1 is evaluated using Kinetic Monte Carlo (KMC) simulations. The proposed methodology is validated by comparing the computed mobility results with experimental measurements.

This chapter is structured as follows: Initially, I will provide an outline of the general simulation protocol and delve into computed properties such as HOMO energies and intermolecular couplings. Next, I will explain how energetic disorder is characterized in this study and how it is calculated based on the time series of HOMO energies obtained earlier. Following this, I will discuss how individual molecular properties influence dynamic disorder. Subsequently, I will address fluctuations in couplings and then proceed to discuss simulations of hole mobility.

4.1 Step-by-step description of the protocol

To investigate the influence of both static and dynamic disorder on HOMO energy distributions and intermolecular couplings, a thorough sampling of numerous molecule pairs across multiple time steps is essential. This extensive sampling is made possible by employing semi-empirical quantum chemistry methods. In this study, I turn to the DFTB method [141, 142, 122, 143] to compute the required HOMO energies ε_i and hole couplings J_{ij}[81, 82, 83] (see Chapter 3). In summary I proceed as follows:

(i) The initial step involves generating a realistic model of the amorphous morphology for each mate-

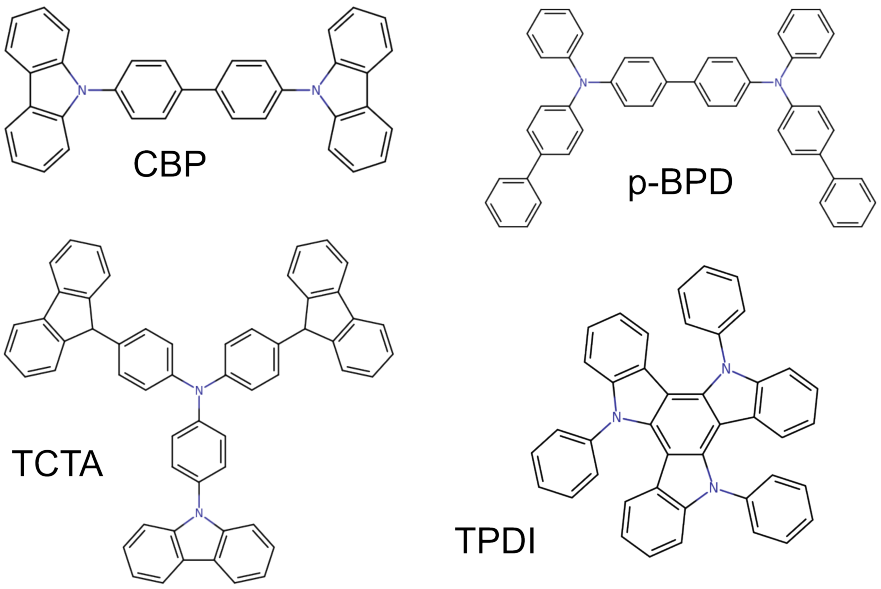

Figure 4.1: Chemical structures of four typical hole transport materials used in OSCs and studied in this work. The full chemical names are: 4,4'-bis(carbazol-9-yl)-2,2-biphenyl (CBP), N,N'-di(biphenyl-4-yl)-N,N'-diphenyl-[1,1'-biphenyl]-4,4'-diamine (p-BPD), 4,4',4"-tris(N-carbazolyl) triphenylamine (TCTA), and 5,10,15-triphenyl-5H-diindolo [3,2-a:3',2'-c] carbazole (TPDI). Reprinted with permission from [121]. Copyright 2024 American Chemical Society.

rial (see Figure 4.1) using the DEPOSIT protocol [9], as discussed in Chapter 3. Properties like packing density and the immediate environment of individual molecules are crucial for hopping transport. Subsequently, a molecular dynamics equilibration of the structure is conducted, followed by the simulation of thermal fluctuations (see Figure 4.2 **a**).
(ii) Following the morphology generation, a MD simulation is conducted to generate the trajectory of the morphologies. During this process, inter- and intra-molecular electronic properties, including orbital energies ε_i, energy-differences between hopping-pairs $\Delta\varepsilon_{ij}$, and electronic couplings J_{ij} are computed for each snapshot. This step is depicted in Figure 4.2 **b)** and **c)**. The fluctuating nature of the transport parameters is illustrated by showing the energetic difference $\Delta\varepsilon_{ij}$ and electronic coupling J_{ij} for one randomly selected molecular pair from one of the morphologies.
This step poses a significant computational challenge due to the substantial number of quantum chemical calculations required to effectively sample static and dynamic disorder. Traditional post-Hartree-Fock or DFT methods become impractical in such cases. Therefore, the study employs the semi-empirical DFTB approach [141, 142] for its efficiency in handling these computational demands.
(iii) To simulate hole transport effectively, the obtained structures and data alone are insufficient. Despite employing highly efficient quantum chemistry methods, the system sizes Ican handle are typically limited to a few thousand molecules. In order to capture the percolative nature of charge transport through mesoscopic systems [144], Iproceed to the third step, where Iperform a stochastic expansion [124, 145] of our energy and coupling distribution to create a virtual hopping network (see Figure 4.2 **e**). Subsequently, hole transport is explicitly simulated using kinetic Monte Carlo (KMC). The disordered nature of the system leads to a percolative character of the charge transport[144, 124].
(iv) In the final step, hole transport simulations are conducted at various applied electric fields. The hole mobility is extracted using our effective time-averaged models, utilizing the LightForge KMC program[124, 146].

4.1.1 Morphology generation & dynamics

Monte-Carlo based morphology generation

The simulation protocol DEPOSIT was previously discussed in Chapter 3. Here, I outline the simulation parameters employed for the deposited morphologies:

- The dimensions of the simulation box were $L_x = L_y = 90\,\text{nm}$ and $L_z = 180\,\text{nm}$.
- In total 2000 molecules have been deposited.
- The total number of moves per SA-cycle was $n = 130000$.
- The start- and end-temperatures in equation (3.61) were $T_s = 300\,\text{K}$ and $T_e = 4000\,\text{K}$.

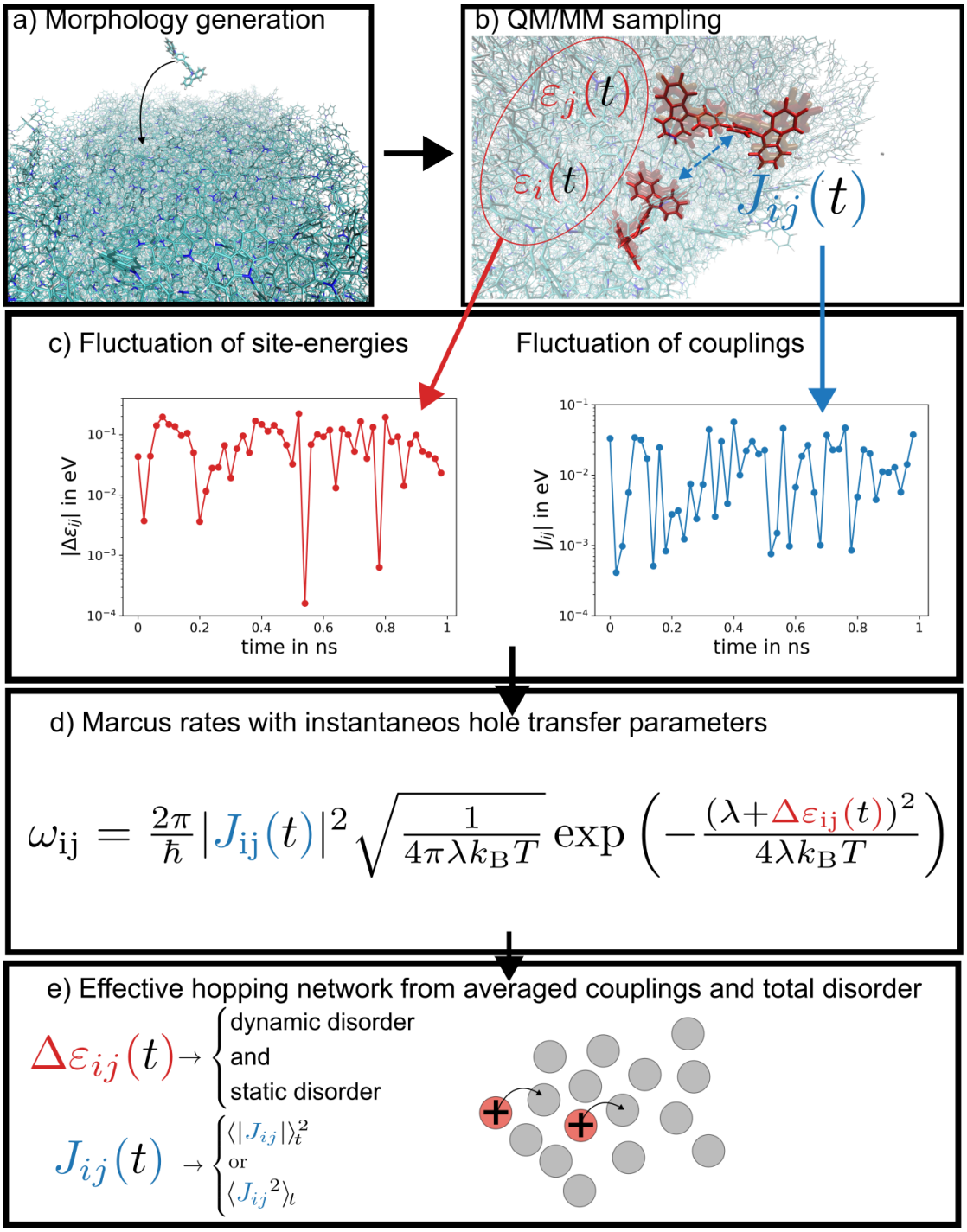

Figure 4.2: Workflow to compute static- and dynamic disorder and to simulate hole transport. All steps of the protocol described here, are illustrated from subfigure **a**) to **e**). Reprinted with permission from [121]. Copyright 2024 American Chemical Society.

- For every deposited molecule 32 SA cycles have been executed in parallel.

Morphology trajectory

Utilizing the aforementioned morphologies, each consisting of 2000 molecules, thermal fluctuations of the molecular structures are obtained through traditional force field-based MD simulations. The setup of the system and subsequent MD simulations are performed using the GROMACS 5.0.4 package[96, 147]. The force field parameters are taken from the GAFF, known for accurately characterizing conjugated molecules and $\pi - \pi$ stacking interactions[90, 91]. Atomic charges are generated through the restrained electrostatic potential (RESP) fitting procedure[148, 149], calculated at the RHF/6-31g* level using the Gaussian 09 package[150, 151]. The energy of the system is minimized using the steepest descent method, and from this geometry, a 2 ns equilibration process is conducted to generate the starting conformation for the MD-trajectory. To maintain temperature and pressure at 300 K and 1 bar, respectively, the Parrinello-Rahman barostat and Nosé-Hoover thermostat are employed during the equilibration process. A total of 500 snapshots with a timestep of $\Delta t = 2$ ps was performed, leading to a total trajectory length of 1 ns.

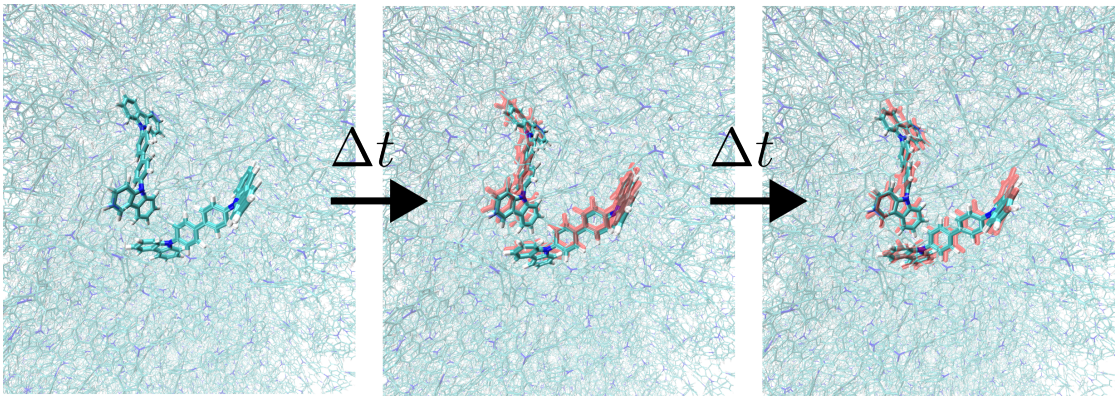

Figure 4.3: Illustration of the molecular dynamics. The image depicts three snapshots of the overall morphology (of CBP), with emphasis on two randomly selected molecules to illustrate their dynamics. The first snapshot on the left displays the system post-equilibration, serving as our starting point. Subsequent snapshots showcase the arrangement at different time points. The transparent red molecules show the molecules in their conformation from the previous snapshot, highlighting the observed conformational changes.

4.1.2 Transport parameters

In Chapter 3, I have introduced the Marcus rate equation to determine the hopping rate for charge transfer between molecules i and j. The Marcus rate equation (3.77) depends on three microscopic parameters:

1. The electronic coupling pertains to the orbitals involved in the charge carrier transition. Specifically, in this research, I focus on hole transport, where J_{ij} represents the coupling between the

HOMO of molecule i and the target molecule j.

2. The difference in the energy of the molecules HOMO energies:

$$\Delta\varepsilon_{ij} = \varepsilon_j - \varepsilon_i \ , \tag{4.1}$$

where ε_j and ε_i represent the HOMO-energy of the target- and initial molecule, respectively.

3. The reorganization energy λ for hole transfer encompasses the impact of conformational alterations resulting from hole transfer. In this study, I assume the reorganization energy to be time-independent. Therefore, for each material depicted in Figure 4.1, the reorganization energy is computed once using the Nelsen-four point procedure [105].

The objective is to understand how the dynamic effects influence the transport parameters. By leveraging insights into the time-resolved behavior, one can elucidate the underlying reasons for dynamic disorder reducing mobility in the materials under investigation. This is discussed below.

4.1.3 Environmental effects on the molecular energies

When evaluating molecular energies, accounting for Coulomb interactions between the molecule of interest and its surroundings is crucial, especially within the realm of organic electronics where polarization effects can profoundly impact molecular energies. An established method, proposed by Friederich et al., addresses environmental polarization arising from the charging of a molecule [152]. This method involves iteratively computing the polarization induced by a charged molecule. Certain molecules are designated as charged centers, and their energies are calculated without considering environmental interactions. Simultaneously, charge densities of surrounding uncharged molecules are computed without molecular interactions. These charge densities, derived from vacuum calculations, are then employed to fit atomic point charges, ensuring accurate replication of the electrostatic potential caused by the charge density [148]. Following this, the energies of both the central molecule and the surrounding molecules are recalculated within the field generated by the previously fitted point charges. The revised charge densities are utilized for a new round of atomic charge fitting to obtain new updated atomic charges. This iterative process continues until the energy of the central molecule reaches convergence.
While this method has shown great success in predicting molecular energies and energetic disorder in amorphous structures, it is computationally demanding. This becomes especially apparent when considering the time dynamics of the structure, making it even more computationally expensive.
In this work, the method proposed by Friederich et al. was not applicable due to its prohibitively high computational costs if applied to the entire MD-trajectories. Therefore, an alternative approach was adopted. Initially, a gas-phase optimization was conducted for one molecule each material using DFT with a B3LYP functional and a def2-SVP basis set. Subsequently, the optimized molecules served as a basis for electronic structure calculations employing HF with a 6-31g* basis set. From the coefficient matrices obtained through the SCF procedure (see Chapter 3), the electron density is computed for the

Table 4.1: Fitted dielectric constants.

Material	ϵ_r
CBP	1.735
p-BPD	1.215
TCTA	1.685
TPDI	2.945

optimized molecule in gas phase. Subsequently, atomic point charges are fitted using the method proposed by Singh et al. [148, 149].
In contrast to the approach proposed in [152], the atomic charges (where I represents each atom of the molecule) are computed only once for a gas-phase optimized molecule.
In simulations involving the HOMO energies, the influence of a charged environment is accounted for using a method, where the central molecule is treated quantum mechanically with the DFTB1 method, and then a coupling term to the classical point charges of the environment is introduced. This approach is referred to as the QM/MM scheme, denoting the combination of quantum mechanics and molecular mechanics. Consequently, the DFTB matrix (introduced in equation (3.40)), introduced in Chapter 3, needs to be updated with [122, 143]:

$$H^0_{\mu\nu} \rightarrow H^0_{\mu\nu} + \frac{1}{2} S^{\alpha\beta}_{\mu\nu} \sum_I \frac{Q_I}{\epsilon_r} \left(\frac{1}{|\boldsymbol{r}_\alpha - \boldsymbol{R_I}|} + \frac{1}{|\boldsymbol{r}_\beta - \boldsymbol{R_I}|} \right). \tag{4.2}$$

In equation (4.2), α and β represent atoms of the central molecule, ϵ_r denotes the dielectric constant, and Q_I denotes the atomic point charge, measured in units of elementary charge, of atoms located outside the quantum mechanical (QM) zone. The overlap matrix between the orbitals of atom α and β is given by $S^{\alpha\beta}_{\mu\nu}$. The summation includes only atoms within a maximum distance of 1.5 nm from the atoms α or β of the molecule in the QM zone. The coupling to the classical point charges Q_I not only affects the on-site energies ($\alpha = \beta$) but also the intramolecular couplings between atoms ($\alpha \neq \beta$).
To replicate the impact of polarization on the HOMO energies, I needed to adjust the dielectric constant to at least achieve an effective polarization in a mean field manner. To do this, I computed the energetic disorder of a frozen morphology and compared it with disorders reported in the work of Kaiser et al. [126], where the method of Friederich et al. [152] was employed for frozen morphologies. I fine-tuned the value of ϵ_r to accurately reproduce the observed energetic disorder.
The values for the obtained dielectric constants for each material can be found in Table 4.1.

4.1.4 Coupling fluctuation strength and timescale

In addition to the energetic disorder, which determines the distribution of HOMO energies and thus plays a critical role in hole transfer, the electronic coupling (as expressed in equation (3.77)) between molecules i and j impacts the hole hopping rate and, consequently, the hole mobility in amorphous OSCs. It is well established that molecular dynamics can induce substantial coupling fluctuations for individual dimers.

Table 4.2: Reorganization energies for hole transport of the four materials studied in this chapter.

Material	CBP	p-BPD	TCTA	TPDI
λ in eV	0.134	0.173	0.206	0.145
τ_{FC} in fs	8.06	6.96	6.40	7.63

Skourtis, Waldeck, and Beratan proposed a theoretical framework for examining and analyzing fluctuations in coupling [137]. This framework provides insights into the temporal dynamics and strength of coupling fluctuation, contributing to a deeper comprehension on the effects amorphous systems. Here, I will provide a brief summary of this discussion to outline the tools utilized in later analysis.

Time scales

To determine whether coupling fluctuations happen quickly or slowly relative to the timescales of molecular dynamics, it's crucial to compute and compare two essential quantities: the Franck-Condon time τ_{FH} and the coherence time τ_{coh}.
The Franck-Condon time is defined as:

$$\tau_{\mathrm{FC}} = \frac{\hbar}{\sqrt{2\lambda k_{\mathrm{B}} T}} \,. \tag{4.3}$$

Here λ represents the reorganization energy associated with hole transfer, as previously defined. The reorganization times obtained for the four materials are provided in the table, along with the corresponding Franck-Condon times at a temperature of 300 K , which are shown in Table 4.2. The coherence time is determined through the analysis of the coupling-autocorrelation function, defined as cited in [136, 138]:

$$C_{ij}(t) = \langle J_{ij}(t) J_{ij}(0)] \rangle_t \,, \tag{4.4}$$

where J_{ij} represents the electronic coupling between the HOMOs of molecular pair (i, j) and $\langle \ldots \rangle$ denotes averaging over all MD snapshots. following approximation can be used[137]:

$$C_{ij}(t) \approx (\langle J_{ij}^2 \rangle_t - \langle J_{ij} \rangle_t^2) \exp\left(-\frac{t^2}{2\tau_{\mathrm{coh}}^2} \right) + \langle J_{ij} \rangle_t^2 \,. \tag{4.5}$$

In order to investigate fluctuation timescales, I randomly selected dimer pairs with a maximum center-of-mass (center-of-mass (COM)) distance of 1.5 nm and conducted MD simulations with a timestep of 1 fs, spanning a total simulation duration of 10 ps. This yielded a total of 10000 MD-snapshots.
To gain further insights into the fluctuations present in the discussed systems, I calculated the autocorrelation function (4.4) for randomly chosen pairs with a maximum center-of-mass (COM) distance of 1.5 nm. Subsequently, the approximation (4.5) was applied and the coherence time τ_{coh} was fitted.
Figure 4.4 illustrates an exemplary coupling-autocorrelation function for a randomly selected molecule

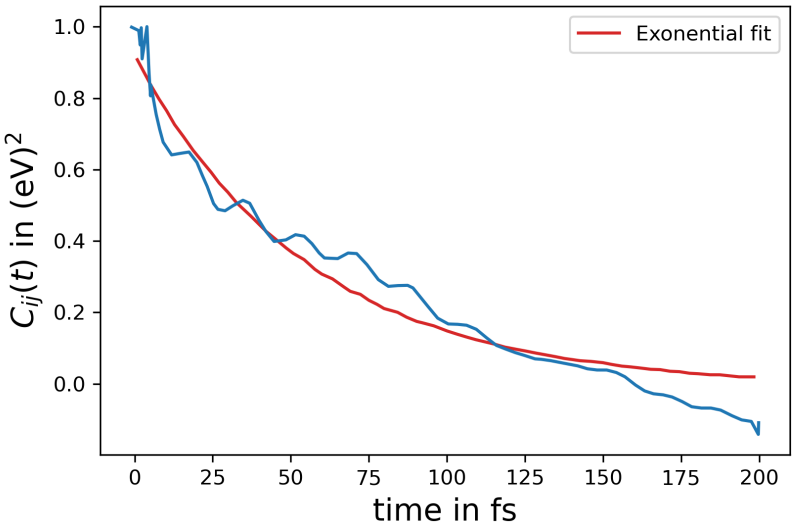

Figure 4.4: Autocorrelation function for electronic coupling of pair (i, j)**.** The autocorrelation function (4.4) was computed for a molecular pair. The approximation (4.5) was then used as a fitting model to extract the coherence time τ_{coh}.

pair meeting the distance criteria. The computed $C_{ij}(t)$ is depicted in blue, while the fitted expression is represented in red. To gain an understanding of typical timescales, the coherence time is determined for numerous randomly selected dimers.

A comparison with the Franck-Condon time for each material indicates that, within our approximations—such as utilizing the reorganization energy for hole transfer of the gas-phase optimized molecule and disregarding outer-shell effects [153] — one can infer from this analysis that coupling fluctuations indeed occur slowly compared to the Franck-Condon time ($\tau_{\text{coh}} > \tau_{\text{FC}}$).

Fluctuation strength

Given that the studied systems fall within the slow coupling regime, I can employ the coherence parameter, as introduced in [137], to quantify the strength of electronic coupling fluctuations:

$$R_{\text{coh}}(i,j) = \frac{\langle |J_{ij}(t)| \rangle_t^2}{\langle J_{ij}(t)^2 \rangle_t} \,, \tag{4.6}$$

where $\langle |J_{ij}(t)| \rangle_t^2$ denotes the square of the time-averaged of the absolute of the couplings and $\langle J_{ij}(t)^2 \rangle_t$ stands for the mean of the time average of the square couplings. The coherence parameter $R_{\text{coh}}(i,j)$ describes the strength of the fluctuations: small values of $R_{\text{coh}}(i,j) \ll 1$ stand for strong coupling fluctuations, allowing the use of $\langle |J_{ij}(t)| \rangle_t^2$, whereby weak fluctuations ($R_{\text{coh}}(i,j) \approx 1$) necessitate the usage

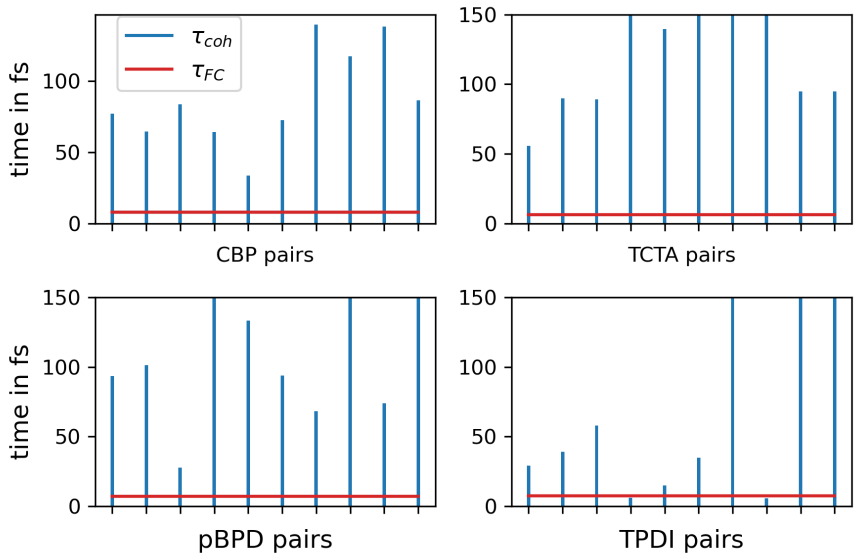

Figure 4.5: Comparison of Franck-Condon and coherence times. Shown are the coherence times (blue) of four randomly picked molecular-pairs. The coherence time was obtained as illustrated in figure 4.4

of $\langle J_{ij}(t)^2 \rangle_t$ to compute time-averaged rates with Marcus formula (3.77) [137].

4.2 Energetic disorder

As previously mentioned, my analysis will focus on examining the energetic disorder, specifically addressing both static and dynamic contributions. To begin, I will investigate the temporal behavior of the HOMO energies of randomly chosen molecules within a particular material.

4.2.1 Time series of molecular energies

Studying the fluctuations in energy of individual molecules randomly selected from various regions within the amorphous matrix can provide insights into the types of motions these molecules undergo. Consequently, I have chosen six molecules from the CBP morphology and plotted their molecular energy $\varepsilon_i(t)$ against the time of the MD trajectory. The fluctuating energies are shown in Figure 4.6, accompanied by the time-averaged values $\bar{\varepsilon}_i = \langle \varepsilon_i(t) \rangle_t$. These histograms of the occurring site energies are depicted in Figure 4.7, clearly illustrating that the HOMO energies follow a symmetric distribution around the expectation value.

The symmetric distribution of energy resulting from time-sampling suggests that molecules within the amorphous matrix undergo harmonic motions like bond length vibration and angular torsion in a combined manner. If the motions were dominated by a single harmonic mode with a distinct frequency,

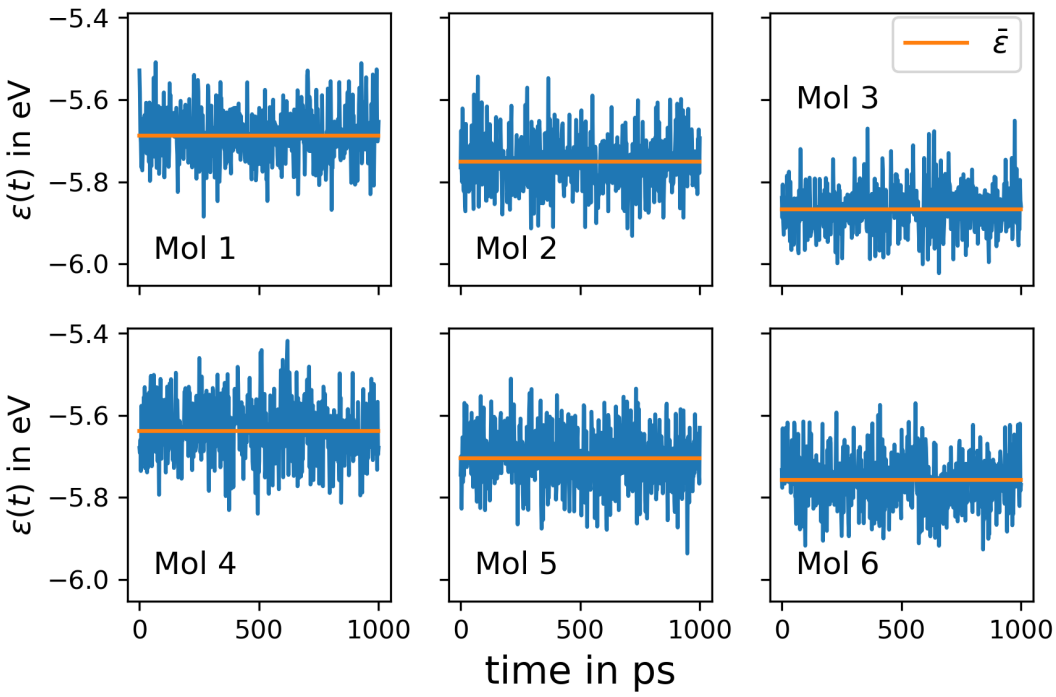

Figure 4.6: Fluctuation of the HOMO energies of six randomly selected molecules from the CBP matrix. The time-series if the energy is shown in blue, the time average $\bar{\varepsilon}$ in orange.

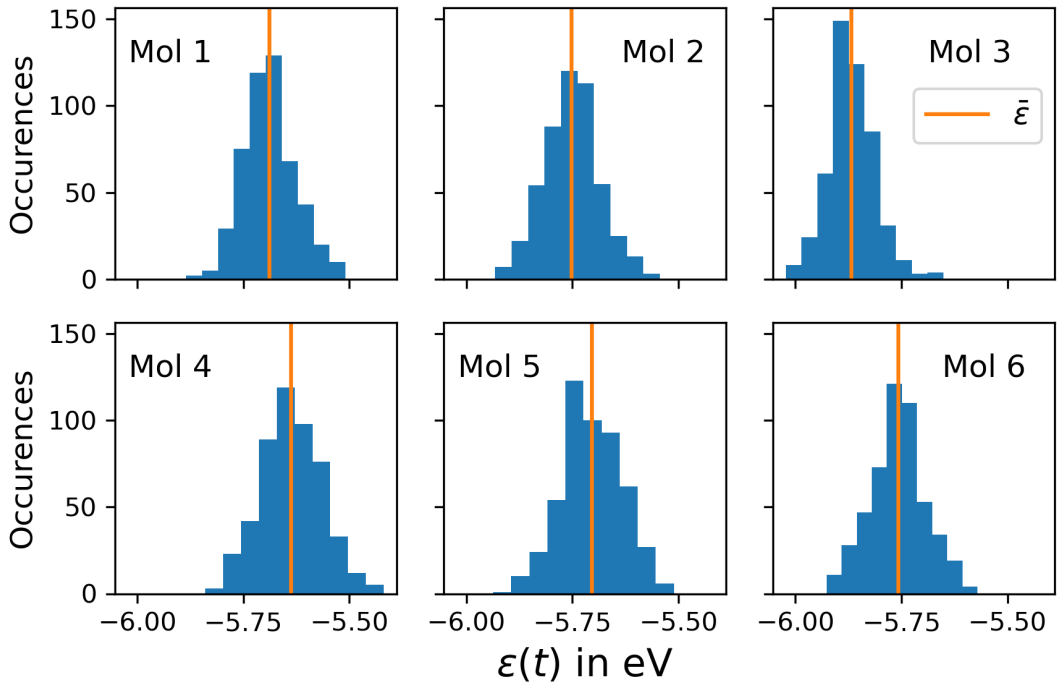

Figure 4.7: Histograms of the fluctuating HOMO energies. The oscillation of CBP molecules and the corresponding energy fluctuations occur symmetrically around the time-averaged mean. This implies that we can compute the expected value by simply taking the arithmetic mean of all values along the time-series.

the distribution of HOMO energies would resemble a bathtub shape rather than a Gaussian shape. The examination of individual molecular energy fluctuations, as illustrated in Figure 4.6 and 4.7, represents an initial step in the analysis of static disorder, which will be defined and discussed in the following section.

4.2.2 Static disorder

To define static disorder, one might initially consider computing the time averages $\bar{\varepsilon}_i$ and then, based on the Gaussian disorder model, calculate the standard deviation regarding the distribution of the time-averaged energies of all molecules. However, this approach overlooks the possibility of spatial correlations between the time-averaged energies of molecules that are in close proximity to each other. Such correlations have already been investigated by Massé et al.[154]. They demonstrated that in amorphous organic semiconductors (OSCs), molecular energies exhibit short-range correlations, which must be taken into account when defining static energetic disorder.
In Figure 4.8, the findings of Massé et al. are illustrated. It can be observed that the variance of the energetic differences of molecules within a certain cutoff radius differs significantly from the naively

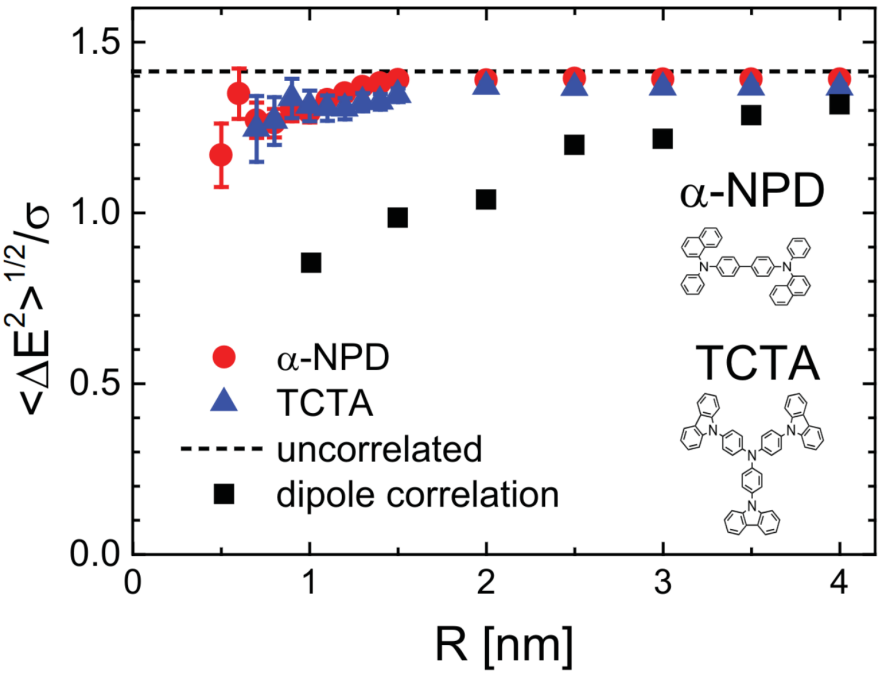

Figure 4.8: Massé et al. studied the correlation between molecular HOMO energies of two typical hole transport materials. Reprinted with permission from [154]. Copyright 2024 by the American Physical Society.

computed variance of site energies. This disparity is particularly pronounced at small pair-distances and serves as a measure of spatial correlation of molecular energies.
To account for such short-range spatial correlations in the definition of the static disorder, I use the following protocol:

- I randomly select a core molecule in the center of the matrix, denoted with index i.
- Compute the time-averaged HOMO energy $\bar{\varepsilon}_i$ of the core molecule.
- I define a sphere with a radius of 1.5 nm around the core molecules COM. All other molecules whose COM is within that sphere are considered to be potential hopping targets j. I then define a list of all pairwise energy differences $\Delta\bar{\varepsilon}_{ij} \equiv \bar{\varepsilon}_j - \bar{\varepsilon}_i$ of the core-molecule and the potential target molecules.
- This procedure is repeated for 400 core molecules leading to a very large number of pairwise energy differences.

Then I define the static disorder as follows:

$$\sigma_s = \sqrt{\frac{\mathrm{Var}[\Delta\bar{\varepsilon}_{ij}]}{2}} \,. \tag{4.7}$$

Where $\mathrm{Var}[\Delta\bar{\varepsilon}_{ij}]$ denotes the variance of the energy differences of all potential hopping pairs. Writing out the variance of the list of pairwise energy differences one finds:

$$\mathrm{Var}[\Delta\bar{\varepsilon}_{ij}] = \mathrm{Var}[\bar{\varepsilon}_i] + \mathrm{Var}[\bar{\varepsilon}_j] - 2\mathrm{Cov}[\bar{\varepsilon}_i,\ \bar{\varepsilon}_j]\,, \tag{4.8}$$

where $\mathrm{Cov}[\bar{\varepsilon}_i, \bar{\varepsilon}_j]$ denotes the covariance between all core molecules i and target-molecules j. If there are no correlations, the covariance between $\bar{\varepsilon}_i$ and $\bar{\varepsilon}_j$ becomes zero, leading to:

$$\mathrm{Var}[\bar{\varepsilon}_i] = \mathrm{Var}[\bar{\varepsilon}_j]\,.$$

Under these circumstances, equation (4.7) would take on the following form:

$$\begin{aligned}\sigma_\mathrm{s} &= \sqrt{\frac{\mathrm{Var}[\varepsilon_i] + \mathrm{Var}[\varepsilon_j] + 0}{2}} \\ &= \sqrt{\frac{2\mathrm{Var}[\varepsilon_i]}{2}} \\ &= \sqrt{\mathrm{Var}[\varepsilon_i]}\,,\end{aligned}$$

This expression essentially represents the standard deviation of the time-averaged energies across all molecules within the system.

Results for static disorder

The normalized histograms of $\Delta\bar{\varepsilon}_{ij}$ and a fitted Gauss-curve are displayed in figure 4.10 in light blue and red, respectively. According to equation (4.7), the width of the Gauss-curve is used to obtain the static disorder. For CBP (top right) and p-BPD (top left), the static disorder is 0.074 eV and 0.075 eV, respectively. Whereas TCTA has a static disorder of 0.085 eV, TPDI has the smallest disorder with 0.071 eV. With the exception of TCTA, the static disorders are very similar and only differ by a few meV. It is intriguing to note the similarity in static disorders among CBP, TPDI, and p-BPD, considering their distinct molecular structures. Predicting the static disorder solely from the molecular structure is therefore very challenging.

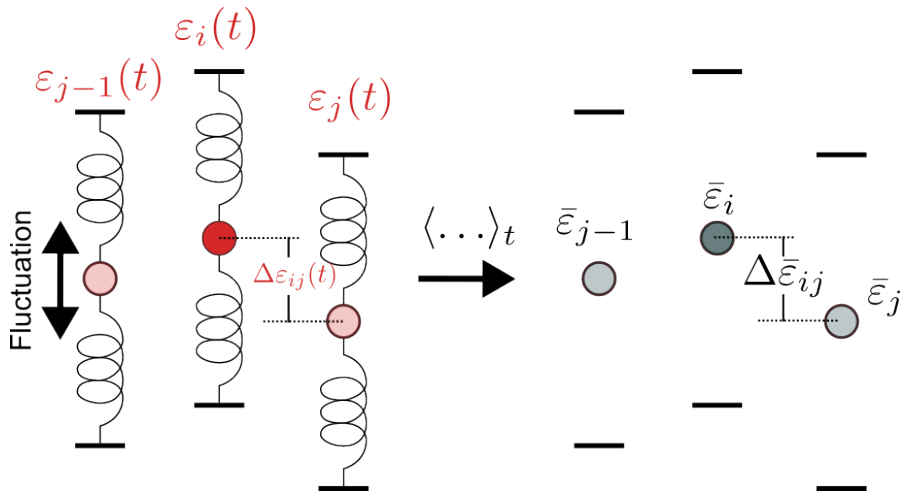

Figure 4.9: Illustration of the construction of the pairwise-energy differences for the energetic disorder in one dimension. The red balls, connected to the springs, represent the HOMO energy of the corresponding molecule. The time-dependent energy differences $\Delta\varepsilon_{ij}(t)$ are illustrated between molecules i and j. On the right the time-averaged site energies and time-averaged site energy-differences $\Delta\bar{\varepsilon}_{ij}$ are shown. For defining static disorder, only the time-averaged energies are relevant. From the perspective of the reference molecule i all molecules within a cutoff radius of 1.5 nm are considered potential target molecules for the hole transfer process. Based on these molecules, I construct the list of pairwise energy differences $\Delta\bar{\varepsilon}_{ij}$.

4.2.3 Dynamic disorder

In the previous section, static disorder was thoroughly examined. Now, the focus shifts to dynamic disorder. To define dynamic disorder, I will revisit the list of pairwise energy differences, previously established. However, instead of analyzing the time-averaged energy differences, the attention will be on the time-dependent fluctuations of each pair. Specifically, I will examine the variance of the time-series for each pair $\Delta\varepsilon_{ij}(t)$. The definition for the dynamic disorder is:

$$\sigma_\mathrm{d} = \sqrt{\frac{\langle \mathrm{Var}_t[\Delta\varepsilon_{ij}(t)]\rangle_{ij}}{2}}\,, \tag{4.9}$$

where $\mathrm{Var}_t[\ldots]$ denotes the variance of the time-series of one pair and $\langle\ldots\rangle_{ij}$ denotes the expected value of the distribution of variances of all pairs.

One might naively assume that computing the mean, as done for the distributions of the time-averaged energy differences, suffices. Figure 4.11 illustrates the distribution of variances for CBP. A closer inspection reveals that the variances are not perfectly symmetrically distributed. Therefore, assuming a Gaussian distribution may not be appropriate.

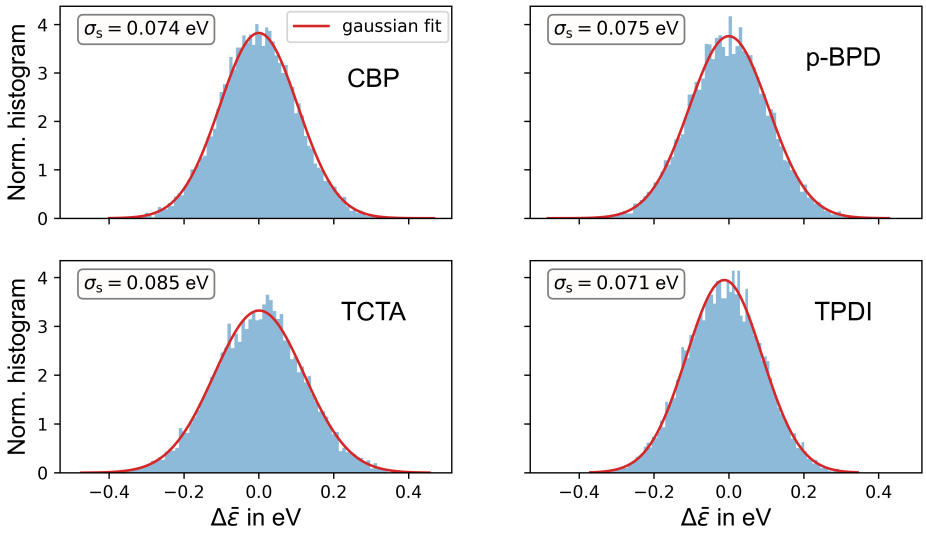

Figure 4.10: Distribution of the time-averaged energy differences of all considered hopping pairs and static disorder σ_s. The distributions of the time-averaged site-energy differences $\Delta\bar{\varepsilon}_{ij}$ are shown in the normalized light blue histograms. A Gauss-curve is fitted as a probability density function (shown in red). We are especially interested in the standard deviation of the fitted Gauss-curve since it relates to the local static disorder σ_s as given in equation (4.7). Considering the chemical structures of the compounds, the static disorder of the materials CBP (top left) and p-BPD (top right) are pretty comparable at 0.074 eV and 0.075 eV, respectively. For TPDI (bottom right), the disorder is slightly below at 0.071 eV. With 10 meV − 14 meV more than the other three materials, the static disorder of TCTA (bottom left) is the highest. Reprinted with permission from [121]. Copyright 2024 American Chemical Society.

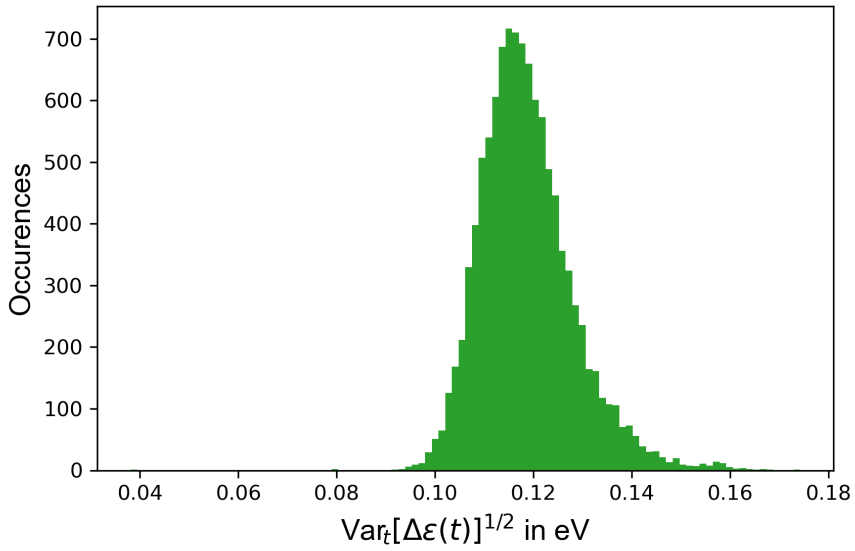

Figure 4.11: Skewed distribution of variance in time-dependent energy difference. The histogram reveals that the variances of the time-series, $\mathrm{Var}_t[\Delta\varepsilon_{ij}(t)]$, form a distribution that lacks perfect symmetry. Rather than assuming a Gaussian distribution, I use the skewed Gaussian distribution defined in equation (4.10).

Instead, I employ the skewed Gaussian distribution for a random variable x, as defined in [155]:

$$g(x,\xi,\omega,\alpha) = \frac{1}{\omega\sqrt{2\pi}} \exp\left(-\frac{(x-\xi)^2}{2\omega^2}\right)\left[1+\mathrm{erf}\left(\alpha\frac{x-\xi}{\omega}\right)\right], \tag{4.10}$$

with the Gaussian error function defined as

$$\mathrm{erf}(x) = \frac{2}{\sqrt{\pi}}\int_0^x \mathrm{d}t\ \mathrm{e}^{-t^2}. \tag{4.11}$$

The parameters ξ, ω and α, determine the position, width, and shape of the distribution. The parameter α represents the skewness. It is worth noting that when $\alpha = 0$ (absence of skewness), the definition reverts to that of the Gaussian distribution, where ξ is the mean and ω the standard deviation.
The mean of the skewed distribution is given by:

$$\langle g(x,\xi,\omega,\alpha)\rangle = \xi + \omega\frac{\alpha}{1+\alpha^2}\sqrt{\frac{2}{\pi}}. \tag{4.12}$$

Results for the dynamic disorder

Figure 4.12 illustrates the distributions of $\mathrm{Var}_i[\Delta\varepsilon_{ij}(t)]^{0.5}$ for all four materials. The histogram is shwon in light green. The fit of the skewed Gaussian distribution is shown in orange. The fit based on the skewed distribution (4.10) is shown in orange.

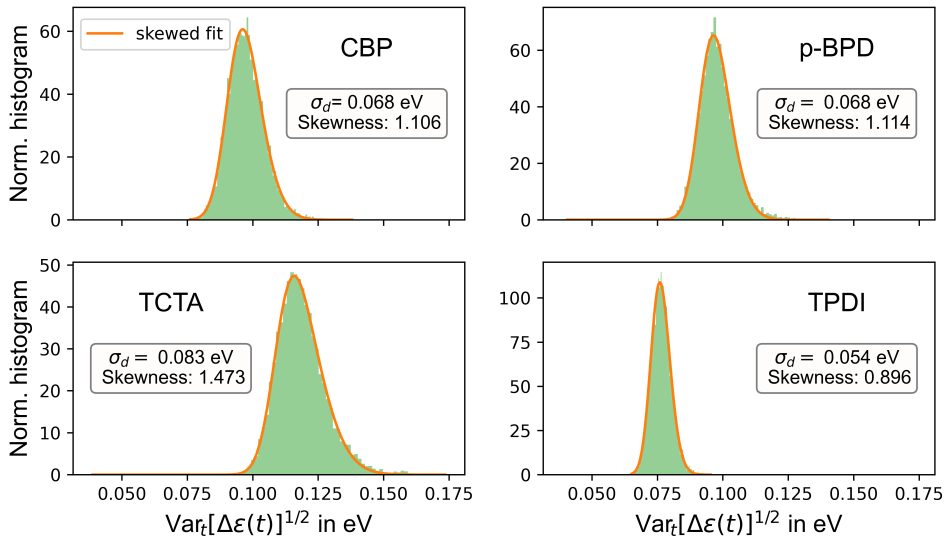

Figure 4.12: Dynamic disorder σ_d. In contrast to the distributions of the time-averaged site energy differences, the standard deviations of the time-series $\mathrm{Var}_t[\Delta\varepsilon_{ij}(t)]^{1/2}$ does not follow a Gaussian distribution. It is better described by a skewed Gaussian distribution. The histograms of $\mathrm{Var}_t[\Delta\varepsilon_{ij}(t)]^{0.5}$ is shown in light green, whereas a fitted skewed Gaussian is shown in yellow. The expectation value of the skewed distribution is computed with the fitting parameters (4.12)and is related to the dynamic disorder according to equation (4.9). Reprinted with permission from [121]. Copyright 2024 American Chemical Society.

For each material, I display the dynamic disorder computed with eq. (4.9) and the skewness of the distribution. Positive skewness can be seen in different degrees in all four materials. The degree of skewness is lowest for TPDI (0.896) and highest for TCTA (1.473). The skewness for CBP (1.106) and p-BPD (1.114) are fairly similar. To calculate the expectation value $\langle\ldots\rangle_{ij}$, the skewness of the distributions has to be taken into account (4.12). The resulting dynamic disorders are, consistent with the static disorders, the highest for TCTA (0.083 eV), lowest for TPDI (0.054 eV), and in between for CBP and p-BPD (both 0.068 eV).

Total disorder

The static (σ_s) and dynamic (σ_d) energetic disorders were determined through statistical examination of the time-averaged differences in HOMO energies ($\Delta\bar{\varepsilon}ij$) and the variances of energy differences across the time series ($\mathrm{Var}t[\Delta\varepsilon_{ij}(t)]$). To combine both static and dynamic disorders into a single effective energetic disorder for the system, I introduce the concept of total disorder as follows:

$$\sigma_t = \sqrt{\sigma_s^2 + \sigma_d^2}\,. \tag{4.13}$$

Table 4.3: Static, dynamic and total energetic disorders computed in this work compared to the disorders reported in the literature.

Material	σ_s	σ_d	σ_t with eq. (4.13)	Literature
CBP	0.074 eV	0.068 eV	0.100 eV	0.096 eV[153]
p-BPD	0.075 eV	0.068 eV	0.101 eV	0.094 eV[126]
TCTA	0.085 eV	0.083 eV	0.119 eV	0.107 eV[126]
TPDI	0.071 eV	0.054 eV	0.089 eV	0.082 eV[126]

The static, dynamic, and total energetic disorder values for the materials under study are presented in Table 4.3, alongside a comparison with reported energetic disorders from the literature (refer to Figure 4.1).

Comparison of static and dynamic disorder values reveals that for TPDI, static disorder significantly outweighs dynamic disorder in contributing to total disorder. Conversely, for TCTA, both static and dynamic disorder contribute equally to total disorder. Notably, CBP and p-BPD exhibit remarkable similarity in dynamic and static disorder values. Comparing the static and dynamic disorders of TPDI with those of CBP and p-BPD, it is noteworthy that while static disorders are very similar, TPDI shows markedly smaller dynamic disorder, resulting in a smaller total disorder. In order to understand this, it is useful investigate the electronic structure of the HOMO and how it is effected by structural changes of the molecules.

A literature review indicates that studies utilizing the frozen morphology approximation consistently yield energetic disorders similar to the total disorders (4.13) obtained in this study. This consistency is attributed to the frozen morphology inherently capturing a conformational state where molecules are notably elongated from their average energies, thus implicitly encompassing aspects of dynamic disorder. Explicitly distinguishing between static and dynamic disorder offers the advantage of gaining insights into how thermal structural changes interact with the chemical structure of the charge transport material and influence the HOMO energy.

Single molecule analysis of HOMO dynamics

In order to provide a qualitative explanation supporting the findings outlined in Table 4.3, I examined five snapshots of a randomly selected molecule from each of the materials. These snapshots were taken at intervals of 200 ps. For each snapshot, I conducted a single point calculation to visualize the HOMO and to illustrate the extent of HOMO variability across the snapshots. This analysis is crucial because alterations in the HOMO structure can be linked to changes in the HOMO energy of the molecules.

Beginning with CBP and p-BPD, both of which exhibit nearly identical dynamic disorder, the visualized HOMOs are depicted in Figure 4.13. The top row represents the CBP molecule, while the bottom row corresponds to the p-BPD molecule. The snapshots are arranged from left to right. It is evident that in most cases, the HOMO is extensively delocalized over the CBP molecule. However, for certain conformations, the primary portion of the HOMO localizes on one of the two side-groups, referred to as carbazole groups. Similar observations apply to p-BPD, where the HOMO exhibits delocalization across

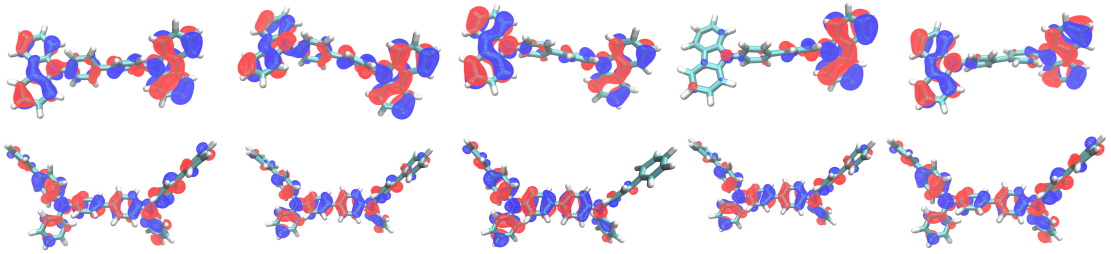

Figure 4.13: HOMO across five snapshots of a single CBP and p-BPD molecule within the amorphous structure. Both molecules share a similar structure centered around a biphenyl unit with rotatable side groups. In most snapshots, the HOMO exhibits delocalization across the molecule.

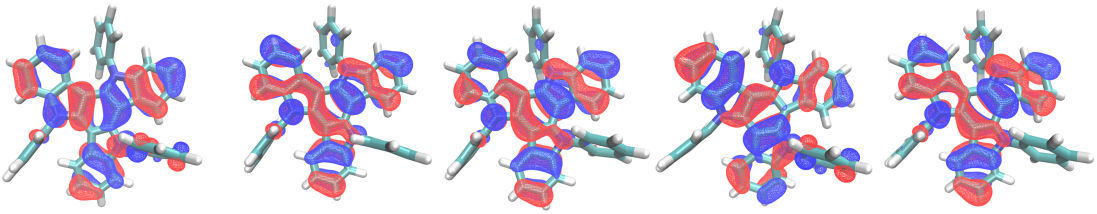

Figure 4.14: HOMO for TPDI snapshots. The main part of the HOMO is localized on the central part of the molecule that moves to less extend than for example the rotation of dihedral angles. This is an explanation for the relatively weak fluctuation induced change of the HOMO energies of TPDI molecules and consequently to a relatively small dynamic disorder.

the entire molecule, yet for specific conformations, such as the one depicted in the middle snapshot, the HOMO does not localize on the phenyl group. It can be inferred that since both molecules share a similar structure with a biphenyl group in the center and either carbazole or one phenyl and one biphenyl group attached via a carbon-nitrogen bond, molecular fluctuations exert a comparable influence on energy fluctuations and therefore the dynamic disorder for these molecules.

The TPDI structure exhibits the smallest dynamic disorder. Once again, I investigate into the investigation of the Highest Occupied Molecular Orbital (HOMO) and its response to structural changes induced by molecular dynamics (MD) simulations. Figure 4.14 displays five snapshots of a randomly selected molecule from the TPDI morphology. Across these snapshots, the HOMO consistently localizes predominantly on the central part of the molecules. This central region is relatively inflexible due to the absence of dihedral bonds that are easy to rotate, in contrast to the bending of the pi-conjugated structure in the center. The movable phenyl units positioned at the top, bottom left, and bottom right minimally affect the HOMO orbital. Consequently, this results in a relatively minor fluctuation-induced alteration in the HOMO and, consequently, its energy.

The TCTA-morphology exhibits the largest dynamic disorder. Building upon the argumentation employed in the discussion of dynamic disorder in other materials, Figure **??** clearly illustrates significant variations in the shape of the HOMO, and consequently its energy, across different snapshots. This variability can be attributed to the extensive delocalization of the HOMO across numerous rotatable

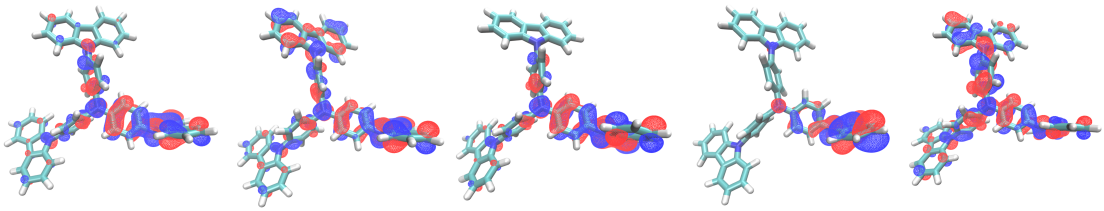

Figure 4.15: HOMO for TCTA snapshots. Compared to the other four materials depicted in Figures 4.13 and 4.14, it's evident that the HOMO of TCTA is significantly more affected by molecular fluctuations. This heightened susceptibility can be attributed to the interplay of delocalized orbitals over multiple dihedral bonds within the TCTA structure.

Table 4.4: Pearson correlation coefficients ρ between the time-averaged site-energy differences $\langle \Delta\varepsilon_{ij}(t) \rangle_t$ and the variance of the temporal fluctuations of the site-energy differences $\mathrm{Var}_t[\Delta\varepsilon_{ij}(t)]$.

Material	ρ
CBP	0.012
p-BPD	-0.014
TCTA	0.025
TPDI	0.018

dihedral bonds, rendering it susceptible to molecular fluctuations. In certain instances, the HOMO spans the entire molecule, while in others, it localizes only on specific single or double arms of the molecule. However, equation (4.13) implies absence of correlation between $\Delta\bar{\varepsilon}_{ij}$ (illustrated in figure 4.10) and $\mathrm{Var}_t[\Delta\varepsilon_{ij}(t)]$ (shown in figure 4.12). Therefore I have examined the Pearson correlation coefficient ρ between $\Delta\bar{\varepsilon}_{ij}$ (illustrated in figure 4.10) and $\mathrm{Var}_t[\Delta\varepsilon_{ij}(t)]$ (shown in figure 4.12). The correlation coefficients for all four materials are presented in table 4.4, indicating a negligible correlation. This observation justifies the use of equation (4.13) to compute the total disorder σ_t.

4.3 Analysis of the couplings

In addition to energetic disorder, which governs the distribution of HOMO energies and hence plays a crucial role in hole transfer, the hopping rate depends quadratically on the absolute of the coupling between molecules i and j, eqaution (3.77). It is widely recognized that molecular dynamics can induce significant coupling fluctuations for individual dimers. I investigate whether these coupling-fluctuations are averaged out if throusands of hopping pairs are considered. Consequently, I analyze electronic couplings along an MD trajectory spanning 1 ns, comprising a total of 50 snapshots.
In this context, I study the influence of molecular fluctuations on coupling properties not at the level of individual dimers, but on a larger scale involving thousands of hopping-pairs. To achieve this, for each snapshot, I construct a histogram of COM distances of pairs within the bulk system. Then, for all molecular pairs within each distance-bin d, I average the couplings between all hopping pairs associated to that distance bin. The obtained averaged couplings as a function of the COM-distance are denoted with $J_{\mathrm{bulk}}(d)$.

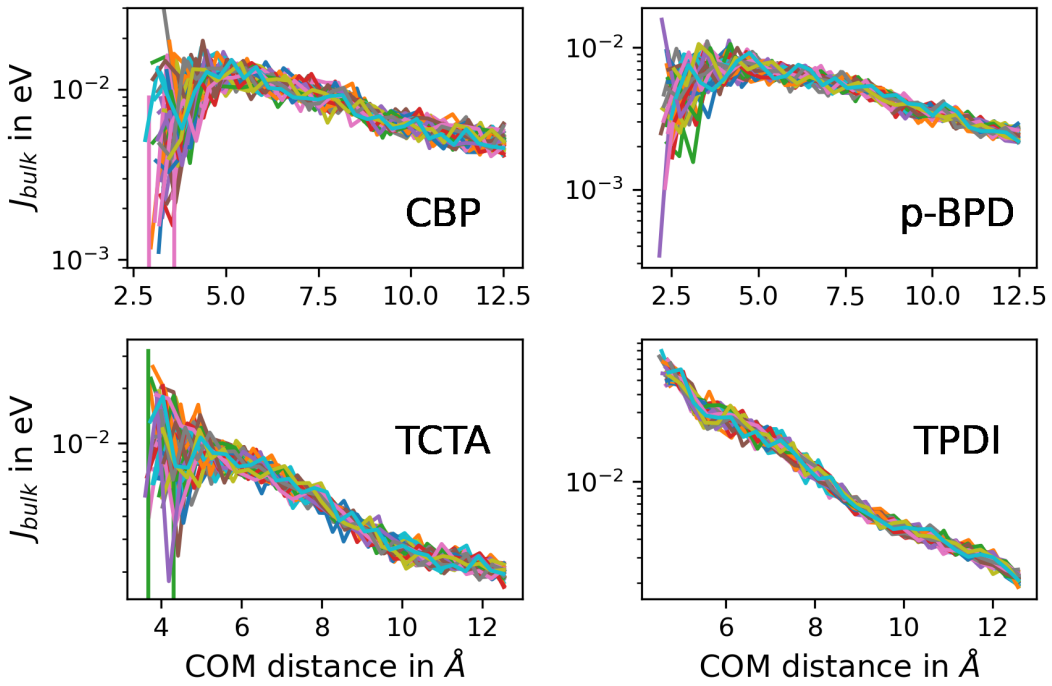

Figure 4.16: Electronic couplings as a function of the COM-distance. For each of snapshot, the couplings of pairs with the same COM-distance d are averaged to form the effective bulk coupling J_{bulk}. The colors denote different snapshots. For CBP (top left), p-BPD (top-right), and TCTA (bottom left), the couplings fluctuate in the region below 5.0 Å COM-distance, with fluctuations exceeding approximately one order of magnitude. For TPDI, the coupling fluctuations are significantly weaker, even for short COM-distances. Reprinted with permission from [121]. Copyright 2024 American Chemical Society.

4.3.1 Snapshot couplings

In figure 4.16, the averaged couplings J_{bulk} are plotted against the center of mass distance for all 50 snapshots and for each material. The colorr represent the snapshots. It is evident that for CBP, p-BPD, and TCTA, the coupling fluctuations are significant in the range of small COM-distances. Within this range, the couplings fluctuate by approximately one order of magnitude. However, for larger COM-distances, the coupling fluctuations become negligible. This means that within the amorphous matrix, coupling fluctuations only impact the hopping rates between molecules with a short COM-distance (below 5 Å). In TPDI, the coupling fluctuations are relatively small, within a factor of 2-3.

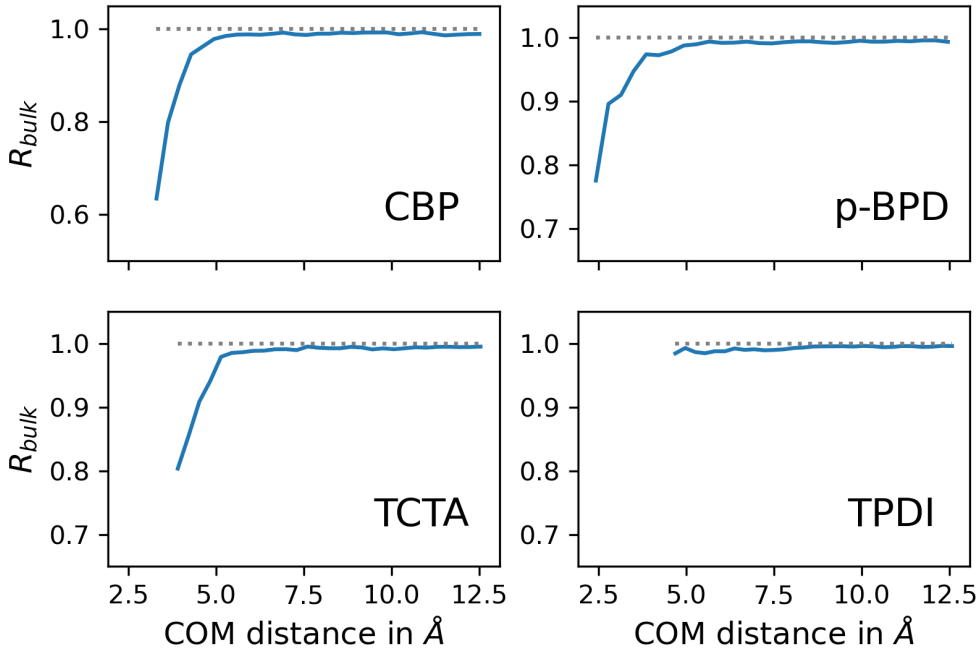

Figure 4.17: Coherence parameter of the bulk couplings. The fluctuation strength of the bulk couplings is examined using the bulk coherence parameter R_{bulk}. If $R_{\text{bulk}} \ll 1$, it indicates strong coupling fluctuations. If $R_{\text{bulk}} \approx 1$, the fluctuations are weak. As previously discussed in figure 4.16, the coupling fluctuations of CBP, p-BPD, and TCTA are relatively strong in the COM-distance regime below 5.0 Å and approach one for increasing COM-distances. These coupling fluctuations are only relevant for short-range hole hopping. For TPDI, the fluctuations of the bulk couplings are negligible. Reprinted with permission from [121]. Copyright 2024 American Chemical Society.

4.3.2 Coherence parameter

Another approach to assess the fluctuation strength of the couplings is investigating the coherence parameter. The coherence parameter for dimers is defined in equation (4.6). I extend this definition to the bulk couplings introduced above:

$$R_{\text{bulk}}(d) = \frac{\langle |J_{\text{bulk}}(d,t)| \rangle_t^2}{\langle J_{\text{bulk}}(d,t)^2 \rangle_t} \,. \tag{4.14}$$

Figure 4.17 shows the coherence parameter for the bulk R_{bulk} as a function of the COM-distance d. In the regime of short COM-distances, the coherence parameter is notably below 1 for CBP, p-BPD, and TCTA. As COM-distances increase, R_{bulk} tends towards 1, indicating that fluctuations in that distance regime have negligible effects on the bulk couplings. For TPDI, the coherence factor is nearly 1 for all distances.

4.4 Hole transport simulations

In the kMC-based hopping transport simulations, I rely on the fundamental assumption that the atomistic system can be represented as a coarse-grained hopping network consisting of sites representing the COM of the molecules. Simulation of the hopping processes takes place using this 3D coarse-grained model, utilizing the discussed couplings and energetic disorders to construct the hopping network. Achieving numerically stable kMC simulations demands a significantly larger number of sites compared to the number of molecules manageable at the microscopic level [144], rendering it impractical to directly construct coarse-grained hopping networks from atomistically resolved morphologies. Consequently, expansion approaches for the site distribution, site energies, and inter-site couplings become necessary to construct suitably large hopping networks.

4.4.1 Generating the hopping-network

Baumeier et al. [145] proposed a method to expand atomistic morphologies, site energies, and couplings into large coarse-grained hopping networks using a stochastic process called the dominance competition process. Initially, N points S_n are randomly and uniformly generated within a 3D simulation box. The number of points is obtained from the density of microscopic COM points and the volume of the simulation box. To account for the spatial extent of the molecules, each point S_n is assigned a spherical radius R_n. These radii are determined based on the nearest neighbor distribution of the microscopic system. Points that lie within the radius of another point are then removed from the simulation box, leaving behind points that have a distance to their nearest neighbor greater than or equal to R_n. However, this approach does not effectively reproduce the short-range order of the microscopic system [156]. To address this limitation, Baumeier et al. proposed an iterative method where independent realizations of the dominance competition approach are performed iteratively. In each iteration, if new points overlap with points from earlier realizations, the new points are discarded. This iterative process is repeated until the density of COM points matches that of the microscopic system. The dimensions of the simulation box used here, were $40 \times 40 \times 40$ nm^3. Periodic boundary conditions (PBC) were applied in all three dimensions. The energies for the generated points are drawn from a Gaussian distribution where the total disorder σ_t (4.13) was the distribution width.

Expanding the intramolecular couplings is done in a two-step procedure, described in the supporting information of the paper of Symalla et. al [124]: first, the center of mass distances d_{ij} of all molecular pairs with $d_{ij} < 15$ Å are binned into 100 bins. These bins are referred to as 'distance' bins k. Within each distance bin k, the absolute values of all associated couplings $|J_{ij}(d_{ij} \in d_k)|$ are binned into another 100 bins, denoted as 'coupling' bins m so that 100 'coupling' bins are nested in every 'distance' bin. This is necessary because, for non-spherical molecules, two different dimers with identical COM-distances may exhibit significantly different orbital overlaps (and hence electronic couplings) due to varying mutual molecular orientations. To assign an electronic coupling to a site-pair in the expanded hopping-site distribution, a coupling-value J_m is randomly chosen from the coupling bins m in the corresponding

distance bin k. The randomly chosen coupling-values are weighted with:

$$w_{km} = \sum_{n=k-2}^{k+2} \sum_{\substack{ij \\ d_{ij} \in n}} \exp\left(-\frac{(\log_{10} J_m - \log_{10} |J_{ij}|)^2}{2\kappa_k^2} \right), \tag{4.15}$$

where the first sum runs over the the two neighbored distance bins, the second sum over all explicitly computed pair-couplings with $|J_{ij}(d_{ij} \in Rd_n)|$. The parameter κ_k is given as five times the bin width of the coupling bins in the distance bin k of interest.

4.4.2 Frozen snapshot mobility

Prior to computing the hole mobility (as described in Chapter 3 for the mobility protocol) in systems where dynamics are explicitly considered, I investigate the extent of variability in hole mobility when computing the mobility using frozen snapshots of the morphology. Specifically, I analyze the mobility of 11 randomly selected snapshots from the MD trajectory, treating the morphology as frozen and using the site energies and couplings from these snapshots without incorporating explicit dynamics. The energetic disorder for the frozen snapshots is defined as

$$\sigma_{\text{snapshot}} = \frac{\text{Var}[\Delta\varepsilon_{ij}^{\text{snapshot}}]^{1/2}}{\sqrt{2}}, \tag{4.16}$$

where $\Delta\varepsilon_{ij}^{\text{snapshot}}$ represents the HOMO-energy differences of the frozen snapshot morphology. This approach mirrors the methodology employed in many prior studies [122, 6, 123, 124, 126, 125].
Based on the energetic disorders of the snapshot and the snapshot couplings, the stochastic expansion from microscopic to coarse grained structures is performed as discussed above. Once a hopping network is established, 30 holes are randomly distributed among the sites in the network. This results in a total charge concentration of approximately 0.0004 per site, which is a typical value [157]. Figure 4.18 illustrates the mobility of the snapshots, depicted by colored lines, and compares the simulated results with experimental mobility data from the literature [158, 159, 160, 161].
For CBP, the obtained mobility fluctuates over approximately one order of magnitude for all applied electric fields, with some computed mobilities matching perfectly with experimental values. The computed mobility for p-BPD varies by a factor of 3 and slightly underestimates the mobility. Similarly, for TCTA, the mobility varies by a factor of 4, although the field-dependent trend is reproduced quite well. For TPDI, mobility variations by a factor of approximately 2 are observed, with the simulated mobility slightly underestimating the experimental values. Considering experimental uncertainties, however, a deviation between simulated and measured mobility by a factor of 2-3 can still be interpreted as a very good agreement.
The reason for the relatively successful simulation of hole mobility despite using the frozen morphology approximation for couplings and energetic disorders is that parts of the dynamic contribution to the disorder are accounted for through non-equilibrium conformations found in the frozen snapshot.

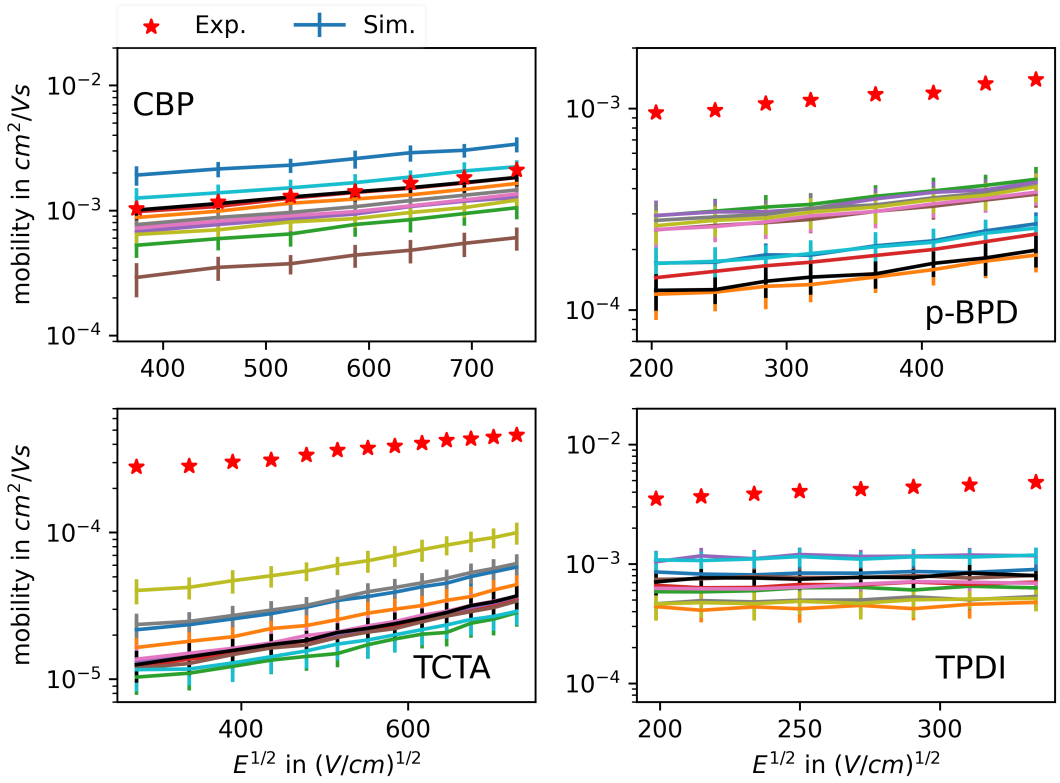

Figure 4.18: Hole mobility for frozen snapshot morphologies. The simulated mobility for all four materials with frozen snapshot morphologies is plotted as colored lines alongside the experimental data [158, 159, 160, 161] (represented by red stars). The simulated mobility for all four materials varies by a factor of 3-10 between the snapshots. Considering experimental uncertainties, the simulated mobility for all four materials is reasonably in agreement with experimental data. Reprinted with permission from [121]. Copyright 2024 American Chemical Society.

Nevertheless, the deviation in mobility among the snapshots indicates that the frozen snapshot approximation introduces another source of uncertainty into mobility prediction.

4.4.3 Hole mobility with explicit consideration of dynamics

Figure 4.18 illustrates the significant range of mobility values observed in simulations across individual snapshots, with deviations spanning up to tenfold differences. Addressing and mitigating this inherent variability and randomness is crucial. One approach to tackle this issue is by calculating the average mobility across all snapshots, which can reduce the dependency of mobility on specific snapshots but may not fully reveal how structural dynamics influence energetic disorder and therefore the mobility. Simply averaging mobility values could obscure important insights into structural dynamics.
To achieve a more comprehensive understanding of how structural dynamics impact mobility, partic-

ularly by explicitly considering static and dynamic disorder along with time-averaged couplings, it is essential to incorporate these quantities directly into the mobility calculation.
Hence, I incorporate the total disorder σ_t, defined in equation (4.13), which explicitly considers both static and dynamic disorder as the distribution width of the Gaussian distribution used in the stochastic model of the hopping matrix.
Regarding the couplings, I compare two approaches: one using the square of the averaged couplings $\langle |J| \rangle_t^2$ and the other using the average of the squared couplings $\langle J^2 \rangle_t$.
Figure 4.19 depicts the obtained mobility using both coupling averaging methods alongside the average mobility from the snapshots shown in Figure 4.18, for comparison. In the case of CBP, all three approaches—incorporating total disorder with averaging squared couplings (blue), incorporating total disorder with square-averaged couplings (orange), and using average snapshot mobility (green) demonstrate excellent agreement with experimental data.
For p-BPD, the mobility for orange and green are equal and underestimate the experimental data by a factor of 5. The result is slightly improved by using the blue approach.
Regarding TPDI, simulations based on both averaging methods exhibit reasonably good agreement with experimental data. This can be attributed to the weak coupling fluctuations for TPDI, as shown in Figure 4.17. The snapshot-averaged mobility performs the worst here, underestimating the experimental values by nearly one order of magnitude. The field dependency of the mobility is accurately captured for CBP, p-BPD, and TPDI.
For TCTA, all three methods underestimate the experimental mobility by a factor of approximately 10 and overestimate the field dependency, as the simulated mobility increases much faster than the measured mobility. This discrepancy might be explained by an overestimation of the total disorder for TCTA. Compared to the disorder reported in [125], the total disorder here is larger by 12 meV, which has a considerable effect on the mobility and also on the field dependency [162].

4.5 Conclusion

Predicting charge mobility in organic semiconductors is a critical area of research, and current methods [126, 153] often rely on assumptions of a static morphology to simplify computations. Dynamic effects on intermolecular couplings are typically neglected due to their high computational demands [135]. Additionally, unraveling the dynamic contribution to energetic disorder remained challenging, making it difficult to predict disorder based solely on single-molecule analyses of fluctuations in site energies.
In this study, I focus on the dynamics of molecules within an amorphous matrix with respect to the total disorder of HOMO energies and intermolecular HOMO couplings. This is achieved through a workflow that combines molecular dynamics, semi-empirical DFTB, and kinetic Monte Carlo simulations. This workflow involves computing time-series data for couplings and site energies, allowing for an investigation into the dynamics of hole transfer parameters across the morphology.
By explicitly considering both static and dynamic contributions to total energetic disorder and performing time averaging of electronic couplings, this approach broadens the scope of energy and coupling

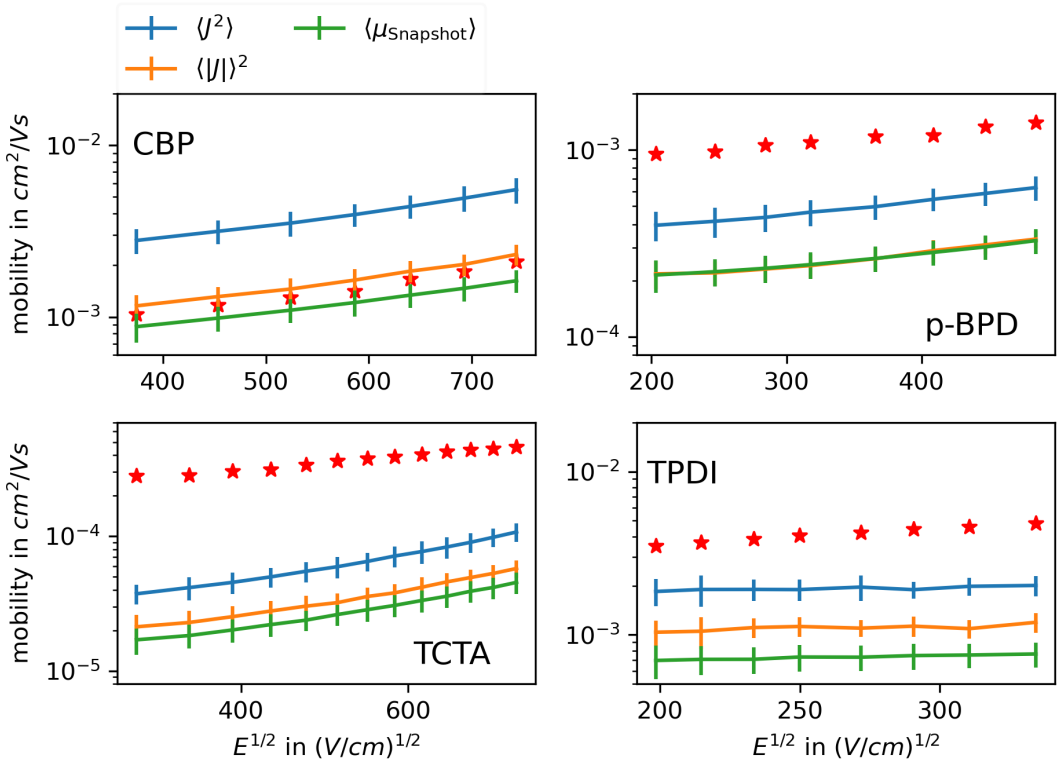

Figure 4.19: Mobility simulations with averaged hole transfer parameters. The mobility is computed using the square averaged couplings (orange) and averaged square couplings (blue). The energy landscape of the hopping network for the kMC simulations was obtained by drawing random site energies from a Gaussian distribution where the total disorder σ_t served as the standard deviation. The experimental data [158, 159, 160, 161] is again shown as red stars. For CBP, the 'orange' simulation yield excellent agreement with experimental mobility. Using the 'blue' method overestimates the mobility by a factor of roughly 3. For p-BPD and TPDI, good agreement with the experimental data is obtained for the 'blue' approach. The 'green' mobility for both is slightly below. The difference between the 'blue' and 'orange' mobility in TPDI is very small due to the weak coupling fluctuations discussed earlier. The mobility for TCTA deviates by approximately one order of magnitude from the experimental values. Reprinted with permission from [121]. Copyright 2024 American Chemical Society.

sampling in amorphous OSC. As a result, mobility predictions can be made that explicitly account for structural dynamics and insights are gained into the underlying physical causes of total energetic disorder, which stem from both static and dynamic influences.

Furthermore, I investigate the fluctuations in intermolecular couplings using a method similar to that employed by Skourtis et al. [137], which reveals that coupling fluctuations significantly impact short-distance pairs. However, for larger center-of-mass (COM) distances, these fluctuations become negligible. Analyzing the HOMO structure within random molecules of each material allows to uncover the origins of dynamic disorder. This exploration provides insights for designing materials with low dynamic disorder, achieved either by localizing the HOMO on rigid fragments of the molecule or using materials with high glass temperatures to reduce molecular flexibility at room temperature (see Figure 4.11).

5

In silico study of OLED architectures

The work presented here was published in:
Ali Deniz Özdemir, Fabian Li, Franz Symalla, Wolfgang Wenzel. In silico studies of OLED device architectures regarding their efficiency. Front. Phys. 11:1222589. 2023 [163]

In preceding sections, particularly in Chapter 2, I extensively discussed the development and current state of OLED devices. In the forthcoming chapter, I will explore the simulation of the efficiency of three distinct OLED architectures. To attain high efficiency in an OLED, it is essential that every electron-hole pair injection results in recombination on an emitter molecule within the emissive layer, followed by radiative decay. However, the efficiency can be reduced by diverse physical processes like exciton-exciton or exciton-polaron quenching or by inefficient carrier injection. Enhancing OLED efficiency necessitates optimizing the interaction among different layers and physical phenomena like charge injection, transport, recombination, and exciton decay. Meticulous material selection and layer arrangements can mitigate loss mechanisms while maximizing quantum efficiency. Computational simulations are promising tools for optimizing OLED performance, efficiently exploring a broad parameter space, and offering insights into the intricate processes occurring across different scales [164, 165].
The goal is to assess the effect of each layer on key performance parameters, including charge balance, exciton generation, and the occurrence of quenching events such as exciton-polaron quenching [166, 27], and exciton-exciton annihilation [167, 54]. This analysis aims to elucidate the influence of these factors on the internal quantum efficiency internal quantum efficiency (IQE), a pivotal metric for evaluating OLED efficiency. Additionally, I aim to optimize the device by adjusting parameters such as the

EML thickness and emitter concentration. In the study presented in this chapter, I examined the impact of integrating charge injection and blocking layers [168] within the framework of a mesoscopic OLED model, using a 3D KMC approach [124, 6], similar to the one used in Chapter 4.
This chapter is organized into two main parts. The first part will focus on three OLED architectures studied in this work, followed by a comprehensive discussion of all microscopic processes involved, including charge injection, charge transport, excitonic processes, and their implementation in this study. In the second part, I will conduct an analysis of the performance of the presented device architectures. I will also present possible optimization strategies and evaluate them using the model developed in this work.

5.1 Parametric model of an OLED

In contrast to the approach detailed in Chapter 4, where amorphous thin film morphologies were initially generated followed by obtaining transfer parameters using quantum chemical methods, I rely on parametric models of OLED devices. Utilizing the LightForge kMC simulation package [124], I simulate the injection and transfer of charge, the formation of excitons, their radiative and thermal decay, as well as bimolecular quenching [54]. To explore three different device architectures, illustrated in Figure 5.1, I employ a heuristic model akin to previous studies [164]. Further elaboration on the simulation setup and process-rate calculations is provided below.

5.1.1 Virtual devices

In this work, I conceptualize OLED devices as a sequence of layers, each consisting of a 3D cubic lattice with a lattice constant of $a = 1\,\mathrm{nm}$ [169, 51]. At every lattice site i, I attribute HOMO and LUMO energy levels, denoted as E_i^{H} and E_i^{L} respectively. These energy levels are randomly sampled from a Gaussian distribution [6], $g(E, \sigma, \langle E \rangle)$, where $\sigma = 0.1\,\mathrm{eV}$ represents the energetic disorder for both HOMO and LUMO energy levels, across all materials incorporated in our investigation. Figure 5.1 illustrates the mean values $\langle E \rangle$ of the HOMO and LUMO energy levels for each layer.
I classify molecules or sites into two distinct groups: phosphorescent emitters and non-emitters. This differentiation is pivotal for modeling different excitonic processes, including inter-system crossing and the radiative decay of singlets or triplets. It relies on the exciton parameters specific to each type, detailed further in the supplementary information. Notably, the materials utilized for charge injection, transport, and blocking layers are all non-emissive. Conversely, emitters are combined with non-emitting host molecules within the emissive layer (EML).

5.1.2 Charge carrier injection

The process of charge injection from an electrode to an organic molecule is considered as a discrete event, where a charge carrier moves from a continuous pool of charges in the electrode to a particular organic site i with an associated energy level (E_i^{H} for holes, E_i^{L} for electrons). To accommodate the

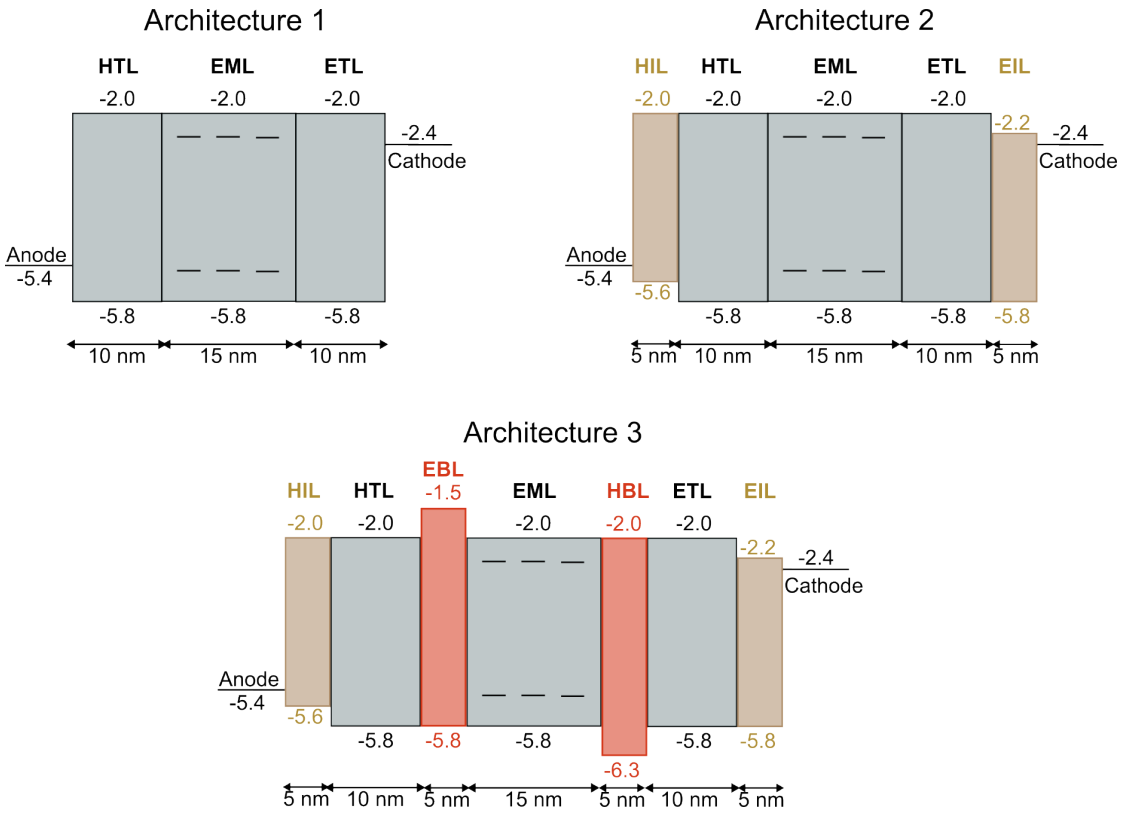

Figure 5.1: Schematic representation of the devices studied in this work. The first device (A1) comprises three layers, with the HTL and ETL having identical thicknesses and energy levels. Holes are injected from the anode into the HTL, while electrons are injected from the cathode into the ETL. Holes migrate from the HTL towards the EML, where emitter molecules with high phosphorescent emission rates and a reduced HOMO-LUMO gap are blended to facilitate exciton generation in close proximity to the emitter molecules. The energy levels of the emitter are represented by dashed lines, and the layer thicknesses are provided in nanometers (nm). Architecture 2 (A2) mirrors A1 but incorporates additional hole and electron injection layers (depicted in yellow). Architecture 3 (A3) features two additional blocking layers flanking the EML to confine charge carriers to the EML.

electrodes' capacity to dissipate continuous amounts of energy, I utilize Miller-Abrahams rates [170, 171] for determining the charge injection rate:

$$\omega_{Xi} = \frac{\pi}{2\hbar k_{\mathrm{B}} T} |J_{Xi}|^2 \times \begin{cases} \exp\left(-\frac{\Delta E_{Xi}}{k_{\mathrm{B}} T}\right) & \text{, for } \Delta E_{Xi} > 0 \\ 1 & \text{else,} \end{cases} \tag{5.1}$$

where the temperature was $T = 300\,\mathrm{K}$ in all simulations. Here, J_{Xi} denotes the electronic coupling between the electrode $X$and the organic molecule i and is given by:

$$J_{Xi} = j_0^{\mathrm{el}} \cdot \exp\left(-2\frac{r_i}{\delta_0^{\mathrm{el}}}\right). \tag{5.2}$$

The prefactor j_0^{el} denotes the maximum coupling, which is then modulated by the distance-dependent exponential function, where δ_0^{el} denotes the characteristic decay length of the electrode wavefunction. The specific values utilized in this context can be referenced in Table 5.1.
The injection barrier for holes ($X = A$, for anode) is given by:

$$\Delta E_{\mathrm{A}i} = E_{\mathrm{A}}^{\mathrm{F}} - E_i^{\mathrm{H}} - e\phi_i^{\mathrm{S}} + e\phi_i^{\mathrm{D}} - eFr_i\,, \tag{5.3}$$

where $E_{\mathrm{A}}^{\mathrm{F}}$ represents the Fermi level of the anode, F signifies the electric field, and r_i denotes the distance between the target site i and the anode. The screening term $\phi_i^{\mathrm{S}} = e^2/(16\pi\epsilon_0\epsilon_r r_i)$ ensures the boundary condition of a constant potential at the electrodes, which is achieved using the method of image charges. The dynamic Coulomb potential ϕ_i^{D} incorporates all other charge carriers q_k and their image charges q_k' within the device:

$$\phi_i^{\mathrm{D}} = \frac{1}{4\pi\epsilon_0\epsilon_r} \sum_k \left(\frac{q_k}{r_{ik}} + \frac{q_k'}{r_{ik}'}\right), \tag{5.4}$$

where the dielectric constant ϵ_r was 4.0 for all layers. The dynamic electrostatic potential is computed by using the Ewald method[172].
The injection barrier for electrons at the cathode ($X = C$) is defined in a similar manner:

$$\Delta E_{\mathrm{C}i} = E_i^{\mathrm{L}} - E_{\mathrm{C}}^{\mathrm{F}} - e\phi_i^{\mathrm{S}} - e\phi_i^{\mathrm{D}} - eFr_i\,. \tag{5.5}$$

5.1.3 Charge transport

As discussed in earlier chapters, charge carrier transport is also modeled as hopping transport in this work. The hopping rate between sites i and j is calculated using the Marcus rate equation (3.77).
The energy difference ΔE_{ij} incorporates the dynamic Coulomb potential ϕ^D arising from charge-charge

interactions within the device and the applied electric field:

$$\Delta E_{ij} = \left(\varepsilon_j - e\Phi_j^{\mathrm{D}}\right) - \left(\varepsilon_i - e\Phi_i^{\mathrm{D}}\right) - eFr_{ij}\,, \tag{5.6}$$

for electrons and:

$$\Delta E_{ij} = \left(\varepsilon_j + e\Phi_j^{\mathrm{D}}\right) - \left(\varepsilon_i + e\Phi_i^{\mathrm{D}}\right) + eFr_{ij}\,, \tag{5.7}$$

for holes.
The electronic coupling J_{ij} is given by:

$$J_{ij} = j_0 \exp\left(-2\frac{r_{ij}}{\delta_0}\right). \tag{5.8}$$

The maximum coupling j_0 and decay length δ_0, along with all parameters pertinent to charge injection and charge transport, are listed in Table 5.1. It's noteworthy that for charge transfer processes, no distinction was made between emitter and host molecules. This differentiation becomes relevant solely for excitonic processes.

Table 5.1: Simulation parameters for charge injection and charge transport.

Parameters for energy landscape	Value
Anode Fermi-level	−5.4 eV
Cathode Fermi-level	−2.4 eV
Energetic disorder σ for all organic materials (HOMO and LUMO)	0.1 eV
Mean HOMO in HTL and ETL	−5.8 eV
Mean LUMO in HTL and ETL	−2.0 eV
Mean HOMO in EML (host)	−5.8 eV
Mean LUMO in EML (host)	−2.0 eV
Mean HOMO in EML (emitter)	−5.5 eV
Mean LUMO in EML (emitter)	−2.3 eV
Mean HOMO in HIL	−5.6 eV
Mean LUMO in HIL	−2.0 eV
Mean HOMO in EIL	−5.8 eV
Mean LUMO in EIL	−2.2 eV
Mean HOMO in HBL	−6.3 eV
Mean LUMO in HBL	−2.0 eV
Mean HOMO in EBL	−5.8 eV
Mean LUMO in EBL	−1.5 eV
Parameters for couplings	
Max coupling electrode-organic j_0^{el}	0.001 eV
Decay length for coupling electrode-organic δ_0^{el}	0.3 nm
Max coupling organic-organic j_0	0.001 eV
Decay length for coupling organic-organic δ_0	0.1 nm
Reorganization energy λ used in Marcus rates for charge transfer	0.2 eV

5.1.4 Excitonic processes

In this study, excitons are modeled as either the first excited singlet (S1) or the first excited triplet states (T1) of the corresponding molecule. The excitation energies E_i^X associated with molecule i are given by:

$$E_i^X = \begin{cases} E_i^{\mathrm{L}} - E_i^{\mathrm{H}} - E^{\mathrm{B}}, \text{ for singlets } X = \mathrm{S1} \\ E_i^{\mathrm{L}} - E_i^{\mathrm{H}} - E^{\mathrm{B}} - E^{\mathrm{ST}}, \text{ for triplets } X = \mathrm{T1} \end{cases} \tag{5.9}$$

where E^{B} is the exciton binding-energy and E^{ST} the singlet-triplet gap.

Exciton recombination and charge separation

If there exists an exciton positioned at a specific site i, it has the potential to undergo charge separation via two distinct pathways: hole separation, where the hole transfers to a neighboring site while leaving the electron behind at site i, or electron separation, which involves the electron relocating to a neighboring site instead. In our model, I characterize separation as a charge transfer process, with the energy barrier for hole separation determined by:

$$\Delta E_{ij} = E_i^{\mathrm{L}} - E_j^{\mathrm{H}} - E_i^X - \frac{e^2}{4\pi\epsilon_0\epsilon_r}\frac{1}{r_{ij}} + e(\Phi_j - \Phi_i)\,, \tag{5.10}$$

where $\Phi_{i(j)}$ represents the total electrostatic potential, incorporating the dynamic term and all other previously introduced terms at site i (j). Additionally, the Coulomb potential between the charged sites i and j is explicitly considered.
The energy barrier for the electron separation process is given by:

$$\Delta E_{ij} = E_j^{\mathrm{L}} - E_i^{\mathrm{H}} - E_i^X - \frac{e^2}{4\pi\epsilon_0\epsilon_r}\frac{1}{r_{ij}} + e(\Phi_i - \Phi_j)\,. \tag{5.11}$$

Exciton transfer

As previously discussed in Chapter 3, excitons possess the ability to move through two mechanisms: Dexter transfer [173, 174], where the bound electron-hole pair jumps to an adjacent site through simultaneous charge transfer, and Förster transfer [175, 176], where energy is transferred via a virtual photon. Both processes are incorporated into our kinetic Monte Carlo (kMC) model.
Since Dexter transfer involves the simultaneous transfer of the electron and hole constituting the exciton, Marcus rate expression (equation (3.77)) is used to compute Dexter transfer rates. However, there are certain adjustments: I utilize the excitation energies E_i^{X} and E_j^{X} (equation (5.9)) to determine the energy difference required for the exponential function in Marcus rates, and consider Dexter couplings J_{ij}^{Dexter} that are one order of magnitude lower compared to couplings used for charge transfer.
In this model, Marcus theory is also used to compute the Förster transfer rates, incorporating the long-

range coupling that is specific to Förster transfer:

$$J_{ij}^{\text{Förster}} = \kappa \frac{|\boldsymbol{d}_i||\boldsymbol{d}_j|}{r_{ij}^3} \,, \tag{5.12}$$

where $\boldsymbol{d}_i$ denotes the transition dipole moment, and the factor κ accounts for the relative orientation of the transition dipole moments of sites i and j. The use of Marcus-transfer rates is justified by the results presented by Stehr et al. [112], wherein they showcased the ability of Marcus theory to qualitatively predict exciton diffusion coefficients in diverse organic materials.
The norm of the transition dipole moment is computed based on the parameter-settings by:

$$|\boldsymbol{d}_i| = \sqrt{\frac{3k}{4\tau_{\text{rad}}\alpha^3 (E_i^X)^3}} \,, \tag{5.13}$$

where $k = 2.42 \times 10^{-17}$ s, τ_{rad} is the radiative life which is the inverse radiative decay rate, $\alpha = 1/137$ is the fine-structure constant and E_i^X is the excitation energy of site i, which is defined in equation (5.9). To obtain the vectorial transition-dipole moment, a randomly orientated unit-vector $\vec{n}_i$ for each site is generated. The vectorial transition-dipole moment is then given by:

$$\vec{d}_i = |\vec{d}_i|\vec{n}_i \,. \tag{5.14}$$

The orientation factor κ in the Förster-coupling (5.12) is given by:

$$\kappa = \vec{n}_i \cdot \vec{n}_j - 3\left(\frac{\vec{r}_{ij}}{r_{ij}} \cdot \vec{n}_i\right)\left(\frac{\vec{r}_{ij}}{r_{ij}} \cdot \vec{n}_j\right) \,, \tag{5.15}$$

where $\vec{r}_{ij}$ is the displacement vector between site i and j and r_{ij} is its length.

Excitonic quenching

Excitons suffer from quenching through various processes such as triplet-triplet annihilation (TTA) or triplet-polaron quenching (TPQ) [54, 177, 47, 56, 51, 58]. In this study, I focus on modeling the rates of TTA and TPQ using a heuristic formula for quenching of type Q = TTA or TPQ:

$$\omega_{ij}^Q = \begin{cases} \omega_{\text{max}}^Q, \text{ if } r_{ij} = a \\ \omega_{\text{max}}^Q \frac{a^6}{r_{ij}^6}, \text{ else} \end{cases} \,. \tag{5.16}$$

As these quenching processes are based on Förster mechanisms, the distance dependence of the quenching rates follows the same law as that of Förster-based exciton transfer ($\propto r_{ij}^{-6}$). The maximum rate for the quenching process Q is denoted by ω_{max}^Q, and a represents the lattice constant used to maintain consistent units. The values employed for the quenching, along with all other relevant rates for excitonics, are presented in Table 5.2 and have been adapted from quantum chemical calculations outlined in the

Table 5.2: Additional parameters for the excitonics.

Decay and quenching rates	non-emitters	emitters
ISC-rate	$1 \times 10^3\,\mathrm{s}^{-1}$	$1 \times 10^{14}\,\mathrm{s}^{-1}$
RISC-rate	$1 \times 10^2\,\mathrm{s}^{-1}$	$1 \times 10^6\,\mathrm{s}^{-1}$
thermal decay rate	$1 \times 10^5\,\mathrm{s}^{-1}$	$1 \times 10^5\,\mathrm{s}^{-1}$
Exciton reorganization energy	0.3 eV	0.3 eV
Excitonic binding energy	0.8 eV	0.8 eV
Singlet-Triplet gap	0.3 eV	0.3 eV
Radiative decay rate S1	$1 \times 10^8\,\mathrm{s}^{-1}$	$1 \times 10^8\,\mathrm{s}^{-1}$
Radiative decay rate T1	$1 \times 10^1\,\mathrm{s}^{-1}$	$1 \times 10^6\,\mathrm{s}^{-1}$
Max TTA rate	$1 \times 10^6\,\mathrm{s}^{-1}$	$1 \times 10^{11}\,\mathrm{s}^{-1}$
Max TPQ rate	$1 \times 10^6\,\mathrm{s}^{-1}$	$1 \times 10^{11}\,\mathrm{s}^{-1}$
Parameters for Dexter transfer integrals		
Max Dexter coupling j_0^{Dexter}	0.0001 eV	0.0001 eV
Decay length for Dexter coupling δ_0^{Dexter}	0.1 nm	0.1 nm

work by Symalla et al. [54].

5.2 Simulation details

To ensure the reliability of the results, I conducted simulations for 20 replicas of each device, with each replica undergoing 50 million kMC steps. Properties such as current or particle densities were then averaged over all replicas. The simulated devices were modeled with a cross section of $20 \times 20\ \mathrm{nm}^2$. The built-in electric field of the devices is determined by the equation:

$$F_{\mathrm{BI}} = \frac{E_{\mathrm{C}}^{\mathrm{F}} - E_{\mathrm{A}}^{\mathrm{F}}}{e(1.6\,\mathrm{nm} + L_{\mathrm{Device}})}, \tag{5.17}$$

where e represents the elementary charge. The distance between the anode and the organic material is 0.8 nm for both the anode and cathode, accounting for the surface roughness of the amorphous organic layer, with typical molecules having a volume of approximately $1\,\mathrm{nm}^3$. The total thickness of all organic layers is denoted by L_{Device}.

To apply electric fields that exceed the built-in field, I use the following scheme:

$$F_{\mathrm{applied}} = F_{\mathrm{BI}} + F_x, \tag{5.18}$$

where F_x takes on values from $0.01\,\mathrm{Vnm}^{-1}$ to $0.06\,\mathrm{Vnm}^{-1}$ unless otherwise specified.
In Chapter 2, I elaborated on the significance of the internal quantum efficiency (IQE) for the overall efficiency of OLED devices. In the model employed in this study, the computation of the outcoupling

efficiency of photons is not implemented. Therefore, our focus is on studying the IQE, defined as:

$$\mathrm{IQE} = \frac{N_{\mathrm{rad}}}{N_{\mathrm{X}} - N_{\mathrm{CS}}}\,, \tag{5.19}$$

where N_{rad} denotes the number of emitted photons, N_{X} represents the total number of excitons, and N_{CS} represents the number of charge separations. Additional information regarding the rates utilized in the kinetic Monte Carlo (kMC) simulations can be found in the supplementary information.

5.3 IV and IQE characteristics

I conducted simulations of charge and exciton dynamics in the three architectures presented in Figure 5.1. Our objective was to compare the IQE of the three devices and examine the charge, exciton, and quenching profiles along the transport axis of the devices. This visualization allowed us to observe the impact of architectural differences on the carrier and exciton dynamics.

As described in the methodology section, I performed simulations by applying electric fields that counterbalance the built-in field F_{BI} of each device, ensuring that the effective field experienced by the charge carriers is equal in all devices. Figure 5.2 (**A**) displays the current-voltage characteristics resulting from the simulations of all device architectures (A1-A3) with an emitter concentration of 15%. It is noteworthy that despite the identical effective fields experienced by the charge carriers, there is a significant difference in the currents between A2 or A3 and A1, varying by approximately one order of magnitude. The reason for this difference is that A2 and A3 contain a higher number of layers than A1, resulting in a higher effective resistance that requires a larger electric field (or voltage) to generate the same currents. Additionally, the presence of blocking layers in A3 further reduces the achieved current compared to A2. The impact of the difference in achieved current among the devices is reflected in their respective IQE. As the achieved currents decrease due to increased effective resistance, the roll-off effect is delayed, leading to higher IQEs at the same electric field experienced by the charge carriers. In Figure 5.2 (**B**), the IQEs of the devices are presented, with A2 and A3 exhibiting significantly larger IQEs at low currents. Conversely, A1 already achieves a current of approximately $10^3\,\mathrm{mA/cm^2}$ at the smallest electric field. Indeed, at high electric fields, the achieved currents of A2 and A3 become comparable to that of A1, and as a result, the roll-off effect becomes prominent, leading to a significant drop in IQE that is comparable to A1.

It is evident that while the implementation of injection and blocking layers leads to a significant improvement in the IQE at low currents, which is in line with experimental findings [168, 178], all of the device architectures are still susceptible to roll-off, resulting in very small high-current IQEs.

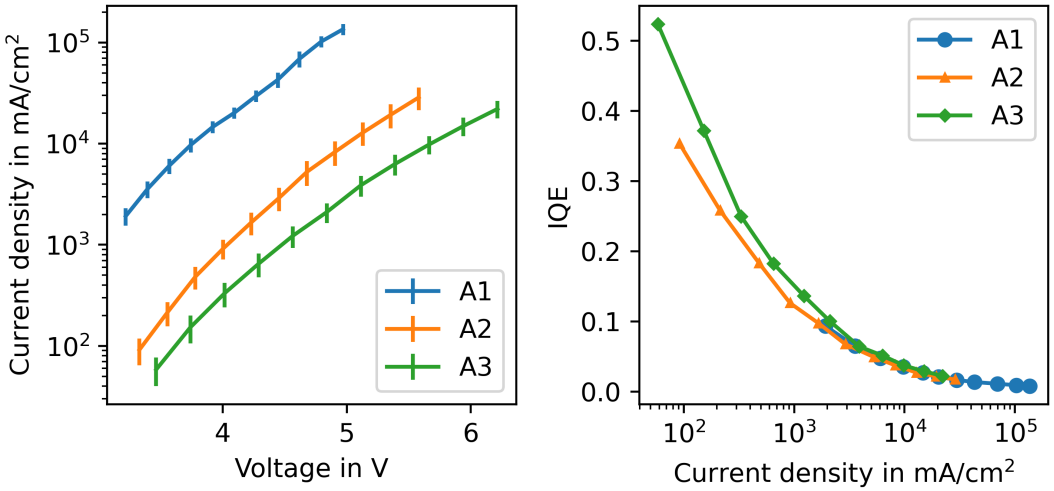

Figure 5.2: IV- and IQE-curves of all three device architectures. Panel (**A**) shows the IV curves of three devices, with A1 (blue), A2 (orange), and A3 (green). The thinnest device, A1, shows the highest current density, followed by A2 and then A3, which is the thickest. The increase in thickness results in higher resistance, leading to lower currents. The emitter concentration in all three devices was 15%. Panel (**B**) shows that A3 exhibits the highest IQE at low current densities ($< 10^3$ mA/cm^2). However, all three IQEs decrease to small values at high current densities ($> 10^3$ mA/cm^2), indicating a common roll-off. Thus, the modifications made to the device architecture were inadequate to prevent the high-current roll-off.

5.4 Charge and exciton profiles

Gaining insights into how the integrated layers influence the distribution of carriers and excitons throughout the system is critical for identifying performance bottlenecks and gaining a deeper understanding of device physics. Figure 5.3 depicts the distribution of particles, such as charges and excitons, throughout the devices, represented by their profiles along the transport axis. Specifically, the charge carrier profile is determined by averaging the sum of all holes (or electrons) across the device's cross-section at a given position along the transport axis over the simulation time. A value of 1 signifies that there is on average one hole (or electron) in the corresponding cross-sectional position.

Upon analyzing the charge profile of A1 in Figure 5.3 (**A**), it becomes evident that the symmetry of A1 in terms of layer arrangement and energetic landscape is mirrored in the distribution of holes and electrons. The concentration of holes is observed to be high at the interface between the anode and the organic layer, decreasing towards the emissive layer and increasing again. A similar trend is observed for electrons, which are concentrated near the cathode-organic interface. Maintaining charge balance is essential for exciton generation, and A1 demonstrates good charge balance within the emissive layer, as reflected in the generation of excitons solely within that region (Figure 5.3 (**B**)).

The simulation results show that reducing charge balance, particularly in the transport layers and near the electrode interfaces, leads to a negligible number of excitons being generated over time. Figure 5.3 (**C**) depicts the proportion of excitons per layer, quenched by TTA or TPQ or charge separation processes leading an exciton to an unbound electron-hole pair. All exciton quenching events and charge separation take place in the EML, indicating that the generated excitons do not leave the EML through diffusion processes.

In Figure 5.3 (**D**), the addition of hole- and electron injection layers (A2) slightly increased the charge balance in the EML, but a significant amount of excitons was generated at the interface between the injection and transport layers. This is due to a smaller gap between HOMO and LUMO energies in the injection layers, which fosters exciton generation (Figure 5.3(**E**)). However, this effect is undesired because most of these excitons are unlikely to diffuse to the EML for radiative decay.

Figure 5.3 (**F**) shows that a large fraction of excitons undergo TTA and TPQ processes in the EML, while a significant fraction is quenched at the interface between the injection and transport layers. To prevent exciton generation at these positions, the charge balance outside the EML must be minimized by adding a hole or electron blocking layer on the left or right side of the EML.

Figure 5.3 (**G**) shows the charge profile of A3 with the desired absent charge balance outside the EML, resulting in exciton generation only inside the EML as seen in figure 5.3 (**H**). However, the existence of blocking layers does not completely eliminate all bottlenecks. It results in the accumulation of excess holes at the interface between the emissive layer (EML) and the hole-blocking layer (HBL), as well as excess electrons at the interface between the EML and the electron-blocking layer (EBL).

Furthermore, the concentration of charge carriers with opposite sign is higher at these interfaces compared to the central region of the EML. As a consequence, the large concentration of charge carriers contributes to a greater number of charge recombination and increases the occurrence of TPQ events (Figure 5.3 (**I**)).

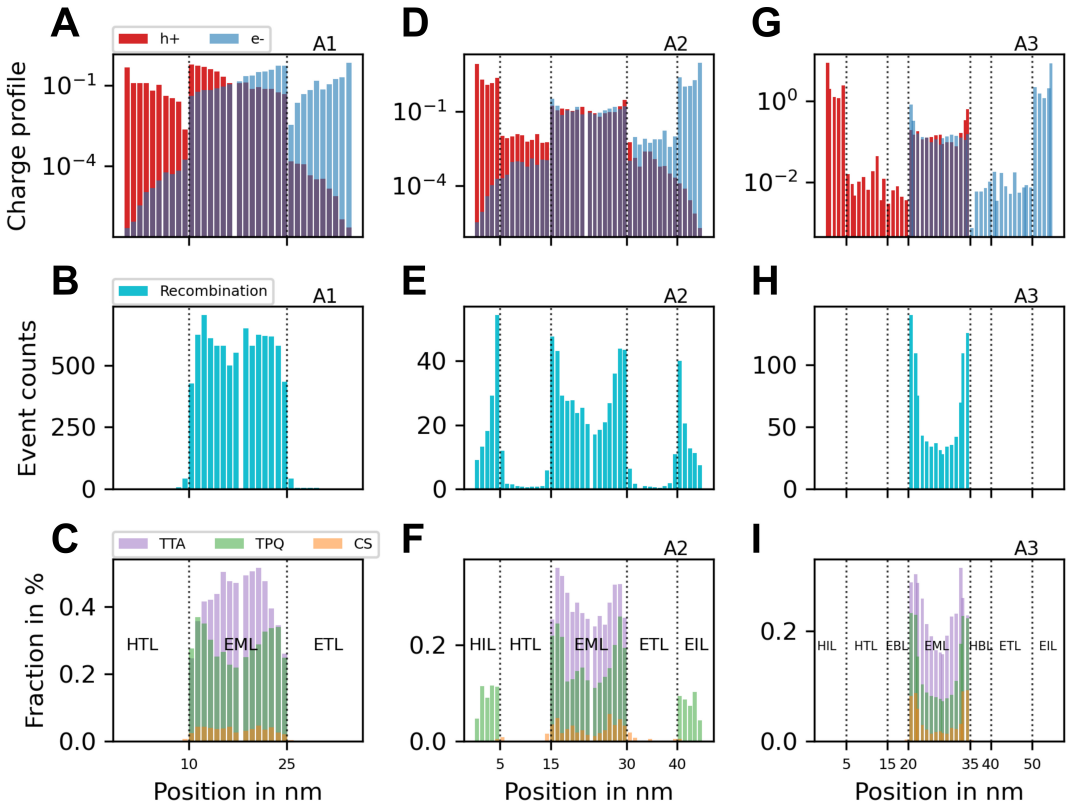

Figure 5.3: The particle profiles of devices with architectures A1, A2, and A3 are shown in the first, second, and third columns, respectively. I simulated one device for each architecture with an EML thickness of 15 nm and an emitter concentration of 15%, with the remaining layers as depicted in Figure 5.1. Panel **A** displays the average number of electrons and holes per cross-sectional layer over the simulation time. I observe that the charge balance within the EML is not ideal, particularly at the interface to the transport layers where I have excess charges with an opposite sign.In panel **B**, I observe that exciton generation only takes place inside the EML, despite non-zero charge balance throughout the entire transport axis. This is due to the relatively large HOMO-LUMO gap in the transport layers that suppresses charge recombination.Panel **C** shows that in addition to TTA processes throughout the entire EML, excess charges at the interface to the transport layers lead to an increased number of TPQ processes, which negatively impacts the IQE.In panel **D**, I add electron- and hole-injection layers (architecture A2) to slightly enhance the charge balance within the EML, but this causes exciton generation in the injection layers (panel **E**). This is due to the smaller HOMO-LUMO gap, despite the small but non-zero charge balance in the injection layers. As shown in panel **F**, this leads to many TPQ events within the injection layers because of the combination of high exciton and charge density there.To prevent charges from recombining outside the EML, I add electron- and hole-blocking layers as depicted in Figure 5.1. As shown in panel **G**, this causes the charge balance to vanish to the left and right of the EML. As expected, exciton generation only occurs within the EML (panel **H**). Furthermore, I observe a reduction in quenching throughout the device compared to panel **F** (panel **I**).

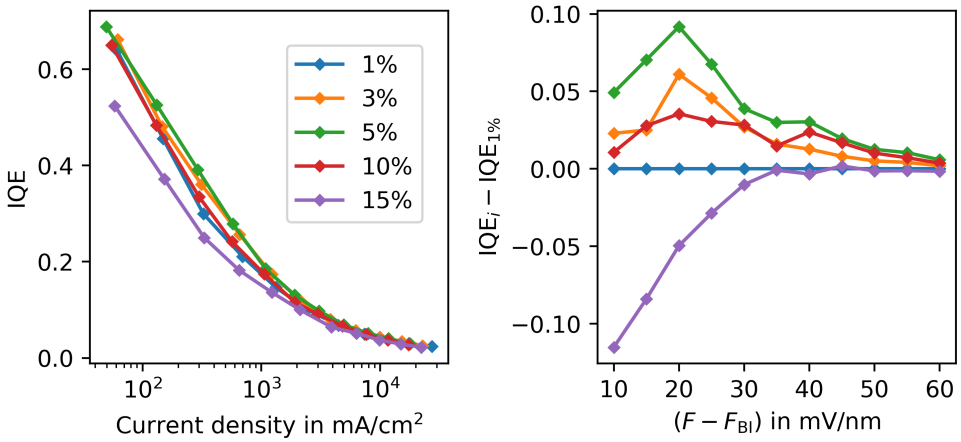

Figure 5.4: The IQE versus current-density relationship for five devices with architecture A3 is presented. All devices have an EML thickness of 15 nm, but vary in emitter concentration from 1% to 15%. The optimal emitter concentration for low current densities appears to be around 5%, with a significant improvement in IQE compared to higher concentrations (15%). However, all devices suffer from significant roll-off, as evidenced by the sharp drop in IQE for high current densities. **B** Increasing the current-densities (corresponding to high electric fields) reduces the positive effect of optimizing the emitter concentration. This suggests that emitter concentration optimization alone can only improve device performance to a limited extent, but cannot overcome the drastic reduction in IQE caused by roll-off.

5.5 Dependency on emitter concentration

Figures 5.3 (**C**), (**F**), and (**I**) provide insights into the particle dynamics resulting from the addition of injection and blocking layers. However, the high count of TTA and TPQ events, particularly at the interfaces with the blocking layers, remain a bottleneck. One potential strategy to address this issue is to decrease the exciton density in the EML by reducing the emitter concentration[38]. To explore this, I simulated A3 with varying emitter concentrations while keeping the rest of the device unchanged. Figure 5.4 (**A**) presents the obtained IQE for A3 with emitter concentrations ranging from 1% to 15%. I observed an improvement for emitter concentrations below 15% for small current densities, but varying the emitter density could not prevent the roll-off effect, leading to low IQEs at large current densities. This is further illustrated in Figure 5.4 (**B**), where I plotted the difference of the IQEs at all applied electric fields relative to the 1% device IQE. I can clearly observe that, particularly for small fields (corresponding to small currents), the 15% device has up to 0.10 lower IQE. The device with 5% emitter concentration exhibited the best performance. Reineke and Baldo[179] reported that devices with emitter concentrations ranging from 1% to 10% exhibit high quantum efficiency, which our results support.

5.6 Dependency on EML thickness

Previous studies have reported that the efficiency of OLED devices is affected by the thickness of the emissive layer (EML), and thicker EMLs lead to more efficient devices [180, 181]. To verify this using our simulation model, I varied the EML thickness of architecture 3 with an emitter concentration of 15%. In Figure 5.5 (A), I present the IQE for architecture 3 with EML thicknesses ranging from 10 to 40 nm. Our simulations demonstrate that thicker EMLs result in higher IQE at low current densities, as observed in previous studies. For example, comparing the IQE of the 10 nm and 40 nm devices, I observe an improvement of about 0.3 (Figure 5.5 (B)). Additionally, I find a significant improvement in the IQE for thicker emissive layers at high effective fields, indicating that increasing EML thickness not only improves the low-field IQE but also reduces roll-off, leading to more efficient devices across all operating regimes. To understand how EML thickness affects the quenching processes, similar to Figure 5.3 (I), I analyzed the ratio of triplet excitons undergoing TPQ or TTA quenching events. Figures 5.6 (A)-(C) illustrate the quenching profiles of devices with architecture 3 and EML thicknesses of 10, 25, and 40 nm, respectively. All simulations were performed with an effective field of $F - F_{\mathrm{BI}} = 60\,\mathrm{mV/nm}$, leading to relatively high current densities (see Figure 5.5).

These results reveal that the fraction of TPQ and TTA events decreases with increasing EML thickness, leading to an increase in the IQE, as demonstrated in Figure 5.6. This demonstrates the ability of computational studies to provide insights into the relationship between modifications to device design that affect macroscopic properties such as IQE or emission, and microscopic properties such as particle dynamics. In the final step of this study, I utilized this model to optimize OLED performance by varying the layer thickness and emitter concentrations. I screened a total of 225 devices with architecture 3, where each device had a different EML (Emissive Layer) thickness and emitter concentration. Figure 5.7 illustrates that the Internal Quantum Efficiency (IQE) demonstrates a significant increasing trend as the EML thickness is increased while maintaining a constant emitter concentration at 5-6

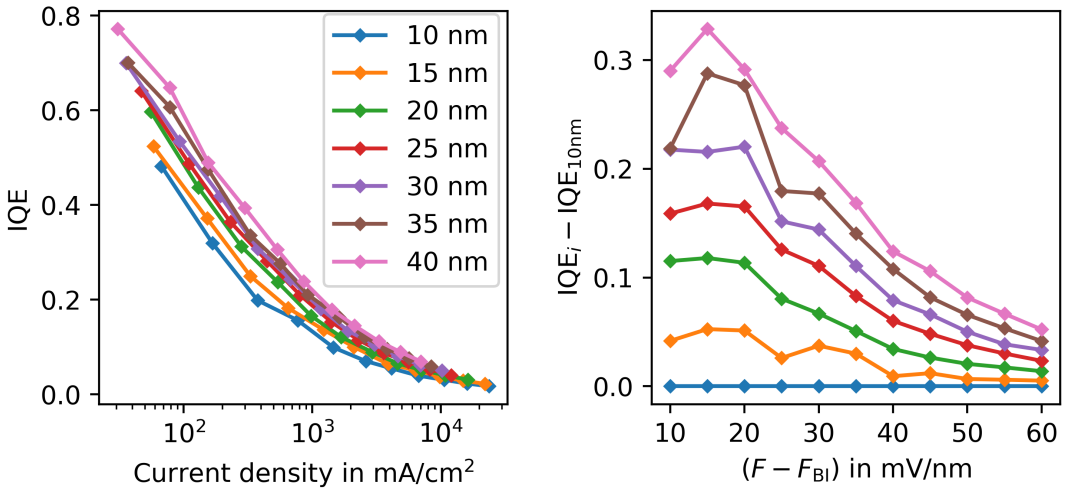

Figure 5.5: IQE as a function of current-density for devices with architecture A3. This time, the emitter concentration is fixed at 15% for all devices, while the EML thickness varies from 10 nm to 40 nm. As the EML thickness increases, there is a significant improvement in IQE at low current-densities. However, roll-off still persists for large current-densities, but not as severe as observed in figure 5.4. **B** To investigate the impact of varying EML thickness on the IQE at high fields (i.e., high current-densities), I plot the change in IQE with respect to the device with 10 nm EML thickness. Interestingly, I observe that the device with 40 nm EML thickness has approximately 8% higher IQE at 60 mV/nm compared to the thinnest device. Unlike optimizing emitter concentration, increasing the EML thickness has a positive effect on high-field IQE.

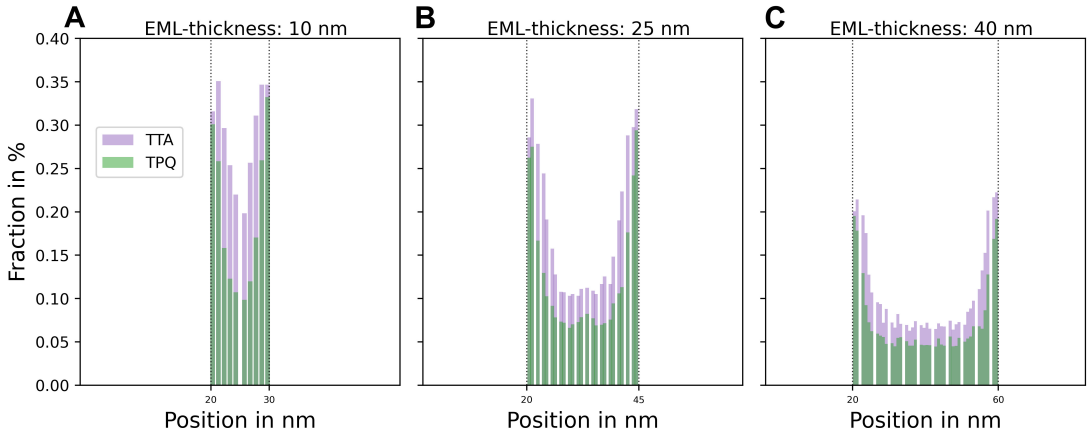

Figure 5.6: Quenching profiles of devices with architecture A3. Shown are devices with EML thicknesses of 10 nm (**A**), 25 nm (**B**), and 40 nm (**C**). It is observed that as the EML thickness increases, there is a decrease in the fraction of excitons generated per cross-sectional position that undergo TTA or TPQ. This decrease in quenching explains the increase in IQE for devices with higher EML thicknesses.

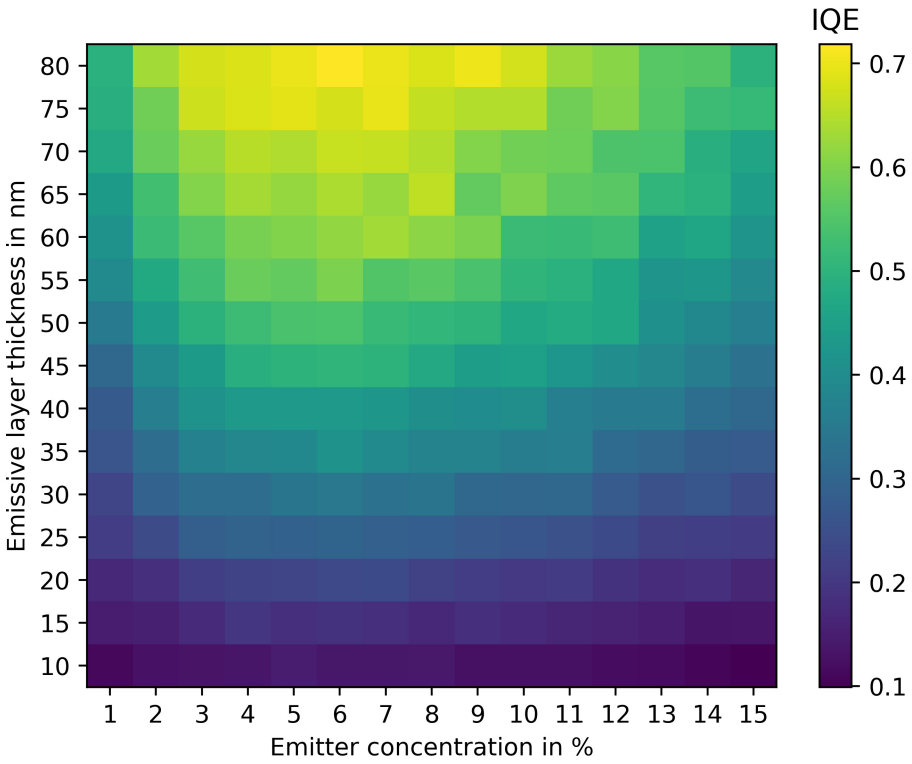

Figure 5.7: IQE of 225 devices with architecture A3. The simulation was conducted using an electric field of 30 mV/nm above the built-in field. The simulation results showed a consistent trend of increasing IQE with increasing EML thickness. Additionally, the optimal emitter concentration was found to be in the range of 5-6%, which is consistent with previous findings.

5.7 Conclusion

In this study, parametric KMC simulations were employed to investigate three distinct OLED architectures: A1, A2, and A3 (see Figure 5.1), all featuring a phosphorescent emitter blended with the host material in the Emissive Layer (EML) [182]. This analysis unveiled significant differences in device performance regarding Internal Quantum Efficiency (IQE) and current-density behavior, as depicted in Figure 5.2. By use particle profile plots (Figure 5.3), I identified key bottlenecks unique to each architecture. Specifically, architecture A1 exhibited non-ideal charge balance within the EML, leading to enhanced Triplet-Polaron Quenching (TPQ), particularly at the interface with the transport layers, and a high occurrence of Triplet-Triplet Annihilation (TTA) processes within the EML (Figure 5.3C). To mitigate this issue, I introduced charge injection layers between the electrodes and transport layers, improving charge balance within the EML. However, this approach led to undesired exciton generation in the injection layers due to the narrow HOMO-LUMO gap (Figure 5.3E and F). Although the addition of charge blocking layers enhanced device efficiency, the roll-off effect persisted.
For the multilayer architecture (A3), further optimization of IQE was achieved by varying the emitter concentration and EML thickness (Figures 5.4 and 5.5). Simulation results indicated that the highest low-current IQEs were achieved with emitter concentrations around 5%, consistent with previously reported values [38, 179]. Nonetheless, the device still experienced roll-off due to TTA and TPQ processes [52]. Increasing the EML thickness further improved efficiency and mitigated roll-off at current densities around $1 \times 10^4\,\mathrm{mA/cm^2}$.
This computational approach demonstrates the utility of heuristic models for analyzing device architectures and identifying efficiency-affecting parameters. This method efficiently pinpointed performance bottlenecks specific to each architecture, tasks that would be laborious and costly to accomplish experimentally. I believe that this computational framework can facilitate the rational design of efficient OLEDs by offering flexibility in adjusting material and device parameters to achieve high IQE and preemptively identifying performance limitations. Combining this heuristic approach with more realistic models based on ab-initio data holds promise for enhanced accuracy, although at higher computational costs. Therefore, heuristic models serve as valuable tools for identifying promising design regions for more detailed investigations.

6 Modelling device degradation

Over the last few decades, many obstacles related to OLED devices, such as poor efficiency, have been effectively addressed. As shown in the previous chapter, a methodical improvement of device structures and materials can help alleviate problems like roll-off effects. Nonetheless, a continuous issue in OLEDs persists: device longevity. Despite notable enhancements in lifespan for display uses where lower brightness levels are sufficient [183, 184], achieving sufficient lifespans for applications requiring high initial brightness remains a challenge for commercial adoption [185].

In general, electroluminescent devices decline in luminance over time. In a review by Aziz and Popovic [186], three specific types of degradation were defined: Formation of dark spots, primarily at electrodes, leading to the creation of non-emissive regions and subsequently reducing the emissive area of the device [187]. The second type of degradation involves catastrophic failure, wherein electrical shorts cause a sudden and drastic reduction in luminance, often correlated with significant leakage currents [188]. The third type is referred to as intrinsic degradation, characterized by a gradual decline in luminance over extended periods of operation.

Proper device encapsulation and meticulous control of production conditions during manufacturing can effectively manage the first two types. However, comprehending and addressing the third type necessitates deeper exploration. In contrast to catastrophic failure and dark-spot formation, which are mainly influenced by external factors and involve observable mechanistic changes in the device, intrinsic degradation stems from microscopic processes occurring within the organic material during operation.

The lifetime of OLED devices presents a significant issue with blue phosphorescent emitters, which experience a 50% reduction in initial luminance after several thousand hours, while green phosphores-

cent devices can operate for up to one million hours before reaching the 50% threshold [189]. Previous studies indicated that defects develop within the device, specifically in the EML, as a result of excitonic quenching mechanisms like TPQ or TTA. These defects contribute to the formation of carrier traps and non-emissive centers. Computational investigations into these processes at the device level and their impact on device lifetimes were carried out in the late 2000s by Giebink et al. [190, 191]. The primary degradation process was reported to be TPQ. However, the early computational degradation studies employed one-dimensional Drift-Diffusion Models (DDM) that were unable to capture the percolative nature of charge transport [192] (see Chapter 3). In 2014, Coehoorn and colleagues demonstrated OLED lifetime simulations using a 3D KMC model. They argued that TPQ is the primary cause of defects leading to charge trapping and non-emissive exciton quenching [57, 65]. However, simulating lifetimes of commercially available OLEDs was not feasible with the methods described above, as simulating hundreds of thousands of hours of operation time using KMC is not achievable. It is challenging to simulate OLEDs in the timescale of device lifetimes, which can extend to several hundred thousand hours or more of operational time. Hauenstein et al. [193] attempted to address this issue by introducing a power law that relates lifetime to current density. Despite this approach, they were only able to reach timescales on the order of thousands of hours.

In this chapter, I propose an alternative approach to address the timescale limitation in kinetic Monte Carlo (KMC). I developed a protocol to accelerate the KMC simulation time to match the scale of these significant device lifetimes.

While this approach effectively tackled the timescale problem for one specific device, it turned out to be impractical for a broader range of device architectures. In this study, merely increasing the emitter concentration without adjusting other system parameters made this approach ineffective. The number of KMC steps needed to observe significant effects of gradually degrading molecules on device performance became unmanageably high and impractical.

The following sections are organized as follows: First, I will outline the used degradation model and its implementation within ourKMC framework. Second, I will discuss how luminance is defined in the context of this work and detail the method for measuring luminance loss. Subsequently, I will introduce the developed timescale acceleration technique, which is then applied to investigate luminance loss in a parametric OLED model (see Figure 6.1). Finally, I will discuss additional methodological improvements that, when combined with the timescale acceleration method, serve as a valuable tool for computational lifetime studies of more complex OLED architectures.

6.1 Degradation model

Inspired by a study conducted by Wang et al., excitonic quenching events play a pivotal role in the degradation investigations presented here. The premise is that, owing to either exciton-exciton or exciton-polaron quenching, molecules targeted by such quenching events, undergo destruction[55, 54]. The exciton-exciton-based quenching events include TTA, triplet-singlet annihilation (TSA), SSA, and STA. In these scenarios, the excess energy of one exciton further excites the exciton on the target

molecule, thereby energetically enabling bond-breaking reaction pathways. In the case of exciton-polaron quenching, there exist singlet-polaron quenching (SPQ) and TPQ processes. Molecules targeted by the polaronic quenching events are destroyed due to similar arguments as those for the exciton-exciton based quenching events. I will distinguish between two main types of degradation in this study: (i) degradation of host molecules within the EML, and (ii) degradation of emitter molecules. In the degradation simulations, I model the destruction of host or emitter molecules over time, depending on the specific type being studied. Initially, all molecules are intact, but as the simulation progresses, more molecules are destroyed, leading to a gradual degradation effect that mimics real-world scenarios.
In this study, each of these mentioned quenching-processes is considered as a degradation trigger, leading to the immediate destruction of the targeted molecule. Since I am employing a cubic lattice toy model for the simulations, when I refer to "destroying" a molecule, I mean setting the electronic couplings of the site representing that molecule to its neighboring sites, as well as setting its fluorescence and phosphorescence rates to zero. Essentially, this prevents charge transport between the destroyed site and its environment, and the molecule can no longer emit photons. In reality, the actual chemical reactions involved may be much more complex, and it is recommended to use quantum mechanical reaction path studies for a more detailed understanding. Nonetheless, the toy model used here still provides valuable insights into the degradation effects on a device scale. The simulated device is depicted in Figure 6.1. In real devices, the probability of individual molecules being destroyed is exceedingly low, requiring billions or even hundreds of billions of such quenching events to target a single molecule. This vast number of necessary events renders it computationally infeasible to simulate device degradation when a significant fraction of molecules must be destroyed to observe any effect. To address this challenge in my simulation approach, molecules are promptly destroyed upon the first occurrence of the event.
However, this leads to simulated device lifetimes that are not comparable to realistic timescales, making the method uninteresting for practical device engineering purposes. Below, I will describe how I address and resolve this limitation.
By comparing the luminance loss curves for host-only and emitter-only degradation modes in a specific device architecture, it becomes possible to identify whether the hosts or emitters are the limiting factor affecting the performance of that particular architecture using these specific materials.

To further elucidate both degradation modes, I visually represent the processes that lead to the destruction of molecular sites at a microscopic level in Figure 6.2. The figure displays a snippet of the cubic lattice in a specific system state, featuring excitons and charge carriers (polarons). In both modes, events of host- and exciton-only quenching, as described earlier, result in the immediate destruction of the targeted site, depicted by the quenching interaction indicated by the red wiggly line. With increasing operation time, a larger fraction of molecular sites undergo destruction, ultimately leading to a reduction in device performance and luminance. The application of the KMC method to model OLED devices has been previously discussed in Chapter 3 and demonstrated in Chapter 5. In this chapter, I will introduce an adapted version of the method. The key difference here is that the molecules constituting the organic material can undergo degradation, meaning that the number of intact molecules in this study is not constant and changes over the course of the simulation.

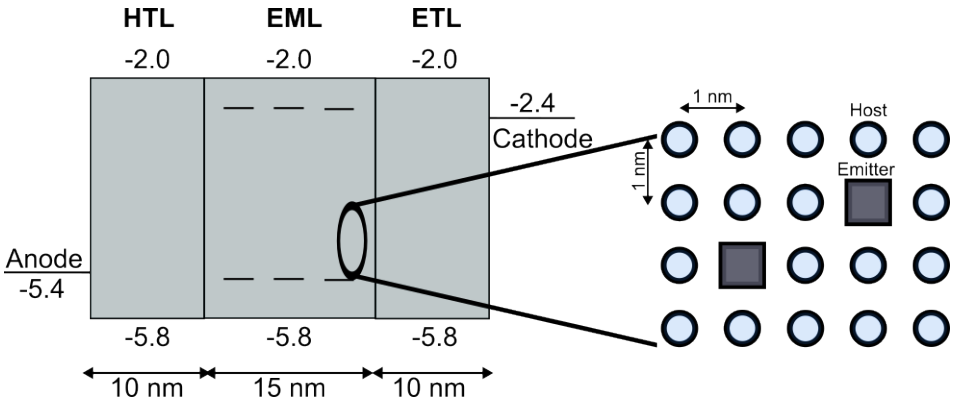

Figure 6.1: Device for degradation simulations. The device architecture utilized in this study precisely mirrors architecture 1 examined in the preceding chapter, as illustrated in Figure 5.1. Specifically, on the right-hand side, I aim to emphasize the microscopic structure of the emissive layer. Host molecules are represented by circles, while emitter molecules are depicted by squares. In this particular instance, the emitter concentration was 1%.

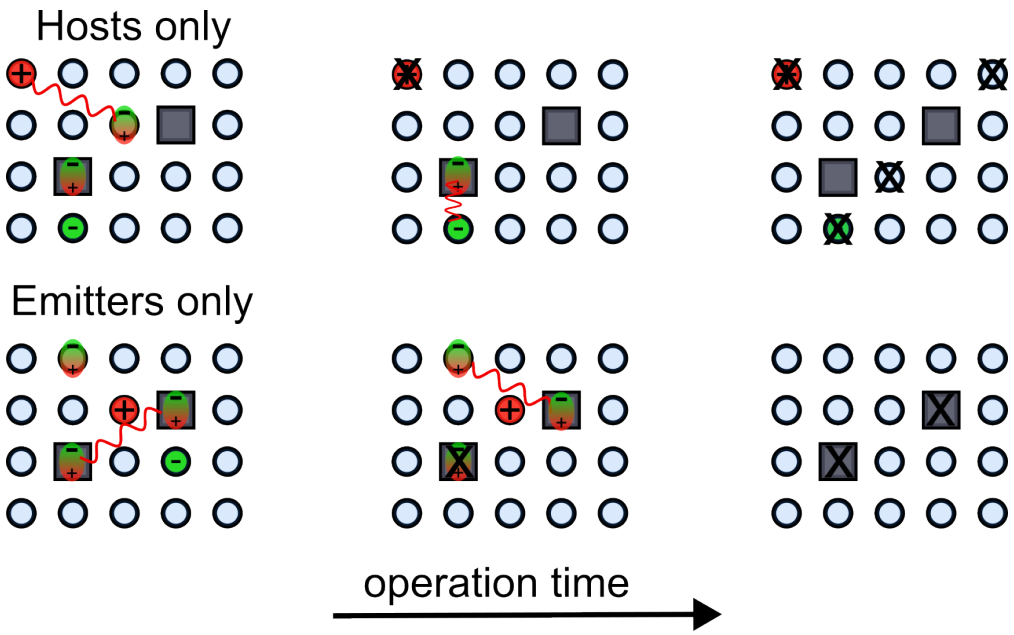

Figure 6.2: Degradation mechanism. The fundamental degradation mechanism and the two degradation modes, namely hosts-only and emitters-only, are illustrated here. The progression of operation time is depicted from left to right. Holes are represented by red circles, while electrons are shown in green. Excitons are depicted as red and green ellipses, representing dipoles. The red wiggly lines indicate long-range Förster transfer of excitons. In the hosts-only mode (top), the emitters remain intact while the host molecules are destroyed upon exciton-exciton or exciton-polaron quenching. Conversely, in the case of emitters-only mode(bottom), the host molecules remain intact while the emitter molecules are subject to destruction. The destroyed molecules are depicted by the back cross.

6.2 Luminescence simulations

As detailed in Chapter 2, the fundamental process of light emission involves the injection of an electron and a hole into the device, leading to their recombination into an exciton which ideally decays radiatively by emitting a photon. Due to spin-statistics, three quarters of the generated excitons will be in a triplet spin state, which can only decay radiatively by a phenomenon known as phosphorescence. The phosphorescence rates of the host sites in this study are exceedingly low, reflecting real-world conditions. Therefore, for triplet excitons to radiatively decay, they must do so within the emitter molecules. Triplet excitons can either be generated directly on the emitter molecules or in their vicinity, requiring them to migrate towards the emitters where they eventually decay by emitting a photon. In both scenarios, the host molecules surrounding the emitters play a crucial role by transporting charge carriers for recombination. These percolation paths through the hosts are vital for exciton generation and subsequent photon emission.

In the case of emitter-only degradation, the overall luminance naturally decreases due to the absence of intact phosphorescent molecules capable of converting triplet molecules into photons. During simulation, any degradation-triggering event occurring within the first one million KMC steps are ignored to allow the system to reach a steady state. After this initialization phase, each subsequent degradation trigger event results in immediate degradation of the target molecule.

Given the stochastic nature of the KMC simulation, I conducted a total of 40 degradation simulations for virtual devices using 20 different initial random seeds. These random seeds determine the energetic landscape and overall characteristics of each device. For each of the 20 replicas, degradation simulations were performed in both host-only and emitter-only modes. This approach allows for easier comparison between modes on the same initial device configuration and minimizes performance variations due to statistical reasons.

The total number of emitted photons by time t is denoted as $n(t_i)$. Figure 6.3 displays the number of emitted photons and the KMC time for 10 of the 20 replicas.

Observing the plot, it is evident that the slope of the emitter-only mode decreases much more rapidly compared to the host-only mode. By 20 µs of KMC time, the red curve shows a noticeable flattening, indicating a significant reduction in the emission rate. On the other hand, the blue curve exhibits a visible flattening much later, around the scale of 1×10^{-2} s (right side).

The slope of the curves can be calculated using the formula:

$$\text{slope}(t_i) = \frac{1}{t_{i+1} - t_i}\,, \tag{6.1}$$

This calculation is based on the fact that the difference in the number of photons between consecutive times is always $n(t_{i+1}) - n(t_i) = 1$. Figure 6.4 illustrates the slopes for one replica in both degradation modes, showing a decrease in the slope for the emitter-only mode compared to the host-only mode.

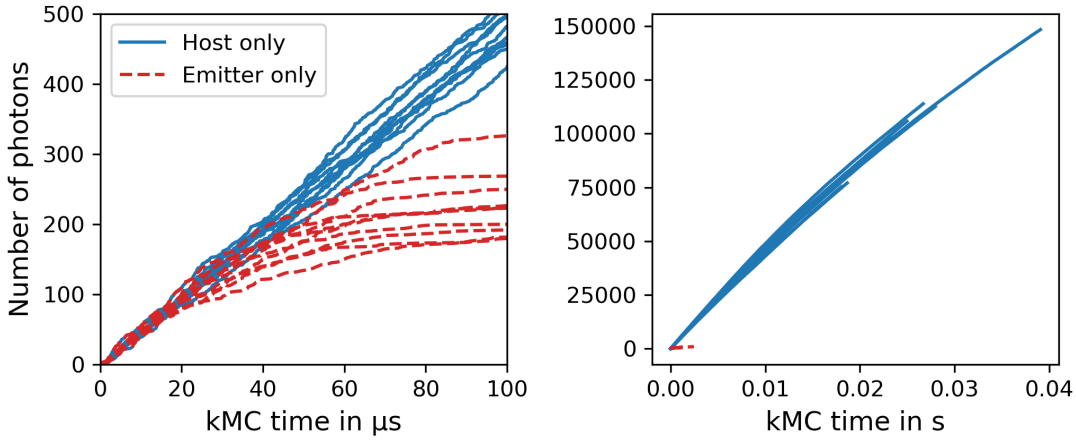

Figure 6.3: Number of emitted photons against the KMC-time. The blue solid lines represent the number of photons emitted in the host-only mode for ten different device replicas, while the red dashed lines represent the emitter-only simulations for the same replicas.
On the left side of the plot, which displays emitted photons over KMC time up to 1 µs, there is a noticeable difference between the two modes. Between 20 µs and 40 µs, the slope of the emitter-only mode curves decreases significantly compared to the host-only mode curves, indicating a sharp reduction in photons emitted per unit time and consequently in luminosity.
On the right side of the plot, where the time axis extends to the full time-scales of the individual replicas, a similar trend is observed but over a longer duration. The emitter-only mode simulations become barely visible early on because the slope of the photon count function decreases drastically. Additionally, it is evident that although the slope of the host-only mode curves also decreases over time, it does so at a slower rate compared to the emitter-only mode.

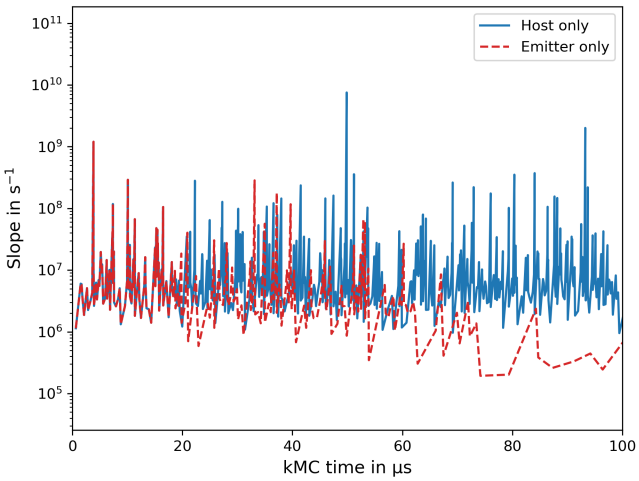

Figure 6.4: Emitted photons per second. Explicitly plotting the slope computed by Equation (6.1) reveals the strong fluctuating behavior due to the varying times between consecutive photon emissions. The significant variability in the time intervals between emissions results in pronounced fluctuations in the slope of the photon count curve. This fluctuation pattern should be considered when analyzing the data further.

However, two critical issues necessitate a more careful analysis of the photon emission rates:

- The emission rates exhibit extreme fluctuations, highlighting the need for statistical analysis across multiple replicas to characterize the emission behavior more reliably.

- The main challenge concerns the timescale of degradation events in the simulations. In the current approach, each degradation-triggering event, immediately results in the degradation of the target molecule. This method leads unrealistic device lifetimes for both degradation modes. In reality, molecules can endure numerous quenching events without breaking down. The probability of a molecule breaking due to exciton-exciton or exciton-polaron quenching events is typically very low [190, 193], requiring a large number of quenching events to observe degradation effects . However, explicitly incorporating these low probabilities to realistically simulate degradation timescales would necessitate enormously long simulations, making them computational unfeasible. Therefore, I simulate the degradation of target molecules without directly modeling the rare occurrence of this event as it happens in reality.

To make computational lifetime studies practical, it is crucial to address this issue. I propose a method to incorporate post-simulation corrections to the system times, allowing for a more realistic estimation of lifetimes based on reasonably short KMC simulations.

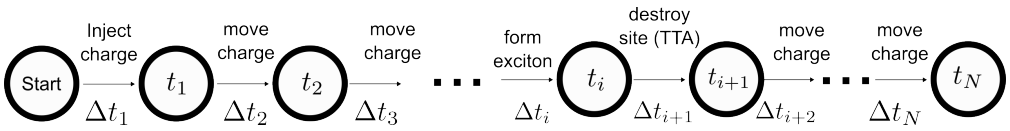

Figure 6.5: Time evolution without time boost. The system time is calculated by summing consecutive time increments corresponding to each KMC-step. In this scenario, we observe that the initial step involves the injection of a charge, followed by two charge hops. In later steps, excitons eventually form and degradation events begin to occur. The first degradation event notably occurs between system states i and $i+1$, resulting in the destruction of one site after the $(i+1)$-th step. Since this rare event is not factored into the time increment calculation, it becomes necessary to adjust all system times after T_i to accommodate the occurrence of this rare degradation event.

6.3 Time scale problem in degradation simulations

In KMC simulations, the time at the beginning is set to zero. After each KMC step i, a time increment Δt_i is randomly drawn from an exponential distribution $\exp(-\Delta t_i \Gamma_i)$, where Γ_i is the sum of the rates of all possible processes that could occur in the ith KMC step.
The total time after N KMC steps is then obtained by adding all increments:

$$t_N = \sum_{i=1}^{N} \Delta t_i \ . \tag{6.2}$$

Initially, most of the processes involve charge injections, followed by numerous charge transfer events. In the example illustrated in Figure 6.5, the first degradation event occurs at step $i+1$. Assuming there are a total of N_d degradation events, these N_d time increments do not account for the fact that a large number of quenching events are needed to destroy the targeted site.

6.3.1 Accelerating KMC kinetics

To address the timescale issue, I boost the N_d time increments corresponding to degradation events. Continuing with the example in Figure 6.5, the time increment Δt_{i+1} gets an additional term:

$$\Delta t_{i+1}^{(1)} = \Delta t_{i+1} + \tau \ . \tag{6.3}$$

The goal of this term is to correct the severely underestimated time increment Δt_{i+1} to a value resembling realistic time passage after one molecule has been degraded, denoted as $\Delta t_{i+1}^{(1)}$.
This correction is achieved by considering what was overlooked when immediately destroying the molecule upon the first quenching event. As discussed earlier, the molecule must undergo numerous quenching events before degradation occurs. I introduce a factor ν to represent how many times this must happen. Additionally, the typical time between quenching events targeting a particular molecule

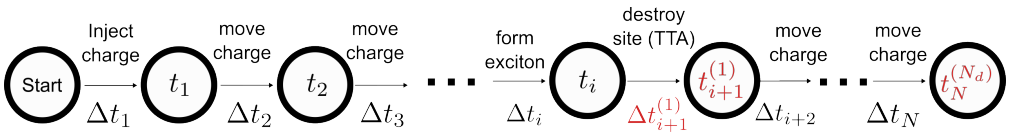

Figure 6.6: System time with boosted degradation times. The system time depicted in Figure 6.5 does not consider that degradation events occur over significantly longer timescales than what can be realistically modeled in conventional KMC simulations without adjusting the timescale. Specifically, the time increment Δt_{i+1} associated with the first site degradation needs to be increased, as described in Equation (6.3). This adjustment must be applied to all subsequent times after the occurrence of each degradation event.

is denoted by a factor α. Together, these factors contribute to the time correction:

$$\tau = \nu \cdot \alpha. \tag{6.4}$$

The two factors will be discussed in more detail below.
When applying this scheme, after N KMC steps, where N_d degradation events have occurred, the total time can be calculated as follows:

$$t_N^{(N_d)} = \sum_{i=1}^{N} \Delta t_i + \sum_{j=1}^{N_d} \nu \cdot \alpha \ . \tag{6.5}$$

By incorporating the time boosts outlined in Equation (6.5), realistic timescales for device degradation can be simulated without the necessity of conducting excessively long KMC simulations where the majority of KMC steps are directly relevant to study the loss in luminosity. The challenge lies in obtaining realistic values for the factors ν and α.

6.3.2 The ν and α factors in the time boost

For host materials, the chance to be destroyed upon quenching processes typically hovers around $P_{\text{deg}}^{\text{host}} \approx 1 \times 10^{-9}$ [193, 190]. In this study, I assume that the inverse probability to destroy a molecule is equal to the required number of quenching events to destroy the target. For host molecules, the factor ν is therefore given by:

$$\nu^{\text{host}} = \frac{1}{P_{\text{deg}}^{\text{host}}} = 1 \times 10^{9} \ . \tag{6.6}$$

It can be assumed that emitter molecules have significantly greater stability. In this study, I have set their stability to be 2000 times higher, resulting in $\nu^{\text{emitter}} = 5 \times 10^{11}$.
This assumption is supported by the high thermal stability of typical emitter materials, particularly Iridium-based phosphorescent emitters, which can be indicative of stability against quenching events [194]. In my current toy model simulation, the choice of parameters can be justified based on simplified

Table 6.1: Normalization condition for the fitted parameters of the double exponential distribution.

emitter concentration	1%	5%	10%
hosts $a_1 b_1 + a_2 b_2$ (6.8)	0.9766	0.8903	0.9534
emitters $a_1 b_1 + a_2 b_2$ (6.8)	0.9873	1.004	1.0055

assumptions. However, for more comprehensive degradation simulations of real devices using realistic materials, detailed quantum chemical investigations into the stability of molecules with respect to exciton-polaron and exciton-exciton quenching events would be beneficial.
Alternatively, one could rely on existing experimental data available in the literature for more accurate and realistic material stability modeling. This approach would provide a stronger foundation for understanding and predicting device performance and durability at a more advanced level beyond the scope of a toy model simulation.

Unlike the material stability parameter ν, the typical time interval between two consecutive quenching events on a specific molecule, denoted as α, cannot be determined without conducting prior KMC simulations to measure α. This complexity arises because α is influenced not only by material properties but also by device architecture and operation conditions such as the applied electric field F.
To examine the parameter α, I conducted KMC simulations on the device depicted in Figure 6.1, ensuring no degradation was induced. The applied electric field was $F = 0.095\,\mathrm{V/nm}$.
During each quenching event within the EML, the KMC program logged the system time, identified the targeted molecule along with its position and categorized it as a host or emitter. Next, I filtered out molecules from the log-file that were targeted by quenching less than 50 times. For the remaining molecules, I computed the elapsed time between two successive quenching events and stored this information in a data array, separately for hosts and emitters. Figure 6.7 shows the histograms of these data arrays for a device with a 1% emitter concentration. The histograms will be used to model the α factor.

The distribution conforms to a double exponential function characterized by the general form:

$$p(\alpha) = a_1 \exp\left(-\frac{\alpha}{b_1}\right) + a_2 \exp\left(-\frac{\alpha}{b_2}\right) . \tag{6.7}$$

The histograms are normalized, meaning that their total area sums to 1. Therefore, a key quality criterion for fitting the parameters of model (6.7) to these histograms is:

$$\int_0^\infty \mathrm{d}\alpha \; p(\alpha) = a_1 b_1 + a_2 b_2 = 1 . \tag{6.8}$$

Table 6.1 shows the extent to which the fitted parameters of the host and emitter distributions meet the normalization condition. The fitted distribution of α is subsequently utilized in the time-boost scheme described earlier using the rejection MC method. This method involves generating two random numbers (x, y) from a uniform distribution. If $y \leq p(x)$, then x is accepted as a value for α in the time-boost

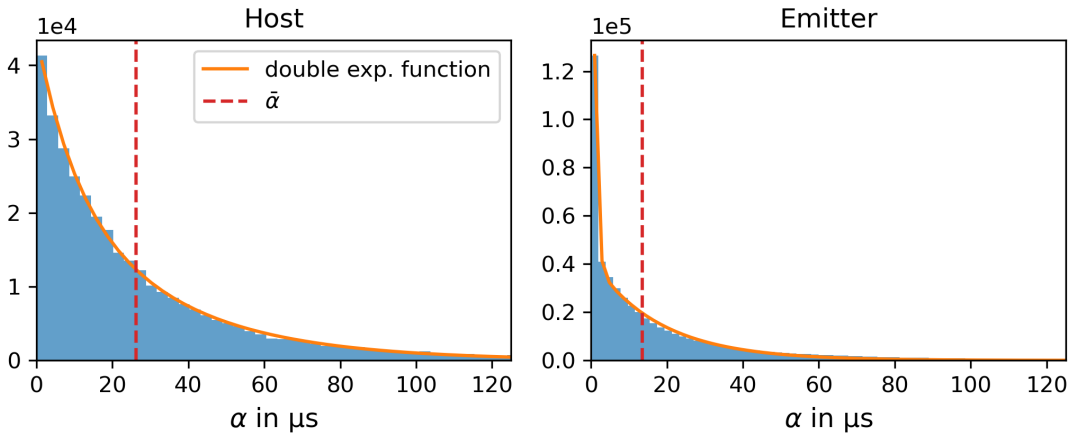

Figure 6.7: Typical time between two quenching events per molecule. The time differences between consecutive quenching events per molecule are depicted in the blue histograms, with hosts on the left and emitters on the right, for a device containing an emitter concentration of 1% and an electrical field of $F = 0.095\,\mathrm{V/nm}$. The distribution exhibits a double-exponential pattern. The expectation value $\bar{\alpha}$ is indicated by the red dashed line.

process.

The expectation value $\bar{\alpha}$ is given by:

$$\begin{aligned}\bar{\alpha} &= \int_0^\infty \mathrm{d}\alpha\ \alpha \cdot p(\alpha) \\ &= a_1 b_1^2 + a_2 b_2^2\,. \end{aligned} \tag{6.9}$$

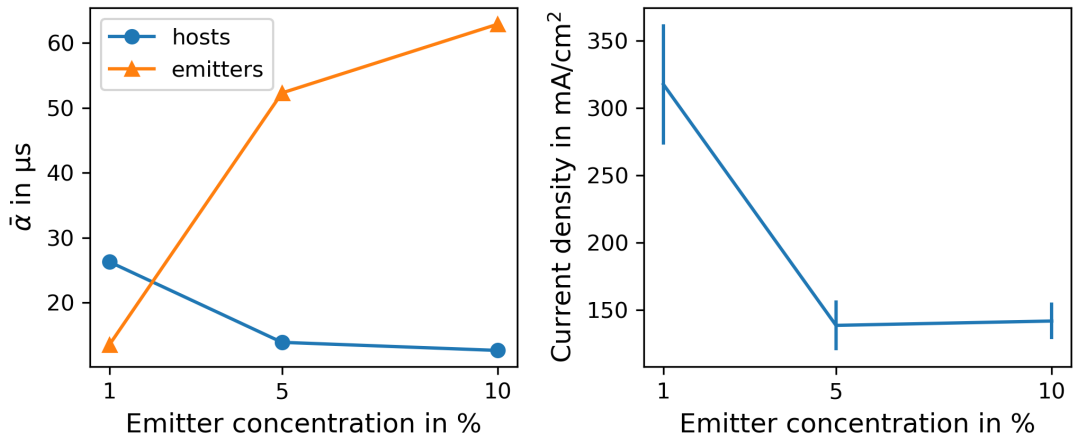

Figure 6.8: Effect of emitter concentration on the typical times between quenching events. Presented are the expectation values of the double exponential distributions for devices with 1%, 5%, and 10% emitter concentration. In host molecules, the mean value $\bar{\alpha}$ decreases with increasing emitter concentration, while for emitter molecules, the opposite trend is observed.

This parameterization was also applied to devices featuring higher emitter concentrations of 5% and 10%. The same electric field was applied across all three emitter concentrations.
To investigate how the emitter concentration affected the typical times between consecutive quenching events, I plotted the obtained mean values $\bar{\alpha}$ (Equation 6.9) for hosts and emitters across all three concentrations in Figure 6.8. The plot clearly shows that for emitter molecules, $\bar{\alpha}$ increases significantly with higher emitter concentrations. This increase is associated with the reduced current densities observed with larger emitter concentrations (refer to Figure 6.8, right panel).
For host molecules, there is a slight decrease in $\bar{\alpha}$. This can be understood by the fact that higher emitter concentrations reduce the conductivity of the EML, leading to charge accumulations at the interfaces. The elevated carrier concentrations at the interfaces promote quenching events on host molecules in these regions to a limited extent.

6.4 Lifetime analysis

A model was introduced to accelerate the KMC kinetics based on factors ν and α in equation (6.5). The parameter ν represents a molecular property indicating the likelihood of a molecule being deactivated through exciton-exciton or exciton-polaron quenching. I estimated ν for both hosts and emitters as discussed in the previous section. The factor α quantifies the time-typical interval between two quenching events occurring on a single molecule. The analysis presented in Figure 6.7 is based on dedicated KMC simulations where for multiple hosts and emitters, the elapsed time between two quenching events have been measured.
Now that all parameterizations and methods to address the timescale issue for lifetime analysis have

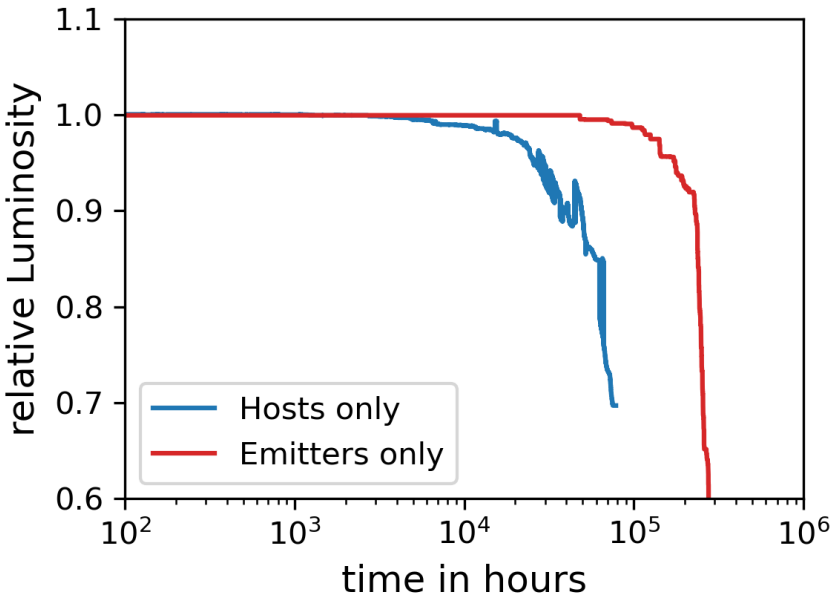

Figure 6.9: Luminance loss curves. For both degradation cases the luminance relative to the initial lumance decreases with increasing operating time.

been discussed, I present the luminance loss curves obtained. The slope of photons-per-KMC-time for the replicas was computed as discussed in equation (6.1).

To mitigate extreme slope fluctuations observed in individual replicas (as shown in Figure 6.4), I had to further process the slope-data. Therefore, I aggregated the data for all replicas into a single two-dimensional array denoted as $\text{slope}_A(t_i)$, where the subscript A signifies combined data from all replicas. After sorting the data by ascending times and applying a subsequent median filter, smooth slope data with corresponding system times was obtained.

Next, the times need to be boosted according to the scheme discussed in equation (6.5), as illustrated in Figure 6.6, where each time, the α factor is generated according to the rejection-MC algorithm.

The obtained luminance curves for the device with a 1% emitter concentration are shown in Figure 6.9. These curves are plotted relative to the initial luminance.

In the host-only case (blue), the luminance begins to decrease slightly around 3000 hours. Between ten thousand and one hundred thousand hours, the host-only case experiences a significant reduction in luminance. In contrast, in the emitter-only case (red), the luminance curves start declining around one hundred thousand to two hundred thousand hours. From these results, I conclude that host degradation affects luminosity earlier than the degradation of emitters. At around 50,000 hours of operation time, the emitter-only simulation still retains most of its initial luminosity, whereas the host-only case has decreased to 85% of its initial value as shown in Figure 6.9.In the scenario focusing solely on the emitter, a notable decrease in luminance is observed after approximately 200,000 hours of operation.

These findings indicate that, in the device depicted in Figure 6.1 with an emitter concentration of 1%, the lifetime limitation is primarily attributed to the degradation of host molecules.
In both scenarios, the decline in luminance does not occur gradually but initiates after a critical point where a significant fraction of host or emitter molecules degrade. This suggests that certain hosts or emitters play a more crucial role in electroluminescence than others, highlighting a percolative nature of carrier transport. Furthermore, this observation suggests that the energetic disorder within such devices, particularly within the host material in the EML, may influence device lifetime, as energetic disorder is predominantly responsible for percolative transport.
The main challenge with this method is the substantial computation time required to generate the luminosity loss curves shown in Figure 6.9. For the host-only case, one billion KMC steps were necessary, mainly because most quenching events target emitter molecules. In contrast, the emitter-only case required only 90 million KMC steps. This disparity in computational costs underscores why simultaneous host and emitter degradation simulations are not feasible with this approach. The problem of reaching significant luminance loss, became more sever with higher emitter concentrations. I was unable to observe significant device degradation even after one billion KMC steps.

6.5 Extrapolated device states

To overcome the challenge of conducting excessively long KMC simulations, I implemented a different approach to generate the luminance degradation curves. In this new method, I employ a linear model to describe the fraction of intact hosts or emitters as a function of time. Rather than conducting simulations where the fraction of intact molecules decreases gradually over time, I used the model to extrapolate the fraction of intact molecules to larger time scales. This approach allows me to simulate the device over extensive time periods in a parallel manner without explicitly simulating degradation as a drift effect during the simulation. By predefining the state of the hosts or emitters at each time, I can efficiently study the long-term behavior of the device and generate accurate luminance loss curves.
The approach involves monitoring the degradation of molecules over a short time, constructing a model based on these observations, and using this model to extrapolate the degradation behavior over longer timescales.
During the simulation, the fraction of intact host and emitter molecules decreases depending on the simulation mode. I recorded each instance of molecule destruction along with its corresponding destruction time. Subsequent destruction times were then adjusted using the time-boost scheme described earlier. This adjustment enabled the analysis of the fraction of intact host or emitter molecules at the boosted time. On the boosted time-scale for both host and emitter molecules, the degradation behavior exhibits a linear trend over time. This is particularly advantageous because it allows for the straightforward fitting of a linear function to describe the rate at which intact molecules degrade within the device. The benefit of this approach is that we can use KMC simulations with significantly fewer steps to parameterize this linear model and still gain valuable insights into the degradation process.

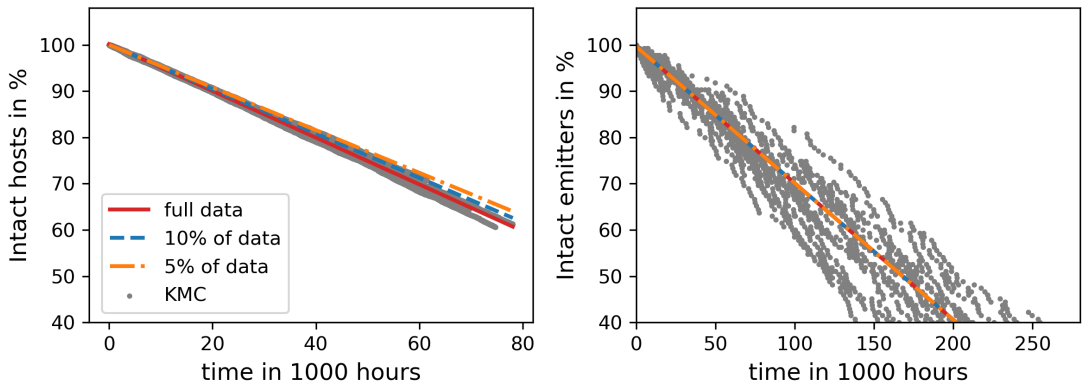

Figure 6.10: Intact molecules of device with 1% emitter concentration. The blue dots in the figure represent the fraction of intact host molecules (on the right) and emitter molecules (on the left) across all 20 replicas. It is clear that on the boosted time-scale, the fraction of intact molecules decreases linearly over time. The black curve illustrates the linear model fitted to the molecule degradation trend.

To determine the necessary number of data points for an accurate parametrization of the linear model describing molecule degradation, I performed linear fits using different percentages of the full KMC data. Specifically, I compared fits using the full dataset, 10% of the dataset, and 5% of the dataset.
Figure 6.10 shows the fraction of intact host and emitter molecules plotted against boosted times. The gray dots represent the data directly obtained from the KMC log-files. The red line represents the linear model fitted to all of the KMC data. The blue and orange lines represent the linear models fitted to only 10% and 5% of the KMC data, respectively.
For host degradation, it was observed that using only 10% of the full KMC data for the fit provides a very close match to the model fitted to the full dataset. However, using only 5% of the dataset leads to slight differences in the slope, resulting in a minor overestimation of intact host molecules at longer operation times.
In contrast, for emitter degradation, using just 5% of the data is sufficient to obtain an accurate fit.

These results indicate that we can reduce the number of KMC steps by a factor of 20 while still accurately modeling molecule degradation in the device. The fitted models for higher concentrations of emitters are depicted in Figure 6.11. In the case of host degradation, higher emitter concentrations accelerate the decay of host molecules within the EML. Conversely, for emitter-only degradation, we observe that with higher emitter concentrations, it takes significantly longer to reduce the fraction of intact emitters.

6.5.1 Validation of the surrogate model

A key unresolved issue concerns understanding whether device degradation, particularly in terms of luminance loss, is solely due to molecule destruction or if additional effects depicted in the explicit

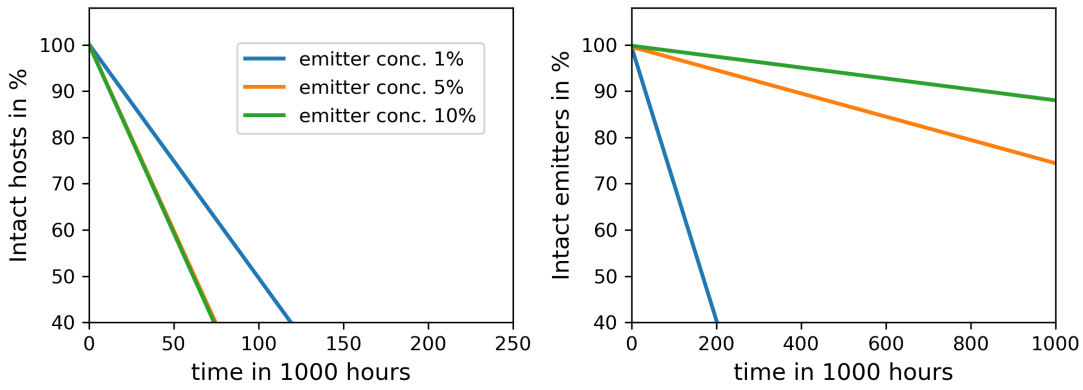

Figure 6.11: Intact molecules for all emitter concentrations. The linear fit to the KMC data of intact molecules is applied to all three cases. Through this fitting procedure, it becomes feasible to predict the fraction of intact molecules at extended operation times without the need for explicit KMC simulations to be conducted. This approach leverages the fitted models to estimate behavior over time, offering a more efficient and streamlined method for analyzing device performance without resorting to lengthy simulation runs.

degradation simulations (Figure 6.9) contribute to this phenomenon. For example, phenomena like exciton-polaron quenching can lead to charge carriers becoming trapped on specific sites, creating static quenchers that influence subsequent exciton interactions. Additionally, there may be memory or correlation effects associated with the destruction of specific sites that are not accounted for when extrapolating the fraction of intact molecules from the linear model and creating multiple device copies in varying states concerning the scale of destroyed molecules.

To validate the surrogate model developed for the device with a 1% emitter concentration, I performed digital simulations at various time points where I computed the fraction of intact hosts in the emissive layer (EML) or intact emitters using the discussed linear models. For each time point, I generated 20 replicas to capture statistical variability.
In the initialization, intact and destroyed molecules are blended to the corresponding fractions inside the EML. Subsequently, I conducted KMC simulations with a total of 20 million steps for each replica and time point without allowing further degradation processes to occur, ensuring a constant slope (6.1) for each simulation.
For each replica, I extracted the median slope along with its standard deviation. Figure 6.12 presents the comparison of the resulting luminance-loss curves. The transparent lines depict the outcomes from the gradual degradation simulations (referred to as drift degradation simulations) as previously described. The luminance values for the extrapolated devices are shown as circles along with the standard deviations. This approach will henceforth be referred to as the surrogate model.

The strong agreement observed between the results of both degradation host-only and emitter-

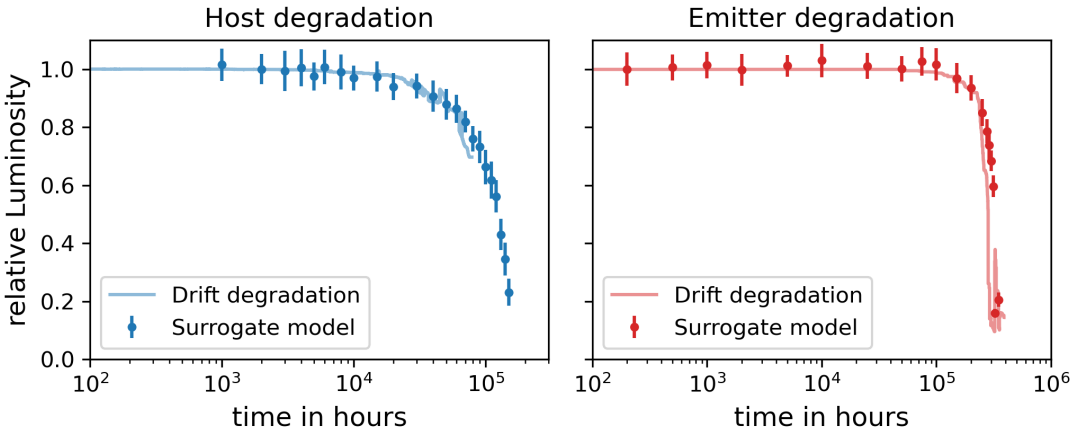

Figure 6.12: Validation of the surrogate degradation model. The luminance-loss curves from the drift degradation simulations presented in Figure 6.9 are displayed. Comparing these curves with the luminance-loss obtained from the surrogate model clearly demonstrates that instead of conducting excessively long drift simulations, it suffices to fit the linear model for intact molecules shown in Figure 6.11 to shorter drift degradation runs, extrapolate to desired times, and compute the luminance of the extrapolated devices.

only—using the drift degradation simulations and the surrogate model provides compelling evidence for the validity of the surrogate model. This validation allows us to conduct lifetime simulations for devices with higher emitter concentrations or more complex architectures.

It is worth noting that the surrogate model significantly reduces the number of required KMC-steps in the drift degradation runs compared to full luminance-loss studies while still producing closely matching results.

6.5.2 Effect of higher emitter concentrations

The linear models for intact molecules depicted in Figure 6.11 were utilized to compute the degradation of devices with 5% and 10% emitter concentrations, again using the surrogate model. The resulting luminance-loss curves are presented in Figure 6.13.

For host-only degradation, it is evident that the device with a 1% emitter concentration exhibits a significantly longer lifetime compared to those with higher emitter concentrations. This difference arises because higher emitter concentrations lead to increased exciton density due to the preference for exciton formation at the emitters, thereby enhancing quenching effects. This phenomenon was discussed in Chapter 5 and can also be inferred from the steeper slopes of the 5% and 10% host-only degradation curves in Figure 6.11.

A notable observation is made in the case of emitter-only degradation. Before the luminance begins to decline, there is an initial increase of approximately 20% to 30% in luminance before experiencing a sudden drop. This behavior is not observed in the device with a 1% emitter concentration. To further

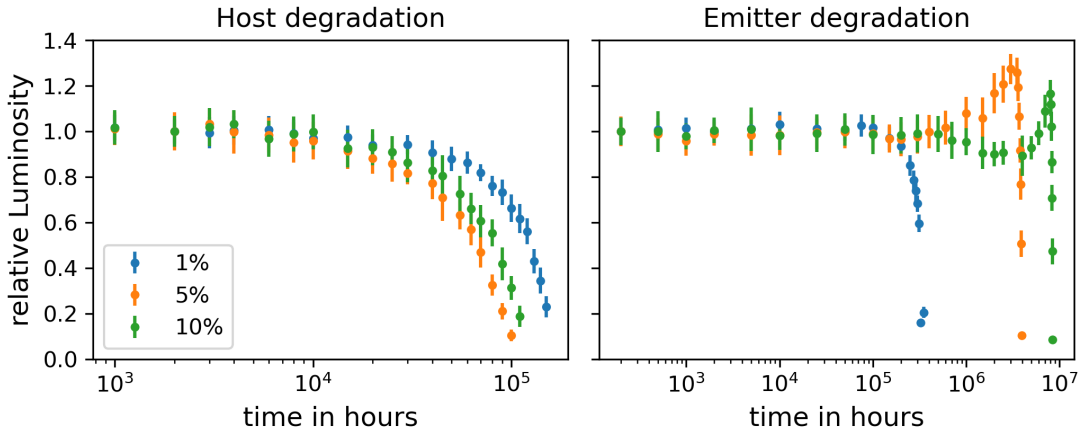

Figure 6.13: Luminance-loss of devices with higher emitter concentration. The left side shows luminance loss curves for devices with 1% (blue), 5% (orange), and 10% (green) emitter concentration subjected to host-only degradation conditions. On the right side, luminance curves for emitter degradation only are presented. These curves exhibit an unusual pattern where luminance initially increases before sharply decreasing. This behavior can be attributed to an increased current density resulting from emitter degradation. The heightened current density leads to greater exciton generation and subsequent photon emission from the remaining intact excitons until all relevant emitters are degraded.

investigate the behavior, I plotted the change in current density relative to the initial current density, as shown in Figure 6.14. There is a fundamental difference in the behavior of current density between host degradation and emitter degradation.

In the case of host degradation, the current density decreases over time. This decline is expected because charges are primarily transported through the host molecules. Therefore, as these host molecules degrade, the overall current density naturally decreases. Additionally, the percolative paths through the host molecules that facilitate charge carrier transport to the emitter molecules are disrupted over time, further reducing both current density and luminance.

On the other hand, in the case of emitter degradation, the current density increases over time. This phenomenon is intriguing and suggests a different mechanism at play.

For charge transport, emitter molecules can indeed act as traps, which can be detrimental to achieving high conductivity. As shown in Figure 6.1, the mean LUMO and HOMO levels of the emitter molecules are structured in a manner that attracts charge carriers, effectively trapping them within the molecules. Therefore, when emitter molecules are destroyed, the trap density within the emissive layer (EML) is reduced. This reduction in trap density contributes to enhancing the overall current density within the device. By reducing the number of trapping sites through emitter degradation, charge carriers experience fewer obstacles and can move more freely through the material, leading to increased current density.

Regarding the luminance behavior of the 5% and 10% devices, the luminance peaks around 5 million and 9 million hours, respectively. At these points, a significant number of emitters have already been

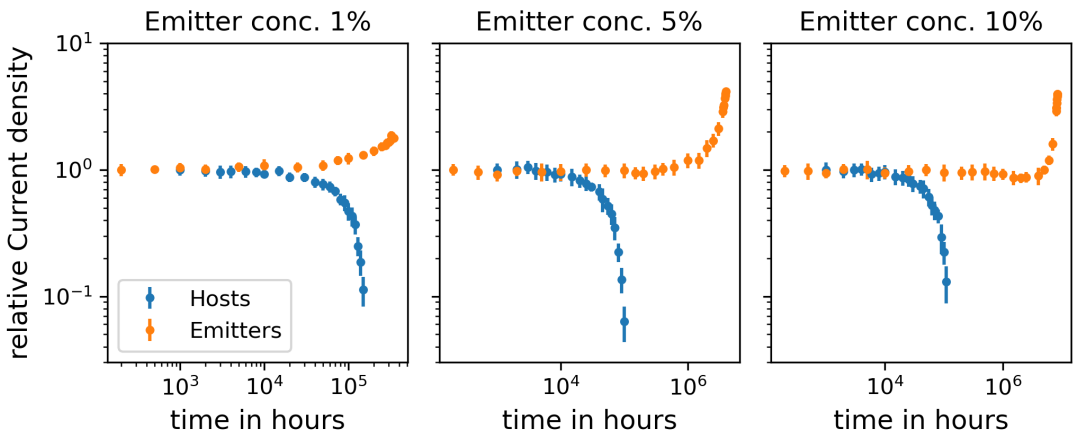

Figure 6.14: Change in current density. In host degradation, the current density decreases as the number of degraded host molecules increases. This reduction occurs because the host molecules predominantly carry the majority of the current through the device. Conversely, emitter degradation results in an increase in current density due to the destruction of emitters, which act as carrier traps within the device. This explains the behavior of the luminance curves of the emitter degradation case shown in Figure 6.13.

destroyed, but enough remain to generate photons from the triplet excitons. The increased current at these times improves the feeding of charges to the remaining excitons, thus boosting luminance. However, as more emitters are destroyed over time, the increased current eventually becomes ineffective because there are insufficient emitters left to sustain photon generation. This effect is less prominent in the luminance-loss curve of the 1% device, but there is still a small increase in current due to emitter degradation.

6.6 Conclusion

Previous computational studies on OLED lifetime [190, 191, 57, 193] have highlighted that intrinsic degradation in OLED devices is primarily attributed to excitonic quenching events that lead to the degradation of host or emitter molecules. However, simulating the luminance loss of commercially available OLED devices is challenging due to the extensive timescales involved in device lifetimes.
Hauenstein et al. [193] attempted to address this challenge by extrapolating device lifetimes based on a power-law relationship between lifetime and current density. This involved performing simulations at high current densities to accelerate device degradation and then extrapolating the obtained lifetime back to lower current densities [193]. Nevertheless, this approach only allowed simulations up to around 2,000 hours of device operation, which is significantly shorter than the lifetimes of commercial OLEDs, which typically range from tens to hundreds of thousands of hours.
In this work, I developed an accelerated KMC model for lifetime studies capable of simulating up to sev-

eral hundred thousand hours of operation time. This advancement enables realistic lifetime simulations of OLED devices. This was achieved by combining two key strategies:

- Boosting simulation time to realistic scales: I employed a method to accelerate KMC kinetics, allowing for the realistic description of luminance loss over extended timescales (6.5). This involved boosting the KMC time-increments Δt after processes involving excitonic quenching. The time boost incorporated two factors: a factor for molecular stability (ν) and a factor for the quenching frequency on individual molecules (α), the latter of which required parameterization through short KMC simulations (see Figure 6.7).

- Reducing the number of necessary KMC steps: given the computational costs of modeling degradation processes, I implemented a strategy to reduce the number of KMC steps by up to ten-fold (see Figure 6.10). This was achieved by fitting a linear model to the fraction of intact emitters or hosts versus operation time. The model could then be used to extrapolate the fraction of intact molecules to time points that are challenging to reach with direct KMC simulations.

By incorporating these methodological improvements, I simulated device degradation with varying emitter concentrations up to large timescales which was to my knowledge not feasible so far.
The results revealed distinct effects depending on whether hosts or emitters degrade within the device. Host degradation led to a steady reduction in luminance and current density (Figures 6.13 and 6.14, respectively), as the main current carriers are host molecules.
Emitter degradation did not result in a steady reduction in luminance or current density. Instead, destroying emitter molecules which act as charge traps, increased the current density (Figure 6.14). However, this increase in current density did not correspond to increased luminance, as all the phosphorescent emitters were eventually destroyed, preventing the phosphorescence of triplet excitons. The presented method provide valuable insights into the complex dynamics of device degradation and its impact on device performance.

7

Summary, Conclusion and Outlook

Amorphous semiconductors based on small organic molecules are widely used as fundamental building blocks for various organic electronics applications, particularly in OLEDs. Theoretical and computational modeling of complete devices, spanning from the molecular to mesoscopic scales, presents numerous challenges associated with bridging wide ranging time- and length-scales. To address these challenges, it is essential to integrate methods from different disciplines, each with unique objectives, into a cohesive multiscale simulation protocol.

In this thesis, I applied a multiscale approach to simulate charge transport in organic semiconductors and model the performance of complete devices, addressing key questions related to their operational efficiency and longevity. My research involved a diverse range of computational methods, including electronic structure calculations, generation of amorphous thin films, and large time-scale kinetic Monte Carlo simulations.

By integrating these methods, I aimed to embody the essence of multiscale modeling, where insights gleaned from different computational approaches are synergistically combined to gain a in-depth understanding of organic semiconductor devices. This approach allowed for a comprehensive exploration of device behavior, spanning from the molecular level to mesoscopic scales, and facilitated the analysis of complex phenomena such as charge transport, exciton quenching, and device degradation mechanisms. The utilization of electronic structure calculations enabled the characterization of material properties at the atomic and electronic level, providing crucial input for subsequent simulations. The generation of amorphous thin films allowed for the realistic representation of material structures encountered in

practical devices. Finally, large time-scale KMC simulations provided insights into device performance over extended operational periods, offering valuable predictions on efficiency and lifetime behavior. Through the integration of these computational methodologies, this thesis contributes to advancing our understanding of organic semiconductor devices and provides practical insights for optimizing device design and performance.

7.1 Summary & Conclusion

Predicting charge mobility in organic semiconductors is a critical aspect of OLED simulations. Current methods often either assume a static morphology, disregarding fluctuations, or neglect coupling fluctuations due to computational complexity. In this work, I introduced an approach that focuses on the dynamic behavior of molecules within the amorphous matrix, specifically addressing the total disorder of HOMO energies and intermolecular HOMO couplings.

This approach employs a workflow combining MD, DFTB, and KMC. By leveraging this workflow, time series of couplings and site energies are calculated, enabling the examination of hole transfer parameter dynamics across the morphology. This provides insights into both static and dynamic contributions to total energetic disorder, allowing for time-averaging of electronic couplings and their integration into a KMC model for simulating hole mobility.

Incorporating MD trajectories expands the sampling scope of energy and coupling, allowing for mobility predictions that explicitly consider structural dynamics. This analysis yields valuable insights into the underlying causes of total energetic disorder, including contributions from both static and dynamic factors. By studying the HOMO structure within random molecules of each material, we can identify origins of dynamic disorder, informing strategies for designing materials with reduced dynamic disorder through localization of HOMO or utilizing materials with higher glass transition temperatures to limit molecular flexibility at room temperature.

Furthermore, investigating fluctuations in intermolecular couplings, following methods like those by Skourtis et al. [137], reveals that coupling fluctuations notably impact short-distance pairs but can be disregarded for large center-of-mass distances.

For instance, the impact of coupling fluctuations on TPDI mobility is demonstrated in Figure 4.19. The observed weak coupling fluctuations (as shown in Figures 4.16 and 4.17) align with the expected result that coupling fluctuations do not significantly affect TPDI mobility.

Ultimately, this sampling and analysis approach aims to guide the rational design of high-mobility organic semiconductors by elucidating the intricate relationship between molecular dynamics and charge transport properties. By gaining deeper insights into how molecular structural dynamics impact charge mobility, this research can inform the strategic selection and modification of organic semiconductor materials to optimize their performance in electronic devices, particularly in applications like OLEDs where efficient charge transport is essential for device functionality and longevity. The goal is to leverage this understanding to design novel materials with tailored molecular architectures that minimize dynamic disorder and enhance charge mobility, ultimately advancing the development of next-generation or-

ganic electronic devices.

The performance of OLEDs relies not only on intrinsic material properties like carrier mobility, as studied in Chapter 4, but also on the arrangement of different materials within the device architecture. In Chapter 5, I employed parametric KMC simulations to analyze three distinct OLED architectures (A1, A2, and A3) incorporating a phosphorescent emitter blended with the host material in the emissive layer (EML) [182]. This investigation revealed significant variations in device performance, particularly in internal quantum efficiency and current-density behavior, as illustrated in Figure 5.2. By examining particle profile plots (Figure 5.3), I identified key bottlenecks specific to each architecture.
For A1, we observed suboptimal charge balance within the EML, leading to heightened TPQ, particularly at the interface with the transport layers, and a high occurrence of TTA processes within the EML (Figure 5.3C). To address this issue, I introduced charge injection layers between the electrodes and transport layers to improve charge balance within the EML. However, this approach resulted in undesired exciton generation in the injection layers due to their small HOMO-LUMO gap, as depicted in Figure 5.3E and F. Despite incorporating charge blocking layers to enhance device efficiency, the roll-off effect persisted.
In the case of the multilayer architecture (A3), I further optimized internal quantum efficiency by adjusting emitter concentration and EML thickness (Figures 5.4 and 5.5). The simulations indicated that optimal low-current IQEs were achieved with emitter concentrations around 5%, consistent with previous reports [38, 179]. However, the device still experienced roll-off due to TTA and TPQ processes [52]. Increasing the EML thickness led to further improvements in efficiency and reduced roll-off at current densities around $1 \times 10^4\,\mathrm{mA/cm^2}$.
The simulations highlight the usefulness of heuristic models in analyzing device architecture and identifying parameters influencing efficiency. By pinpointing performance bottlenecks specific to each architecture, this computational approach offers a cost-effective and time-efficient alternative to experimental methods.

Beyond device efficiency, the longevity of OLED devices is a critical factor for their practical application. Building upon the work presented in Chapter 5, I extended the KMC model to incorporate molecular degradation induced by exciton-exciton and exciton-polaron quenching events.
Device degradation occurs over time scales of several tens or hundreds of thousands of hours of operation, making direct simulation of device degradation with KMC methods impractical. To tackle these challenges, I implemented two strategies: I boosted the KMC time increments (Δt) based on factors (ν and α) to simulate realistic luminance loss over extended operational periods. The α factor, representing quenching frequency, was parameterized using short KMC simulations (see Figure 6.7). To reduce computational costs, I developed a linear model to predict intact molecule fractions over time, allowing for a reduction of up to 10% in necessary KMC steps (Figure 6.11). These methods enabled the simulation of device degradation under varying emitter concentrations. Results showed distinct effects of host versus emitter degradation:

Host degradation led to steady reductions in luminance and current density (Figures 6.13 and 6.14), impacting main current carriers. Emitter degradation increased current density due to charge trapping by destroyed emitters, without a corresponding increase in luminance, preventing triplet excitons from transforming into light.
These findings emphasize the importance of molecular-level processes in optimizing OLED longevity and stability.

7.2 Outlook

Earlier multiscale workflows for computing carrier mobility utilized a static morphology model where, following virtual deposition, the amorphous structure was assumed to remain unchanged [125]. Implementing this approximation for sufficiently large structures (around 5000 molecules) and averaging over 2-3 replicas provides statistically reliable results for capturing complete energetic disorder. This approach effectively models the carrier mobility of known materials. The methodology presented here, explicitly considering both static and dynamic contributions, offers a decisive advantage over the static approximation. It was demonstrated that, for the materials discussed in this work, both static and dynamic disorder significantly contribute to the overall disorder. Controlling static disorder is challenging due to the complexity of modeling how amorphous structures and packing densities form based on individual molecular considerations. However, the dynamic aspect is more manageable. The analysis conducted in Figures 4.13, 4.14, and 4.15 indicates that designing molecules where the HOMO is localized on immobile segments of the molecules can reduce dynamic disorder. Even a slight reduction in dynamic disorder can greatly enhance hole mobility, as demonstrated in Equation (3.80). Another strategy to improve carrier mobility could involve synthesizing molecules with higher glass transition temperatures to minimize thermal fluctuations and, consequently, dynamic disorder. Overall, the results presented in Chapter 4 lay the groundwork for a more rational optimization strategy aimed at achieving high mobility materials by minimizing dynamic disorder. This methodology not only replicates results obtained with established methods but also provides deeper insights into the origins of energetic disorder.

The devices studied in Chapter 5 and their efficiency loss mechanisms, along with strategies to overcome them, have been relatively straightforward. However, this approach can be extended to more complex devices that incorporate doped injection layers [16, 164, 195]. When dealing with such devices, KMC simulations become computationally expensive due to numerous charge carrier hops within the doped injection layers, leading to prolonged simulation times to reach steady-state conditions.
To address this challenge, I am collaborating with a Master's student to develop a surrogate model tailored specifically for doped injection layers within devices. This model aims to replace regions dominated by charge transfer processes with a resistor network capable of accurately mimicking current density profiles. We have discovered that this approach is versatile and can be extended to encompass multilayered structures, which has motivated us to consider replacing multiple layers in an OLED with

the resistor network.
The development and validation of the resistor network model, intended to replace simulation-intensive yet less informative layers within the device, was conducted concurrently with the writing of this thesis. The next step involves interfacing this resistor network model to the existing KMC model.
While the exact strategy for integrating the validated resistor network model into a hybrid simulation framework is yet to be tested, the foundational components are in place. This integration is expected to significantly reduce simulation times, as explicit KMC simulations will only be conducted within the emissive layer, thereby increasing efficiency by several orders of magnitude.

As a final direction, I would like to suggest a more methodologically rigorous approach to studying molecular degradation processes, which were approximated in this work. It is possible to conduct detailed quantum chemical investigations into the reaction pathways involved in molecular cleavage triggered by exciton-exciton or exciton-polaron quenching.
An in-depth quantum chemical analysis of the destruction probability (ν^{-1}) for realistic materials, combined with the long-time scale degradation model developed here, could greatly assist researchers and engineers in computationally designing material-device combinations with enhanced lifetimes of organic optoelectronic devices.

Bibliography

[1] Stephen R. Forrest and Mark E. Thompson. "Introduction: Organic Electronics and Optoelectronics". In: *Chemical Reviews* 107.4 (Apr. 2007). Publisher: American Chemical Society, pp. 923–925.

[2] C. W. Tang and S. A. VanSlyke. "Organic electroluminescent diodes". In: *Applied Physics Letters* 51.12 (Sept. 1987). Number: 12, pp. 913–915.

[3] https://www.precedenceresearch.com/oled-market Accessed: 21.02.2024.

[4] en-gb. https://impact.economist.com/sustainability/net-zero-and-energy/cities-road-to-2050-lighting-the-way-to-sustainable-growth Accessed: 21.02.2024.

[5] en-US. https://www.fluxim.com/dipole-orientation-led Accessed: 21.02.2024.

[6] H. Bässler. "Charge Transport in Disordered Organic Photoconductors a Monte Carlo Simulation Study". In: *physica status solidi (b)* 175.1 (1993). Number: 1, pp. 15–56.

[7] S.d. Baranovskii et al. "Percolation Approach to Hopping Transport in Organic Disordered Solids". en. In: *physica status solidi (b)* 230.1 (2002). _eprint: https://onlinelibrary.wiley.com/doi/pdf/10.1002/1521-3951%28200203%29230%3A1%3C281%3A%3AAID-PSSB281%3E3.0.CO%3B2-W, pp. 281–288.

[8] L. Li, G. Meller, and H. Kosina. "Percolation current in organic semiconductors". en. In: *Journal of Computational Electronics* 6.1 (Sept. 2007), pp. 357–361.

[9] Tobias Neumann et al. "Modeling disordered morphologies in organic semiconductors". In: *Journal of Computational Chemistry* 34.31 (2013). Number: 31, pp. 2716–2725.

[10] Anna Köhler and Heinz Bässler. *Electronic Processes in Organic Semiconductors: An Introduction*. en. Weinheim, Germany: Wiley-VCH Verlag GmbH & Co. KGaA, May 2015.

[11] Richard H. Friend and Jeremy H. Burroughes. "Charge injection in conjugated polymers in semiconductor device structures". en. In: *Faraday Discussions of the Chemical Society* 88.0 (Jan. 1989). Publisher: The Royal Society of Chemistry, pp. 213–222.

[12] José C. S. Costa et al. "Optical band gaps of organic semiconductor materials". In: *Optical Materials* 58 (Aug. 2016), pp. 51–60.

[13] Felix Gutmann and L. E. Lyons. *Organic Semiconductors*. Englisch. John Wiley & Sons Inc, 1967.

[14] Daniel J. Gaspar and Evgueni Polikarpov, eds. *OLED fundamentals: materials, devices, and processing of organic light-emitting diodes*. eng. Boca Raton ; London ; New York: CRC Press, Taylor & Francis Group, 2015.

[15] Jonas Armleder et al. "Controlling doping efficiency in organic semiconductors by tuning short-range overscreening". en. In: *Nature Communications* 14.1 (Mar. 2023). Publisher: Nature Publishing Group, p. 1356.

[16] Artem Fediai et al. "Disorder compensation controls doping efficiency in organic semiconductors". en. In: *Nature Communications* 10.1 (Oct. 2019). Bandiera_abtest: a Cc_license_type: cc_by Cg_type: Nature Research Journals Number: 1 Primary_atype: Research Publisher: Nature Publishing Group Subject_term: Computational methods;Computational science;Electronic devices;Semiconductors Subject_term_id: computational-methods;computational-science;electronic-devices;semiconductors, p. 4547.

[17] Shi-Jie Zou et al. "Recent advances in organic light-emitting diodes: toward smart lighting and displays". en. In: *Materials Chemistry Frontiers* 4.3 (Mar. 2020). Publisher: The Royal Society of Chemistry, pp. 788–820.

[18] Bernard Geffroy, Philippe le Roy, and Christophe Prat. "Organic light-emitting diode (OLED) technology: materials, devices and display technologies". en. In: *Polymer International* 55.6 (2006). _eprint: https://onlinelibrary.wiley.com/doi/pdf/10.1002/pi.1974, pp. 572–582.

[19] W. Helfrich and W. G. Schneider. "Recombination Radiation in Anthracene Crystals". In: *Physical Review Letters* 14.7 (Feb. 1965). Publisher: American Physical Society, pp. 229–231.

[20] W. Helfrich and W. G. Schneider. "Transients of Volume-Controlled Current and of Recombination Radiation in Anthracene". In: *The Journal of Chemical Physics* 44.8 (Apr. 1966), pp. 2902–2909.

[21] P. S. Vincett et al. "Electrical conduction and low voltage blue electroluminescence in vacuum-deposited organic films". In: *Thin Solid Films* 94.2 (Aug. 1982), pp. 171–183.

[22] Yue Qu, Michael Slootsky, and Stephen R. Forrest. "Enhanced light extraction from organic light-emitting devices using a sub-anode grid". en. In: *Nature Photonics* 9.11 (Nov. 2015). Publisher: Nature Publishing Group, pp. 758–763.

[23] Alongkarn Chutinan et al. "Theoretical analysis on light-extraction efficiency of organic light-emitting diodes using FDTD and mode-expansion methods". In: *Organic Electronics* 6.1 (Feb. 2005), pp. 3–9.

[24] Tetsuo Tsutsui. "Progress in Electroluminescent Devices Using Molecular Thin Films". en. In: *MRS Bulletin* 22.6 (June 1997), pp. 39–45.

[25] Oskar Sachnik et al. "Elimination of charge-carrier trapping by molecular design". en. In: *Nature Materials* 22.9 (Sept. 2023). Publisher: Nature Publishing Group, pp. 1114–1120.

[26] Chihaya Adachi et al. "Nearly 100% internal phosphorescence efficiency in an organic light-emitting device". In: *Journal of Applied Physics* 90.10 (Nov. 2001), pp. 5048–5051.

[27] R. Coehoorn, P. A. Bobbert, and H. van Eersel. "F\"orster-type triplet-polaron quenching in disordered organic semiconductors". In: *Physical Review B* 96.18 (Nov. 2017). Publisher: American Physical Society, p. 184203.

[28] He Jiang, Peng Tao, and Wai-Yeung Wong. "Recent Advances in Triplet–Triplet Annihilation-Based Materials and Their Applications in Electroluminescence". In: *ACS Materials Letters* 5.3 (Mar. 2023). Publisher: American Chemical Society, pp. 822–845.

[29] Y.r. Do et al. "Enhanced Light Extraction from Organic Light-Emitting Diodes with 2D SiO2/SiNx Photonic Crystals". In: *Advanced Materials* 15.14 (2003). _eprint: https://onlinelibrary.wiley.com/doi/pdf/10.1002/adma.2 pp. 1214–1218.

[30] Yiru Sun and Stephen R. Forrest. "Enhanced light out-coupling of organic light-emitting devices using embedded low-index grids". en. In: *Nature Photonics* 2.8 (Aug. 2008). Publisher: Nature Publishing Group, pp. 483–487.

[31] M. A. Baldo et al. "Highly efficient phosphorescent emission from organic electroluminescent devices". en. In: *Nature* 395.6698 (Sept. 1998). Publisher: Nature Publishing Group, pp. 151–154.

[32] J. H. Burroughes et al. "Light-emitting diodes based on conjugated polymers". en. In: *Nature* 347.6293 (Oct. 1990). Publisher: Nature Publishing Group, pp. 539–541.

[33] M. A. Baldo et al. "Very high-efficiency green organic light-emitting devices based on electrophosphorescence". In: *Applied Physics Letters* 75.1 (July 1999), pp. 4–6.

[34] M. A. Baldo et al. "Excitonic singlet-triplet ratio in a semiconducting organic thin film". In: *Physical Review B* 60.20 (Nov. 1999). Publisher: American Physical Society, pp. 14422–14428.

[35] Chihaya Adachi et al. "High-efficiency organic electrophosphorescent devices with tris(2-phenylpyridine)iridium doped into electron-transporting materials". In: *Applied Physics Letters* 77.6 (Aug. 2000). Publisher: American Institute of Physics, pp. 904–906.

[36] Chang-Lyoul Lee, Kyung Bok Lee, and Jang-Joo Kim. "Polymer phosphorescent light-emitting devices doped with tris(2-phenylpyridine) iridium as a triplet emitter". In: *Applied Physics Letters* 77.15 (Oct. 2000), pp. 2280–2282.

[37] Sergey Lamansky et al. "Highly Phosphorescent Bis-Cyclometalated Iridium Complexes: Synthesis, Photophysical Characterization, and Use in Organic Light Emitting Diodes". In: *Journal of the American Chemical Society* 123.18 (May 2001). Publisher: American Chemical Society, pp. 4304–4312.

[38] Caroline Murawski, Karl Leo, and Malte C. Gather. "Efficiency Roll-Off in Organic Light-Emitting Diodes". en. In: *Advanced Materials* 25.47 (2013). _eprint: https://onlinelibrary.wiley.com/doi/pdf/10.1002/adma.2013016 pp. 6801–6827.

[39] S. P. McGlynn and etc. *Molecular Spectroscopy of the Triplet State*. Englisch. Prentice Hall, 1969.

[40] Nicholas J. Turro and Juan C. Scaiano. *Principles of Molecular Photochemistry: An Introduction*. Englisch. 2009th ed. Sausalito, Calif: University Science Books, Jan. 2009.

[41] Andreas F. Rausch, Herbert H. H. Homeier, and Hartmut Yersin. "Organometallic Pt(II) and Ir(III) Triplet Emitters for OLED Applications and the Role of Spin–Orbit Coupling: A Study Based on High-Resolution Optical Spectroscopy". en. In: *Photophysics of Organometallics*. Ed. by Alistair J. Lees. Berlin, Heidelberg: Springer, 2010, pp. 193–235.

[42] Yi-Zhong Shi et al. "Recent progress in thermally activated delayed fluorescence emitters for nondoped organic light-emitting diodes". en. In: *Chemical Science* 13.13 (Mar. 2022). Publisher: The Royal Society of Chemistry, pp. 3625–3651.

[43] Hiroki Uoyama et al. "Highly efficient organic light-emitting diodes from delayed fluorescence". en. In: *Nature* 492.7428 (Dec. 2012). Publisher: Nature Publishing Group, pp. 234–238.

[44] Sebastian Reineke et al. "White organic light-emitting diodes: Status and perspective". In: *Reviews of Modern Physics* 85.3 (July 2013). Publisher: American Physical Society, pp. 1245–1293.

[45] Norbert Koch et al. "Optimized Hole Injection with Strong Electron Acceptors at Organic-Metal Interfaces". In: *Physical Review Letters* 95.23 (Nov. 2005). Publisher: American Physical Society, p. 237601.

[46] Tsubasa Sasaki et al. "Unravelling the electron injection/transport mechanism in organic light-emitting diodes". en. In: *Nature Communications* 12.1 (May 2021). Publisher: Nature Publishing Group, p. 2706.

[47] M. A. Baldo, C. Adachi, and S. R. Forrest. "Transient analysis of organic electrophosphorescence. II. Transient analysis of triplet-triplet annihilation". In: *Physical Review B* 62.16 (Oct. 2000). Publisher: American Physical Society, pp. 10967–10977.

[48] Lorenz von Reventlow. "Exzitonen-Dynamik in flüssigprozessierten organischen Leuchtdioden". ger. PhD thesis. Karlsruhe, 2021.

[49] B. J. Chen et al. "Electron drift mobility and electroluminescent efficiency of tris(8-hydroxyquinolinolato) aluminum". In: *Applied Physics Letters* 75.25 (Dec. 1999), pp. 4010–4012.

[50] Toshinori Matsushima et al. "Optical, morphological, structural, electrical, molecular orientation, and electroluminescence characteristics of organic semiconductor films prepared at various deposition rates". In: *Thin Solid Films* 520.6 (Jan. 2012), pp. 2283–2288.

[51] M. Mesta et al. "Kinetic Monte Carlo modeling of the efficiency roll-off in a multilayer white organic light-emitting device". In: *Applied Physics Letters* 108.13 (Mar. 2016), p. 133301.

[52] Sebastian Reineke, Karsten Walzer, and Karl Leo. "Triplet-exciton quenching in organic phosphorescent light-emitting diodes with Ir-based emitters". In: *Physical Review B* 75.12 (Mar. 2007). Publisher: American Physical Society, p. 125328.

[53] Nicholas J. Turro, V. Ramamurthy, and J. C. Scaiano. *Modern molecular photochemistry of organic molecules*. eng. OCLC: 396185412. Sausalito, Calif.: University Science Books, 2010.

[54] Franz Symalla et al. "Multiscale Simulation of Photoluminescence Quenching in Phosphorescent OLED Materials". In: *Advanced Theory and Simulations* 3.4 (2020). Number: 4, p. 1900222.

[55] Qi Wang, Bin Sun, and Hany Aziz. “Exciton–Polaron-Induced Aggregation of Wide-Bandgap Materials and its Implication on the Electroluminescence Stability of Phosphorescent Organic Light-Emitting Devices”. en. In: *Advanced Functional Materials* 24.20 (2014). _eprint: https://onlinelibrary.wiley.com/doi/pdf/10.1002/adfm.201303840, pp. 2975–2985.

[56] H. van Eersel et al. “Effect of Förster-mediated triplet-polaron quenching and triplet-triplet annihilation on the efficiency roll-off of organic light-emitting diodes”. In: *Journal of Applied Physics* 119.16 (Apr. 2016), p. 163102.

[57] Reinder Coehoorn et al. “Kinetic Monte Carlo Study of the Sensitivity of OLED Efficiency and Lifetime to Materials Parameters”. en. In: *Advanced Functional Materials* 25.13 (Apr. 2015). Publisher: John Wiley & Sons, Ltd, pp. 2024–2037.

[58] Jaesang Lee et al. “Hot excited state management for long-lived blue phosphorescent organic light-emitting diodes”. en. In: *Nature Communications* 8.1 (May 2017). Publisher: Nature Publishing Group, p. 15566.

[59] Susanna Schmidbauer, Andreas Hohenleutner, and Burkhard König. “Chemical Degradation in Organic Light-Emitting Devices: Mechanisms and Implications for the Design of New Materials”. en. In: *Advanced Materials* 25.15 (2013). _eprint: https://onlinelibrary.wiley.com/doi/pdf/10.1002/adma.201205022, pp. 2114–2129.

[60] M. A. Baldo, R. J. Holmes, and S. R. Forrest. “Prospects for electrically pumped organic lasers”. In: *Physical Review B* 66.3 (July 2002). Publisher: American Physical Society, p. 035321.

[61] S. D. Babenko et al. “Annihilation of singlet excited states in anthracene solutions”. In: *Chemical Physics Letters* 8.6 (Mar. 1971), pp. 598–600.

[62] Yifan Zhang et al. “Singlet–triplet quenching in high intensity fluorescent organic light emitting diodes”. In: *Chemical Physics Letters* 495.4 (Aug. 2010), pp. 161–165.

[63] Christian Gärtner et al. “The influence of annihilation processes on the threshold current density of organic laser diodes”. In: *Journal of Applied Physics* 101.2 (Jan. 2007), p. 023107.

[64] D. Kasemann et al. “Organic light-emitting diodes under high currents explored by transient electroluminescence on the nanosecond scale”. In: *Physical Review B* 84.11 (Sept. 2011). Publisher: American Physical Society, p. 115208.

[65] H. van Eersel et al. “Monte Carlo study of efficiency roll-off of phosphorescent organic light-emitting diodes: Evidence for dominant role of triplet-polaron quenching”. In: *Applied Physics Letters* 105.14 (Oct. 2014), p. 143303.

[66] M. Born and R. Oppenheimer. “Zur Quantentheorie der Molekeln”. en. In: *Annalen der Physik* 389.20 (1927), pp. 457–484.

[67] C. David Sherrill and Henry F. Schaefer. “The Configuration Interaction Method: Advances in Highly Correlated Approaches”. In: *Advances in Quantum Chemistry*. Ed. by Per-Olov Löwdin et al. Vol. 34. Academic Press, Jan. 1999, pp. 143–269.

[68] Rodney J. Bartlett and Monika Musiał. “Coupled-cluster theory in quantum chemistry”. In: *Reviews of Modern Physics* 79.1 (Feb. 2007). Publisher: American Physical Society, pp. 291–352.

[69] P. Hohenberg and W. Kohn. “Inhomogeneous Electron Gas”. en. In: *Physical Review* 136.3B (Nov. 1964), B864–B871.

[70] Christoph R. Jacob and Markus Reiher. “Spin in density-functional theory”. en. In: *International Journal of Quantum Chemistry* 112.23 (2012). _eprint: https://onlinelibrary.wiley.com/doi/pdf/10.1002/qua.24309, pp. 3661–3684.

[71] W. Kohn and L. J. Sham. “Self-Consistent Equations Including Exchange and Correlation Effects”. In: *Physical Review* 140.4A (Nov. 1965). Publisher: American Physical Society, A1133–A1138.

[72] Kieron Burke. “Perspective on density functional theory”. In: *The Journal of Chemical Physics* 136.15 (Apr. 2012), p. 150901.

[73] Axel D. Becke. “Density-functional thermochemistry. I. The effect of the exchange-only gradient correction”. In: *The Journal of Chemical Physics* 96.3 (Feb. 1992), pp. 2155–2160.

[74] Frank Jensen. *Introduction to computational chemistry*. en. 2nd ed. OCLC: ocm70707839. Chichester, England ; Hoboken, NJ: John Wiley & Sons, 2007.

[75] Pekka Koskinen and Ville Mäkinen. “Density-functional tight-binding for beginners”. en. In: *Computational Materials Science* 47.1 (Nov. 2009), pp. 237–253.

[76] Yang Yang et al. “Description of Phosphate Hydrolysis Reactions with the Self-Consistent-Charge Density-Functional-Tight-Binding (SCC-DFTB) Theory. 1. Parameterization”. In: *Journal of Chemical Theory and Computation* 4.12 (Dec. 2008). Publisher: American Chemical Society, pp. 2067–2084.

[77] M. Elstner et al. “Self-consistent-charge density-functional tight-binding method for simulations of complex materials properties”. In: *Physical Review B* 58.11 (Sept. 1998). Publisher: American Physical Society, pp. 7260–7268.

[78] M. Elstner et al. “A Self-Consistent Charge Density-Functional Based Tight-Binding Scheme for Large Biomolecules”. en. In: *physica status solidi (b)* 217.1 (2000). _eprint: https://onlinelibrary.wiley.com/doi/pdf/10.1002/%28SICI%291521-3951%28200001%29217%3A1%3C357%3A%3AAID-PSSB357%3E3.0.CO%3B2-J, pp. 357–376.

[79] Harald Oberhofer and Jochen Blumberger. “Revisiting electronic couplings and incoherent hopping models for electron transport in crystalline C60 at ambient temperatures”. en. In: *Physical Chemistry Chemical Physics* 14.40 (Sept. 2012). Publisher: The Royal Society of Chemistry, pp. 13846–13852.

[80] Per-Olov Löwdin. “On the Non-Orthogonality Problem Connected with the Use of Atomic Wave Functions in the Theory of Molecules and Crystals”. In: *The Journal of Chemical Physics* 18.3 (Mar. 1950), pp. 365–375.

[81] Adam Kubas et al. “Electronic couplings for molecular charge transfer: Benchmarking CDFT, FODFT, and FODFTB against high-level ab initio calculations”. In: *The Journal of Chemical Physics* 140.10 (Mar. 2014), p. 104105.

[82] Adam Kubas et al. “Electronic couplings for molecular charge transfer: benchmarking CDFT, FODFT and FODFTB against high-level ab initio calculations. II”. In: *Physical Chemistry Chemical Physics* 17.22 (May 2015). Number: 22, pp. 14342–14354.

[83] Orestis George Ziogos et al. “HAB79: A new molecular dataset for benchmarking DFT and DFTB electronic couplings against high-level ab initio calculations”. In: *The Journal of Chemical Physics* 155.23 (Dec. 2021). Number: 23, p. 234115.

[84] Harald Oberhofer, Karsten Reuter, and Jochen Blumberger. “Charge Transport in Molecular Materials: An Assessment of Computational Methods”. In: *Chemical Reviews* 117.15 (Aug. 2017). Number: 15, pp. 10319–10357.

[85] Walter Kob and Hans C. Andersen. “Testing mode-coupling theory for a supercooled binary Lennard-Jones mixture I: The van Hove correlation function”. In: *Physical Review E* 51.5 (May 1995). Publisher: American Physical Society, pp. 4626–4641.

[86] Srikanth Sastry, Pablo G. Debenedetti, and Frank H. Stillinger. “Signatures of distinct dynamical regimes in the energy landscape of a glass-forming liquid”. en. In: *Nature* 393.6685 (June 1998). Publisher: Nature Publishing Group, pp. 554–557.

[87] Alexander Lukyanov, Christian Lennartz, and Denis Andrienko. “Amorphous films of tris(8-hydroxyquinolinato)aluminium: Force-field, morphology, and charge transport”. en. In: *physica status solidi (a)* 206.12 (2009). _eprint: https://onlinelibrary.wiley.com/doi/pdf/10.1002/pssa.200925276, pp. 2737–2742.

[88] Falk May et al. “Can Lattice Models Predict the Density of States of Amorphous Organic Semiconductors?” In: *Physical Review Letters* 109.13 (Sept. 2012). Publisher: American Physical Society, p. 136401.

[89] J. J. Kwiatkowski et al. “Simulating charge transport in tris(8-hydroxyquinoline) aluminium (Alq3)”. en. In: *Physical Chemistry Chemical Physics* 10.14 (Mar. 2008). Publisher: The Royal Society of Chemistry, pp. 1852–1858.

[90] Junmei Wang et al. “Development and testing of a general amber force field”. en. In: *Journal of Computational Chemistry* 25.9 (2004). _eprint: https://onlinelibrary.wiley.com/doi/pdf/10.1002/jcc.20035, pp. 1157–1174.

[91] Junmei Wang et al. “Automatic atom type and bond type perception in molecular mechanical calculations”. In: *Journal of Molecular Graphics and Modelling* 25.2 (Oct. 2006), pp. 247–260.

[92] Nicholas Metropolis et al. “Equation of State Calculations by Fast Computing Machines”. In: *The Journal of Chemical Physics* 21.6 (June 1953), pp. 1087–1092.

[93] S. Kirkpatrick, C. D. Gelatt, and M. P. Vecchi. “Optimization by Simulated Annealing”. In: *Science* 220.4598 (May 1983). Publisher: American Association for the Advancement of Science, pp. 671–680.

[94] Jack Wildman et al. “General Force-Field Parametrization Scheme for Molecular Dynamics Simulations of Conjugated Materials in Solution”. In: *Journal of Chemical Theory and Computation* 12.8 (Aug. 2016). Publisher: American Chemical Society, pp. 3813–3824.

[95] Loup Verlet. “Computer ”Experiments” on Classical Fluids. I. Thermodynamical Properties of Lennard-Jones Molecules”. In: *Physical Review* 159.1 (July 1967). Publisher: American Physical Society, pp. 98–103.

[96] H. J. C. Berendsen, D. van der Spoel, and R. van Drunen. “GROMACS: A message-passing parallel molecular dynamics implementation”. In: *Computer Physics Communications* 91.1 (Sept. 1995). Number: 1, pp. 43–56.

[97] Tetsuya Morishita. “Fluctuation formulas in molecular-dynamics simulations with the weak coupling heat bath”. In: *The Journal of Chemical Physics* 113.8 (Aug. 2000), pp. 2976–2982.

[98] Chuan Liu et al. “A unified understanding of charge transport in organic semiconductors: the importance of attenuated delocalization for the carriers”. en. In: *Materials Horizons* 4.4 (July 2017). Publisher: The Royal Society of Chemistry, pp. 608–618.

[99] Artem Fediai et al. “Disorder-driven doping activation in organic semiconductors”. en. In: *Physical Chemistry Chemical Physics* 22.18 (May 2020). Publisher: The Royal Society of Chemistry, pp. 10256–10264.

[100] A. Sommerfeld and H. Bethe. “Elektronentheorie der Metalle”. de. In: *Aufbau Der Zusammenhängenden Materie*. Ed. by A. Smekal. Berlin, Heidelberg: Springer, 1933, pp. 333–622.

[101] Rocco P. Fornari and Alessandro Troisi. “Theory of charge hopping along a disordered polymer chain”. en. In: *Physical Chemistry Chemical Physics* 16.21 (May 2014). Publisher: The Royal Society of Chemistry, pp. 9997–10007.

[102] J. Klafter. “Hopping Transport in Disordered Systems”. en. In: *Organic Molecular Aggregates*. Ed. by Peter Reineker, Hermann Haken, and Hans Christoph Wolf. Berlin, Heidelberg: Springer, 1983, pp. 169–183.

[103] R. A. Marcus. “On the Theory of Oxidation-Reduction Reactions Involving Electron Transfer. I”. en. In: *The Journal of Chemical Physics* 24.5 (May 1956). Number: 5, pp. 966–978.

[104] Karin Zojer. “Simulation of Charge Carriers in Organic Electronic Devices: Methods with their Fundamentals and Applications”. In: *Advanced Optical Materials* 9.14 (2021). Number: 14, p. 2100219.

[105] Stephen F. Nelsen, Silas C. Blackstock, and Yaesil Kim. “Estimation of inner shell Marcus terms for amino nitrogen compounds by molecular orbital calculations”. In: *Journal of the American Chemical Society* 109.3 (Feb. 1987). Number: 3, pp. 677–682.

[106] Omar López-Estrada et al. "Reassessment of the Four-Point Approach to the Electron-Transfer Marcus–Hush Theory". In: *ACS Omega* 3.2 (Feb. 2018). Publisher: American Chemical Society, pp. 2130–2140.

[107] Damodar M. Pai. "Transient Photoconductivity in Poly(N-vinylcarbazole)". In: *The Journal of Chemical Physics* 52.5 (Mar. 1970), pp. 2285–2291.

[108] Gianluca Tirimbò and Björn Baumeier. "Ab initio modeling of excitons: from perfect crystals to biomaterials". EN. In: *Advances in Physics: X* (Jan. 2021). Publisher: Taylor & Francis.

[109] J. D. Wright. *Molecular Crystals*. en. Google-Books-ID: 7sroAgMASIEC. Cambridge University Press, 1995.

[110] D. L. Dexter. "A Theory of Sensitized Luminescence in Solids". In: *The Journal of Chemical Physics* 21.5 (May 1953), pp. 836–850.

[111] Th. Förster. "Zwischenmolekulare Energiewanderung und Fluoreszenz". de. In: *Annalen der Physik* 437.1-2 (1948). _eprint: https://onlinelibrary.wiley.com/doi/pdf/10.1002/andp.19484370105, pp. 55–75.

[112] Vera Stehr et al. "Singlet Exciton Diffusion in Organic Crystals Based on Marcus Transfer Rates". In: *Journal of Chemical Theory and Computation* 10.3 (Mar. 2014). Number: 3 Publisher: American Chemical Society, pp. 1242–1255.

[113] Stefan K. Possanner et al. "Threshold Voltage Shifts in Organic Thin-Film Transistors Due to Self-Assembled Monolayers at the Dielectric Surface". en. In: *Advanced Functional Materials* 19.6 (2009). _eprint: https://onlinelibrary.wiley.com/doi/pdf/10.1002/adfm.200801466, pp. 958–967.

[114] Fabrizio Torricelli et al. "Ultra-high gain diffusion-driven organic transistor". en. In: *Nature Communications* 7.1 (Feb. 2016). Publisher: Nature Publishing Group, p. 10550.

[115] Christopher M. Snowden. *Introduction to Semiconductor Device Modelling*. en. Google-Books-ID: dmFd9ExMaVgC. World Scientific, 1998.

[116] M. Gruber et al. "Impact of energy alignment and morphology on the efficiency in inorganic–organic hybrid solar cells". In: *Organic Electronics* 11.12 (Dec. 2010), pp. 1999–2011.

[117] Weifeng Zhou, Christoph Zimmermann, and Christoph Jungemann. "Master equation study of excitonic processes limiting the luminous efficacy in phosphorescent organic light-emitting diodes". In: *Journal of Applied Physics* 125.16 (Apr. 2019), p. 165501.

[118] H. Houili et al. "Investigation of the charge transport through disordered organic molecular heterojunctions". In: *Journal of Applied Physics* 100.3 (Aug. 2006), p. 033702.

[119] Mosè Casalegno, Guido Raos, and Riccardo Po. "Methodological assessment of kinetic Monte Carlo simulations of organic photovoltaic devices: The treatment of electrostatic interactions". en. In: *The Journal of Chemical Physics* 132.9 (Mar. 2010), p. 094705.

[120] Franz Symalla. "Modellierung von Ladungs- und Exzitondynamik in amorphen organischen Halbleitern = Modeling of charge and exciton dynamics in amorphous organic semiconductors". PhD Thesis. Karlsruher Institut für Technologie (KIT), 2018.

[121] Ali Deniz Özdemir et al. "Dynamic Effects on Hole Transport in Amorphous Organic Semiconductors: a Combined QM/MM and kMC Study". In: *Journal of Chemical Theory and Computation* 19.13 (July 2023). Publisher: American Chemical Society, pp. 3849–3860.

[122] Alexander Heck et al. "Multi-Scale Approach to Non-Adiabatic Charge Transport in High-Mobility Organic Semiconductors". In: *Journal of Chemical Theory and Computation* 11.11 (Nov. 2015). Number: 11, pp. 5068–5082.

[123] Pascal Friederich et al. "Molecular Origin of the Charge Carrier Mobility in Small Molecule Organic Semiconductors". In: *Advanced Functional Materials* 26.31 (2016). Number: 31, pp. 5757–5763.

[124] Franz Symalla et al. "Charge Transport by Superexchange in Molecular Host-Guest Systems". In: *Physical Review Letters* 117.27 (Dec. 2016). Number: 27, p. 276803.

[125] Simon Kaiser et al. "De Novo Calculation of the Charge Carrier Mobility in Amorphous Small Molecule Organic Semiconductors". English. In: *Frontiers in Chemistry* 9 (Dec. 2021). Publisher: Frontiers.

[126] Simon Kaiser et al. "De Novo Simulation of Charge Transport through Organic Single-Carrier Devices". In: *Journal of Chemical Theory and Computation* 17.10 (Oct. 2021). Publisher: American Chemical Society, pp. 6416–6422.

[127] Naga Rajesh Tummala et al. "Static and Dynamic Energetic Disorders in the C60, PC61BM, C70, and PC71BM Fullerenes". In: *The Journal of Physical Chemistry Letters* 6.18 (Sept. 2015). Number: 18, pp. 3657–3662.

[128] Giacomo Londi et al. "Fate of Low-Lying Charge-Transfer Excited States in a Donor:Acceptor Blend with a Large Energy Offset". In: *The Journal of Physical Chemistry Letters* 11.23 (Dec. 2020). Number: 23, pp. 10219–10226.

[129] Gabriele D'Avino et al. "Electrostatic phenomena in organic semiconductors: fundamentals and implications for photovoltaics". In: *Journal of Physics: Condensed Matter* 28.43 (Nov. 2016). Number: 43, p. 433002.

[130] Alessandro Troisi, David L. Cheung, and Denis Andrienko. "Charge Transport in Semiconductors with Multiscale Conformational Dynamics". In: *Physical Review Letters* 102.11 (Mar. 2009). Number: 11, p. 116602.

[131] Geoffrey R. Hutchison, Mark A. Ratner, and Tobin J. Marks. "Hopping Transport in Conductive Heterocyclic Oligomers: Reorganization Energies and Substituent Effects". In: *Journal of the American Chemical Society* 127.7 (Feb. 2005). Number: 7, pp. 2339–2350.

[132] Thorsten Vehoff et al. “Charge Transport in Organic Crystals: Role of Disorder and Topological Connectivity”. In: *Journal of the American Chemical Society* 132.33 (Aug. 2010). Number: 33, pp. 11702–11708.

[133] James Kirkpatrick et al. “Columnar mesophases of hexabenzocoronene derivatives. II. Charge carrier mobility”. In: *The Journal of Chemical Physics* 129.9 (Sept. 2008). Number: 9, p. 094506.

[134] Patrick Reiser et al. “Analyzing Dynamical Disorder for Charge Transport in Organic Semiconductors via Machine Learning”. In: *Journal of Chemical Theory and Computation* 17.6 (June 2021). Number: 6, pp. 3750–3759.

[135] G. Aydin and I. Yavuz. “Intrinsic Static/Dynamic Energetic Disorders of Amorphous Organic Semiconductors: Microscopic Simulations and Device Study”. In: *The Journal of Physical Chemistry C* 125.12 (Apr. 2021). Number: 12, pp. 6862–6869.

[136] David N. Beratan et al. “Charge Transfer in Dynamical Biosystems, or The Treachery of (Static) Images”. In: *Accounts of Chemical Research* 48.2 (Feb. 2015). Number: 2, pp. 474–481.

[137] Spiros S. Skourtis, David H. Waldeck, and David N. Beratan. “Fluctuations in Biological and Bioinspired Electron-Transfer Reactions”. In: *Annual Review of Physical Chemistry* 61.1 (Mar. 2010). Number: 1, pp. 461–485.

[138] David N. Beratan and J. J. Hopfield. “Failure of the Born-Oppenheimer and Franck-Condon approximations for long distance electron transfer rate calculations”. In: *Journal of Chemical Physics* 81 (Dec. 1984), pp. 5753–5759.

[139] Spiros S. Skourtis et al. “Protein dynamics and electron transfer: electronic decoherence and non-Condon effects”. eng. In: *Proceedings of the National Academy of Sciences of the United States of America* 102.10 (Mar. 2005). Number: 10, pp. 3552–3557.

[140] Sai Manoj Gali et al. “Energetic fluctuations in amorphous semiconducting polymers: Impact on charge-carrier mobility”. In: *The Journal of Chemical Physics* 147.13 (Oct. 2017). Number: 13, p. 134904.

[141] D. Porezag et al. “Construction of tight-binding-like potentials on the basis of density-functional theory: Application to carbon”. In: *Physical Review B* 51.19 (May 1995). Number: 19, pp. 12947–12957.

[142] G. Seifert, D. Porezag, and Th. Frauenheim. “Calculations of molecules, clusters, and solids with a simplified LCAO-DFT-LDA scheme”. In: *International Journal of Quantum Chemistry* 58.2 (1996). Number: 2, pp. 185–192.

[143] Alexander Heck, Julian J. Kranz, and Marcus Elstner. “Simulation of Temperature-Dependent Charge Transport in Organic Semiconductors with Various Degrees of Disorder”. In: *Journal of Chemical Theory and Computation* 12.7 (July 2016). Number: 7, pp. 3087–3096.

[144] A. Massé, R. Coehoorn, and P. A. Bobbert. “Universal Size-Dependent Conductance Fluctuations in Disordered Organic Semiconductors”. In: *Physical Review Letters* 113.11 (Sept. 2014). Number: 11, p. 116604.

[145] Björn Baumeier et al. “Stochastic modeling of molecular charge transport networks”. In: *Physical Review B* 86.18 (Nov. 2012). Number: 18, p. 184202.

[146] Franz Symalla et al. “43-3: Ab-initio Simulation of Doped Injection Layers.” en. In: *SID Symposium Digest of Technical Papers* 51.1 (Aug. 2020), pp. 630–633.

[147] Mark James Abraham et al. “GROMACS: High performance molecular simulations through multi-level parallelism from laptops to supercomputers”. In: *SoftwareX* 1-2 (Sept. 2015), pp. 19–25.

[148] U. Chandra Singh and Peter A. Kollman. “An approach to computing electrostatic charges for molecules”. en. In: *Journal of Computational Chemistry* 5.2 (1984). _eprint: https://onlinelibrary.wiley.com/doi/pdf/10.1002/jcc.540050204, pp. 129–145.

[149] Brent H. Besler, Kenneth M. Merz Jr., and Peter A. Kollman. “Atomic charges derived from semiempirical methods”. In: *Journal of Computational Chemistry* 11.4 (1990). Number: 4, pp. 431–439.

[150] G. A. Petersson et al. “A complete basis set model chemistry. I. The total energies of closed-shell atoms and hydrides of the first-row elements”. In: *The Journal of Chemical Physics* 89.4 (Aug. 1988). Number: 4, pp. 2193–2218.

[151] G. A. Petersson and Mohammad A. Al-Laham. “A complete basis set model chemistry. II. Open-shell systems and the total energies of the first-row atoms”. In: *The Journal of Chemical Physics* 94.9 (May 1991). Number: 9, pp. 6081–6090.

[152] Pascal Friederich et al. “Ab Initio Treatment of Disorder Effects in Amorphous Organic Materials: Toward Parameter Free Materials Simulation”. In: *Journal of Chemical Theory and Computation* 10.9 (Sept. 2014). Number: 9 Publisher: American Chemical Society, pp. 3720–3725.

[153] Anirban Mondal et al. “Molecular library of OLED host materials—Evaluating the multiscale simulation workflow”. In: *Chemical Physics Reviews* 2.3 (Sept. 2021). Number: 3, p. 031304.

[154] Andrea Massé et al. “Ab initio charge-carrier mobility model for amorphous molecular semiconductors”. In: *Physical Review B* 93.19 (May 2016). Number: 19, p. 195209.

[155] Govind S. Mudholkar and Alan D. Hutson. “The epsilon–skew–normal distribution for analyzing near-normal data”. In: *Journal of Statistical Planning and Inference* 83.2 (Feb. 2000). Number: 2, pp. 291–309.

[156] Arnaud Delarue and Dominique Jeulin. “MULTI-SCALE SIMULATION OF SPHERICAL AGGREGATES”. en. In: *Image Analysis and Stereology* 20.3 (2001). Number: 3, pp. 181–186.

[157] M. Bouhassoune et al. “Carrier-density and field-dependent charge-carrier mobility in organic semiconductors with correlated Gaussian disorder”. In: *Organic Electronics* 10.3 (May 2009). Number: 3, pp. 437–445.

[158] Hidenobu Matsushima et al. “Organic electrophosphorescent devices with mixed hole transport material as emission layer”. In: *Current Applied Physics* 5.4 (May 2005). Number: 4, pp. 305–308.

[159] Seunguk Noh et al. “Carrier conduction mechanism for phosphorescent material doped organic semiconductor”. In: *Journal of Applied Physics* 105.3 (Feb. 2009). Number: 3, p. 033709.

[160] Dal Ho Huh et al. “High hole mobility hole transport material for organic light-emitting devices”. In: *Synthetic Metals* 180 (Sept. 2013), pp. 79–84.

[161] Kenji Okumoto et al. “Amorphous molecular materials: charge transport in the glassy state of N,N′-di(biphenylyl)-N,N′-diphenyl-[1,1′-biphenyl]-4,4′-diamines”. en. In: *Synthetic Metals* 111-112 (June 2000), pp. 473–476.

[162] J. O. Oelerich et al. “Field dependence of hopping mobility: Lattice models against spatial disorder”. In: *Physical Review B* 96.19 (Nov. 2017). Number: 19, p. 195208.

[163] Ali Deniz Özdemir et al. “In silico studies of OLED device architectures regarding their efficiency”. In: *Frontiers in Physics* 11 (2023).

[164] Ali Deniz Özdemir et al. “Systematic kMC Study of Doped Hole Injection Layers in Organic Electronics”. In: *Frontiers in Chemistry* 9 (2022).

[165] Leanne Paterson, Falk May, and Denis Andrienko. “Computer aided design of stable and efficient OLEDs”. In: *Journal of Applied Physics* 128.16 (Oct. 2020), p. 160901.

[166] Sebastian Wehrmeister et al. “Combined Electrical and Optical Analysis of the Efficiency Roll-Off in Phosphorescent Organic Light-Emitting Diodes”. In: *Physical Review Applied* 3.2 (Feb. 2015). Number: 2, p. 024008.

[167] Sebastian Engmann et al. “Higher order effects in organic LEDs with sub-bandgap turn-on”. In: *Nature Communications* 10.1 (Jan. 2019). Number: 1, p. 227.

[168] Vadim I. Adamovich et al. “New charge-carrier blocking materials for high efficiency OLEDs”. In: *Organic Electronics*. High Efficiency Light Emitters 4.2 (Sept. 2003). Number: 2, pp. 77–87.

[169] Murat Mesta et al. “Molecular-scale simulation of electroluminescence in a multilayer white organic light-emitting diode”. In: *Nature Materials* 12.7 (July 2013). Number: 7, pp. 652–658.

[170] Allen Miller and Elihu Abrahams. “Impurity Conduction at Low Concentrations”. en. In: *Physical Review* 120.3 (Nov. 1960). Number: 3, pp. 745–755.

[171] Robin G. E. Kimber et al. “Mesoscopic kinetic Monte Carlo modeling of organic photovoltaic device characteristics”. In: *Physical Review B* 86.23 (Dec. 2012). Number: 23 Publisher: American Physical Society, p. 235206.

[172] P. P. Ewald. “Die Berechnung optischer und elektrostatischer Gitterpotentiale”. In: *Annalen der Physik* 369.3 (1921). Number: 3, pp. 253–287.

[173] Anna Köhler and Heinz Bässler. “What controls triplet exciton transfer in organic semiconductors?” In: *Journal of Materials Chemistry* 21.12 (2011). Number: 12, pp. 4003–4011.

[174] Shu-Wen Zheng et al. “Dexter-Type Exciton Transfer in van der Waals Heterostructures”. In: *Advanced Functional Materials* 32.26 (2022). Number: 26, p. 2201123.

[175] Tobias Brixner et al. “Exciton Transport in Molecular Aggregates – From Natural Antennas to Synthetic Chromophore Systems”. In: *Advanced Energy Materials* 7.16 (2017). Number: 16, p. 1700236.

[176] Qingyun Wan et al. “Efficient Long-Range Triplet Exciton Transport by Metal–Metal Interaction at Room Temperature”. In: *Angewandte Chemie International Edition* 61.10 (2022). Number: 10, e202114323.

[177] Denis Y. Kondakov. “Triplet–triplet annihilation in highly efficient fluorescent organic light-emitting diodes: current state and future outlook”. In: *Philosophical Transactions of the Royal Society A: Mathematical, Physical and Engineering Sciences* 373.2044 (June 2015). Number: 2044, p. 20140321.

[178] Shubham Negi, Poornima Mittal, and Brijesh Kumar. “Impact of different layers on performance of OLED”. In: *Microsystem Technologies* 24.12 (Dec. 2018). Number: 12, pp. 4981–4989.

[179] Sebastian Reineke and Marc A. Baldo. “Recent progress in the understanding of exciton dynamics within phosphorescent OLEDs”. In: *physica status solidi (a)* 209.12 (2012). Number: 12, pp. 2341–2353.

[180] Stefan Höfle et al. “Influence of the Emission Layer Thickness on the Optoelectronic Properties of Solution Processed Organic Light-Emitting Diodes”. In: *ACS Photonics* 1.10 (Oct. 2014). Number: 10, pp. 968–973.

[181] John S. Bangsund, Kyle W. Hershey, and Russell J. Holmes. “Isolating Degradation Mechanisms in Mixed Emissive Layer Organic Light-Emitting Devices”. In: *ACS Applied Materials & Interfaces* 10.6 (Feb. 2018). Number: 6 Publisher: American Chemical Society, pp. 5693–5699.

[182] Boris Minaev, Gleb Baryshnikov, and Hans Agren. “Principles of phosphorescent organic light emitting devices”. In: *Physical Chemistry Chemical Physics* 16.5 (Jan. 2014). Number: 5, pp. 1719–1758.

[183] Rico Meerheim et al. “Ultrastable and efficient red organic light emitting diodes with doped transport layers”. In: *Applied Physics Letters* 89.6 (Aug. 2006), p. 061111.

[184] Sebastian Reineke et al. “White organic light-emitting diodes with fluorescent tube efficiency”. en. In: *Nature* 459.7244 (May 2009). Publisher: Nature Publishing Group, pp. 234–238.

[185] Sebastian Scholz et al. “Degradation Mechanisms and Reactions in Organic Light-Emitting Devices”. In: *Chemical Reviews* 115.16 (Aug. 2015). Publisher: American Chemical Society, pp. 8449–8503.

[186] Hany Aziz and Zoran Popovic. “Degradation Phenomena in Small-Molecule Organic Light-Emitting Devices”. In: *Chemistry of Materials - CHEM MATER* 16 (July 2004).

[187] P. E. Burrows et al. “Reliability and degradation of organic light emitting devices”. In: *Applied Physics Letters* 65.23 (Dec. 1994), pp. 2922–2924.

[188] Youngkyoo Kim et al. “Accelerated pre-oxidation method for healing progressive electrical short in organic light-emitting devices”. In: *Applied Physics Letters* 82.14 (Apr. 2003), pp. 2200–2202.

[189] Yifan Zhang, Jaesang Lee, and Stephen R. Forrest. "Tenfold increase in the lifetime of blue phosphorescent organic light-emitting diodes". en. In: *Nature Communications* 5.1 (Sept. 2014). Publisher: Nature Publishing Group, p. 5008.

[190] N. C. Giebink et al. "Intrinsic luminance loss in phosphorescent small-molecule organic light emitting devices due to bimolecular annihilation reactions". In: *Journal of Applied Physics* 103.4 (Feb. 2008). Publisher: American Institute of Physics, p. 044509.

[191] N. C. Giebink et al. "Direct evidence for degradation of polaron excited states in organic light emitting diodes". In: *Journal of Applied Physics* 105.12 (June 2009), p. 124514.

[192] Yufei Shen and Noel C. Giebink. "Monte Carlo Simulations of Nanoscale Electrical Inhomogeneity in Organic Light-Emitting Diodes and Its Impact on Their Efficiency and Lifetime". In: *Physical Review Applied* 4.5 (Nov. 2015). Publisher: American Physical Society, p. 054017.

[193] Christoph Hauenstein et al. "Identification of OLED Degradation Scenarios by Kinetic Monte Carlo Simulations of Lifetime Experiments". In: *Frontiers in Chemistry* 9 (2022).

[194] Melanie H. Bowler et al. "Understanding the superior temperature stability of iridium light-emitting electrochemical cells". en. In: *Materials Horizons* 4.4 (July 2017). Publisher: The Royal Society of Chemistry, pp. 657–664.

[195] Franz Symalla et al. "43-3: Ab-initio Simulation of Doped Injection Layers." en. In: *SID Symposium Digest of Technical Papers* 51.1 (2020). _eprint: https://onlinelibrary.wiley.com/doi/pdf/10.1002/sdtp.13946, pp. 630–633.